ELECTROOPTIC STREAK CAMERA

John B. Shaw
B.A., Portland State University, 1970
M.S., Oregon Graduate Center, 1976

A dissertation submitted to the faculty
of the Oregon Graduate Center
in partial fulfillment of the
requirements for the degree
Doctor of Philosophy
in
Applied Physics & Electronic Science

July, 1980

The dissertation "Electrooptic Streak Camera" by John B. Shaw has been examined and approved by the following Examination Committee:

RICHARD A. ELLIOTT, Thesis Advisor
Associate Professor

J. FRED HOLMES
Professor

GAIL A. MASSEY
Professor

DOUGLAS F. BAROFSKY
Associate Professor

THOMAS K. PLANT
Assistant Professor
Oregon State University

DEDICATION

I dedicate this dissertation to my wife, without whose support and many sacrifices this would not have been undertaken or completed.

ACKNOWLEDGEMENTS

I would like to thank Dr. Richard Elliott for his unswerving patience and timely encouragements while guiding me in this work, and Dr. Gail Massey for many valuable discussions concerning some of the technical subtleties of this work.

TABLE OF CONTENTS

	Page
DEDICATION/ACKNOWLEDGEMENTS	iii
LIST OF TABLES	vi
LIST OF ILLUSTRATIONS	vii
ABSTRACT	ix

Chapter

1. INTRODUCTION 1
2. SIMPLE ELECTROOPTIC DEFLECTION TECHNIQUES 12
   - 2.1 Quadrupole Gradient Deflectors 13
   - 2.2 Prism Deflectors 17
   - 2.3 Traveling Lens Deflector 24
   - 2.4 Comparisons 28
3. DEFLECTION SYSTEMS WITHOUT TRANSIT TIME LIMITATIONS . . 34
   - 3.1 Multiple Prism System 35
   - 3.2 Lens systems--Geometric Considerations 42
   - 3.3 Multiple Lens System 48
   - 3.4 Single Lens 57
   - 3.5 Comparisons of the Multiple Unit Systems 59
   - 3.6 Voltage Pulse Generator Limitations 62
   - 3.7 Some Typical Designs 66
4. SUPPORTING SYSTEMS AND TEST APPARATUS 69
   - 4.1 Fast High Voltage Pulse Production 69
     - 4.1.1 Photoconducting Switches 70
     - 4.1.2 Photoconductivity in Silicon Junctions . . . 83
     - 4.1.3 Spark Gaps 83
     - 4.1.4 Pulse Forming Networks 87
   - 4.2 High Voltage Pulse Transmission and Coupling Techniques 91
     - 4.2.1 Transmission Lines 92
     - 4.2.2 Transitions 94

Page

4.3 Light Pulse Generation 98

4.3.1 The Oscillator, Amplifier, and Doubler . . . 99
4.3.2 Single Pulse Selection 101

5. DIAGNOSTICS 110

6. EXPERIMENTAL RESULTS 115

7. FUTURE WORK 126

APPENDIX

1. QUADRUPOLE GEOMETRY 128

2. NEGATIVE LENS DEFLECTOR 133

REFERENCES 139

BIOGRAPHICAL NOTE 145

LIST OF TABLES

Table Page

1. Simple Deflector Volume Comparisons 31

2. Ray Matrices 49

3. Practical Designs for Lithium Niobate Traveling Lens Deflector (λ = 1μm) 67

4. Oscillator and Mode Locking Configurations 100

LIST OF ILLUSTRATIONS

Figure Page

1. The second harmonic generation technique devised by Weber 3

2. A typical setup for Two Photon Fluorescence 4

3. A Kerr cell shutter 6

4. A photoelectron streak camera 8

5. The electrooptic streak camera 10

6. a) The basic quadrupole deflector arrangement. Hyperbolic electrodes induce a linear field gradient b) which may be used to deflect a light beam 14

7. The basic two-prism deflector 19

8. The traveling lens deflector 25

9. The multiple prism stripline deflector 35

10. The iterated traveling lens deflector 36

11. The two-prism deflector in a stripline configuration . . 38

12. Traveling lens geometric limitations 44

13a. An optically activated silicon switch 71

13b. Coordinate system for analyzing the light activated switch 71

14. Design chart for light activated silicon switches . . . 75

15. Silicon properties vs. temperature 77

16. Fermi level plot for the silicon sample indicating possible deep level traps at about .3 eV below the conduction band 78

17. Silicon switch electrode geometries and breakdown voltage waveforms 81

Figure		Page

18. Characteristics of mylar dielectric, stripline, spark gaps 85

19. Simple charged line pulse forming network 89

20. Coax to stripline couplings 95

21. Dual avalanche chain switchout electronics 104

22. Krytron switchout electronics 106

23. Operating characteristics of the single pulse selector 108

24. Test apparatus arrangement 111

25. Experimental arrangement for deflection experiments . . 116

26. Deflector--exploded view 118

27. Sample experimental results for first deflection experiment 119

28. The setup for the second deflection experiment 122

29. Sample experimental results for second deflection experiment 124

A1-1. The hyperbolic electrode structure of the quadrupole deflector is shown along with the coordinates of points referenced in the analysis 132

A2-1. Central ray deflection 135

A2-2. Positive and negative lens deflection characteristics 136

ABSTRACT

ELECTROOPTIC STREAK CAMERA

John B. Shaw, Ph.D.
Oregon Graduate Center, 1980

Supervising Professor: Richard A. Elliott

This dissertation presents the results of research directed towards the development of an electrooptic streak camera. A number of electrooptic techniques have been utilized to provide beam deflection, but, as shown here, they are all subject to limitations imposed by transit time of light through the device. These limitations may be overcome, however, by suitably combining a number of simple deflectors to form a strip transmission line which can provide a synchronous interaction between an electrical pulse and the optical pulse to be displayed. This new deflector is capable of excellent service in streak camera applications.

Unfortunately, the existence of a suitable deflection technique does not immediately guarantee the development of a practical electrooptic streak camera; major difficulties exist in the production of an acceptable voltage pulse generator. Photoconducting silicon switches offer a possible solution, but they have not yet attained the performance level necessary for this application as highlighted by the investigations carried out in this work. Laser triggered spark gaps are the best alternative, and utilizing one of these, the first demonstration of the new deflection technique has been accomplished.

Although the results have been less than dramatic, the best resolution time obtained being only 750 picoseconds, they show that it should be possible to construct an electrooptic streak camera providing better than 10 picosecond resolution in the near infrared.

CHAPTER 1

INTRODUCTION

Since the late 1960's, interest in picosecond phenomena has steadily increased, primarily in response to the development of techniques for producing and measuring picosecond optical pulses. It is now possible to make direct measurements, on a picosecond time scale, of phenomena such as intermolecular and intramolecular lifetimes.[1-3] Utilizing transform limited pulses,[4] phase dependent propagation phenomena such as coherent photon response[5] and self-induced transparency[6] may be studied. In the context of laser fusion research, picosecond pulse measurements provide diagnostic aids for laser development and pulse shaping systems. As new pulse sources and measurement techniques are developed, new avenues of research appear, and this field continues to grow.

A variety of techniques exist for the measurement of picosecond optical pulses, including a number based on linear or nonlinear optical interactions, and one, the photoelectron streak camera, based on the generation and subsequent deflection of an electron beam. Bradley and New[7] have written an excellent paper reviewing and comparing these various techniques. A short review is included here which illustrates the advantages and limitations of the various measurement techniques in current usage.

The first direct evidence of picosecond structure in laser pulses came from measurements based upon second harmonic generation (SHG).[8-12]

A typical setup as used by Weber[10, 12] is illustrated in Figure 1. The beam splitter routes part of the incoming beam to each polarizer where two beams of orthogonally polarized light are generated. After recombination, the two beams pass through the index matched Potassium Dihydrogen Phosphate (KDP) crystal to induce SHG of the second kind.[13] The detector receives the light that has passed through the second harmonic filter. SHG occurs only when the two recombined beams overlap in the KDP crystal. To obtain a pulse profile, measurements of the second harmonic power must be made with many pulses while systematically varying the overlap of the two pulses in the KDP. Since no SHG occurs when no overlap exists, the second harmonic background light is zero, this being the major advantage of this arrangement. Also, since the second harmonic is coherent light, it emerges from the KDP in a nearly parallel beam that is easy to collect efficiently. However, the high light intensities required and the many measurements necessary to obtain a profile are major disadvantages of this technique.

For single pulse events the two photon fluorescence (TPF) technique may be used. Referring to Figure 2, the incoming beam is split and subsequently recombined in a dye which fluoresces only from two-photon absorption of the incident light. A single pulse passing through the dye will generate some background fluorescence. Since the intensity of the fluorescence grows as the square of the intensity, a second pulse, of intensity equal to the first, will result in four

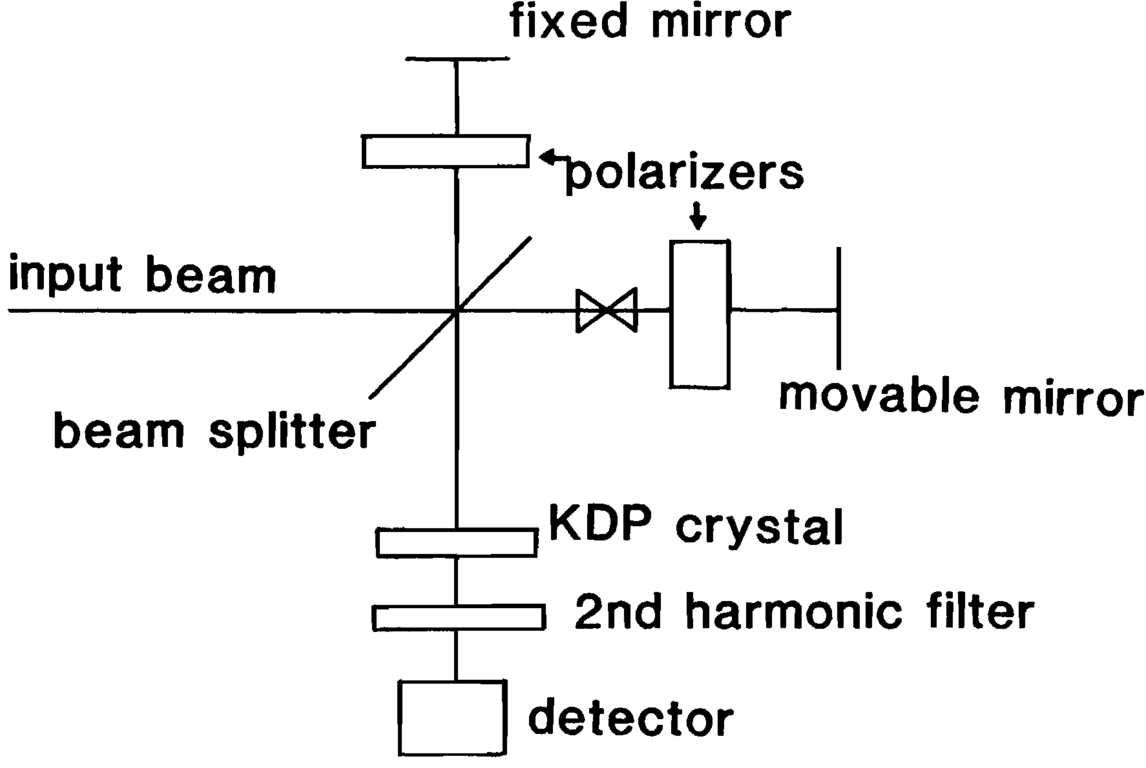

Figure 1. The second harmonic generation technique devised by Weber. The KDP produces SHG of the second kind from the two overlapping, orthogonally polarized beams provided from the input beam by the beam splitter and polarizers. Adjustment of the movable mirror allows pulsewidth determination.

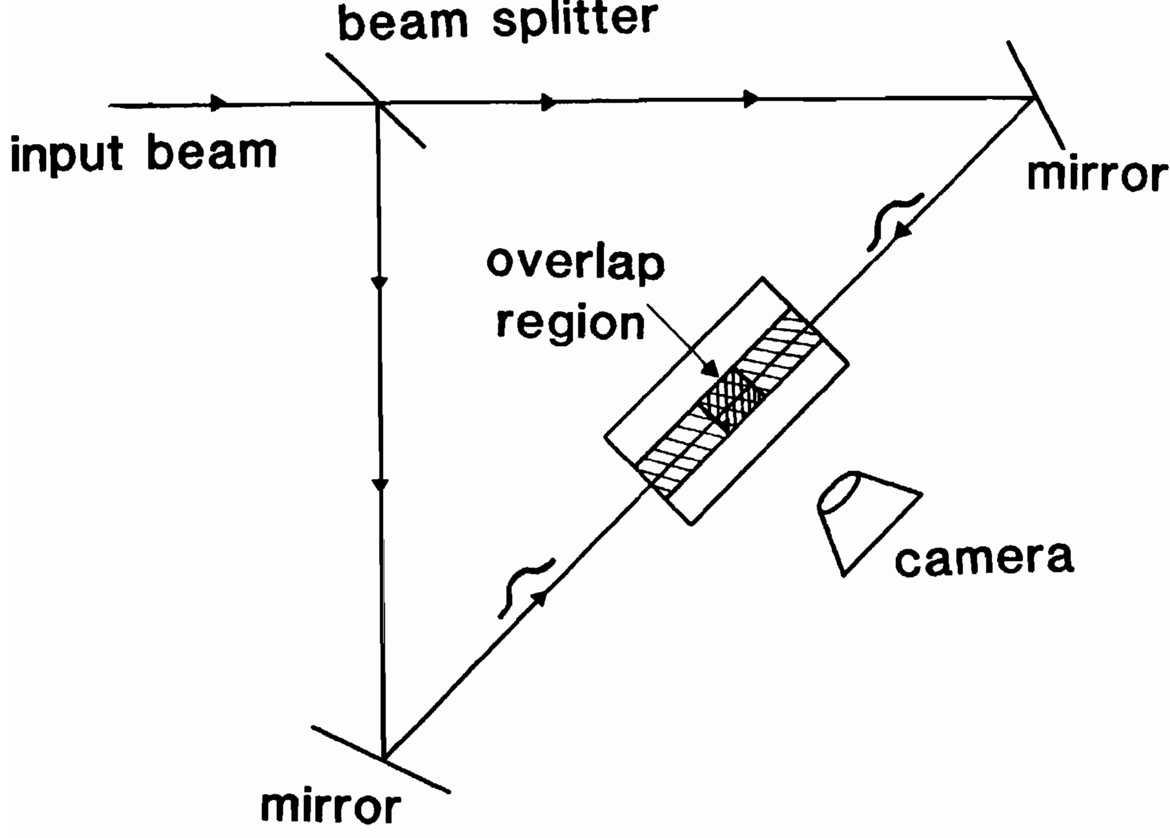

Figure 2. A typical setup for Two Photon Fluorescence. Fluorescence occurs with maximum intensity in the shaded region where the two pulses overlap. The width of this bright region indicates the input pulse width.

times the intensity of the fluorescence. A region of more intense fluorescence then corresponds to pulse overlap, and the width of this region is related to several characteristics of the initial pulse. Extensive studies of this relationship may be found in the literature, a few of which are listed here for reference.[12, 14-18]

Another technique, the optically driven Kerr cell, depends upon the optical Kerr effect.[19] Figure 3 illustrates its operation. Initially, no signal light reaches the film because of the crossed polarizers. An intense gating pulse propagating in the Kerr cell reorients the molecules with respect to the optical electric field, inducing local refractive index changes which alter the polarization of the signal beam as it passes through that portion of the medium. The output polarizer transmits this light to the film. The resulting spot sweeps across the film as the gating pulse propagates down the cell, and the film records the spatially varying spot intensity, which corresponds to the signal pulse intensity profile in time. This technique offers the advantages of low background intensity, direct signal pulse intensity readout, and the possibility of measuring low intensity pulses. Of course, a powerful gating pulse synchronized with the signal pulse must be available. Frequently, satisfaction of this requirement follows from the derivation of both pulses from one source. The first experiments by Duguay and Hansen[20] employed a Kerr cell using carbon disulfide and measured a pulse of 8 picoseconds duration.

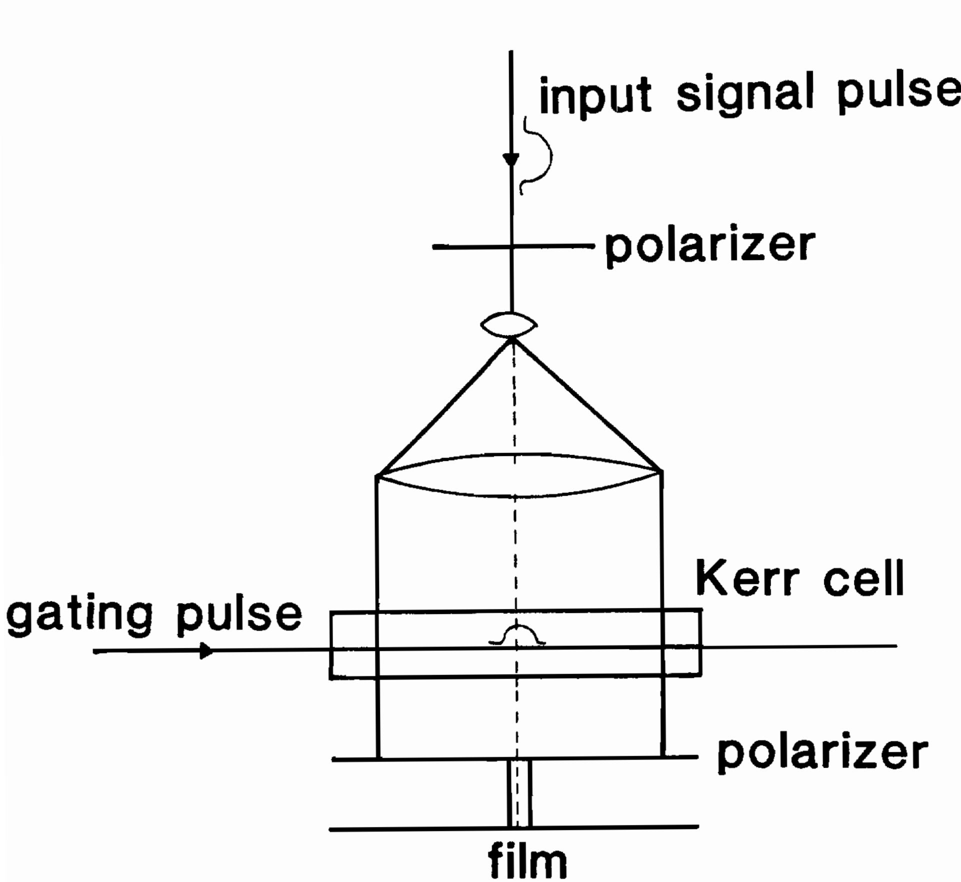

Figure 3. A Kerr cell shutter.
The crossed polarizers keep the signal pulse from reaching the film unless a gating pulse is present. Application of a gating pulse induces polarization changes in the signal pulse which permit light to be transmitted through the region of overlap of the pulses. Signal pulse intensity variations in time then appear as spatial intensity variations along the film.

For low light level measurements without the use of an intense gating pulse, one must use a photoelectron streak camera. Other advantages of this instrument include direct intensity profile readout, operation over a wide spectral range, nearly wavelength independent operation within this range, and resolution times of one to ten picoseconds. Its major disadvantages stem from its limited infrared response, extending at most to about 1.1 micrometers (due to the photocathode), and its relatively high cost. Referring to the simplified illustration of Figure 4, part of the input beam triggers the sweep electronics while the remainder illuminates the photocathode. The emitted electrons are collimated, accelerated, and swept across a phosphor target where a visible streak image forms. After intensification by the pickup camera, the pulse shape data is ready for processing or immediate display. Usually a wide range of resolving times are provided by inclusion of several different sweep rates in the sweep circuitry. A range of several picoseconds to hundreds of picoseconds is not uncommon in commercial instruments, while resolution times below 1 picosecond have been reported.[21]

The preceding descriptions of current display technologies and their limitations point out the lack of a streak camera capable of operation with low light intensities at infrared wavelengths with time resolutions in the picosecond range. Considerable effort has been expended toward extending photocathode operation further into the infrared spectral range. This has resulted in useful photo-cathodes for 1.06 micrometers (as needed for some laser fusion

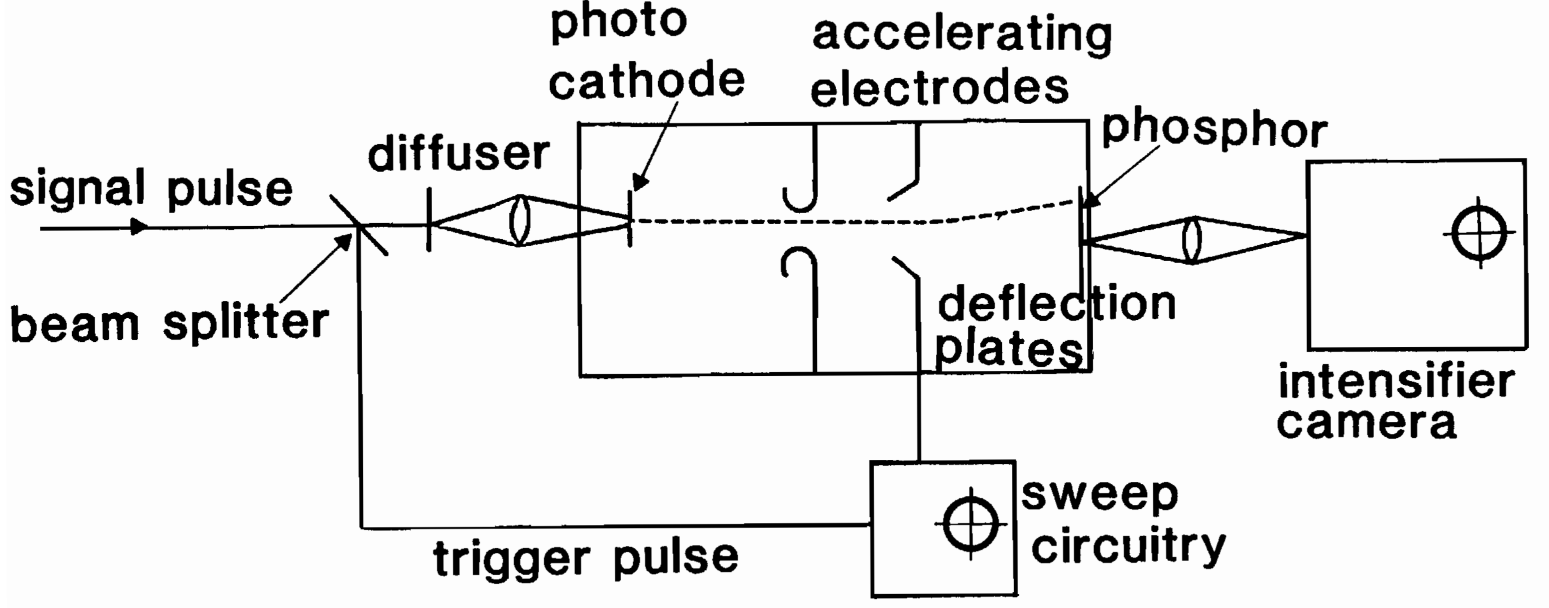

Figure 4. A photoelectron streak camera.
The incoming pulse produces photoelectrons whose current density corresponds to the pulse intensity. This beam is swept across the phosphor to produce an image which is amplified and recorded by the camera for display.

diagnostics), but it will probably never extend their usefulness to wavelengths much longer than this. Thus, a new technique is required to meet this need.

Much research in this field is devoted to methods of direct light beam deflection by use of the linear electrooptic effect exhibited by many materials. An applied electric field induces a change in refractive index which induces a controlled prismatic bending of a light beam passing through the material. This approach leads to a device such as that depicted in Figure 5. The incoming light passes through the deflector, which sweeps the beam axis through some small angle. The imaging lenses then focus the light onto the film where a streak is formed. Part of the incoming light triggers a high voltage sweep circuit in order to actuate the deflector during the passage of the signal. The operation and output of the device appear similar to that of the photoelectron streak camera, but of course the photocathode has been removed, and the light beam is now swept directly. The resulting device is capable of low light level operation from ultraviolet to far infrared wavelengths, thus being able to replace all currently used measurement techniques.

Subsequent chapters of this dissertation will address all aspects of the electrooptic streak camera. Chapter 2 develops the theory of the simple deflection devices described in the literature prior to this research. Comparisons of the various arrangements show that,

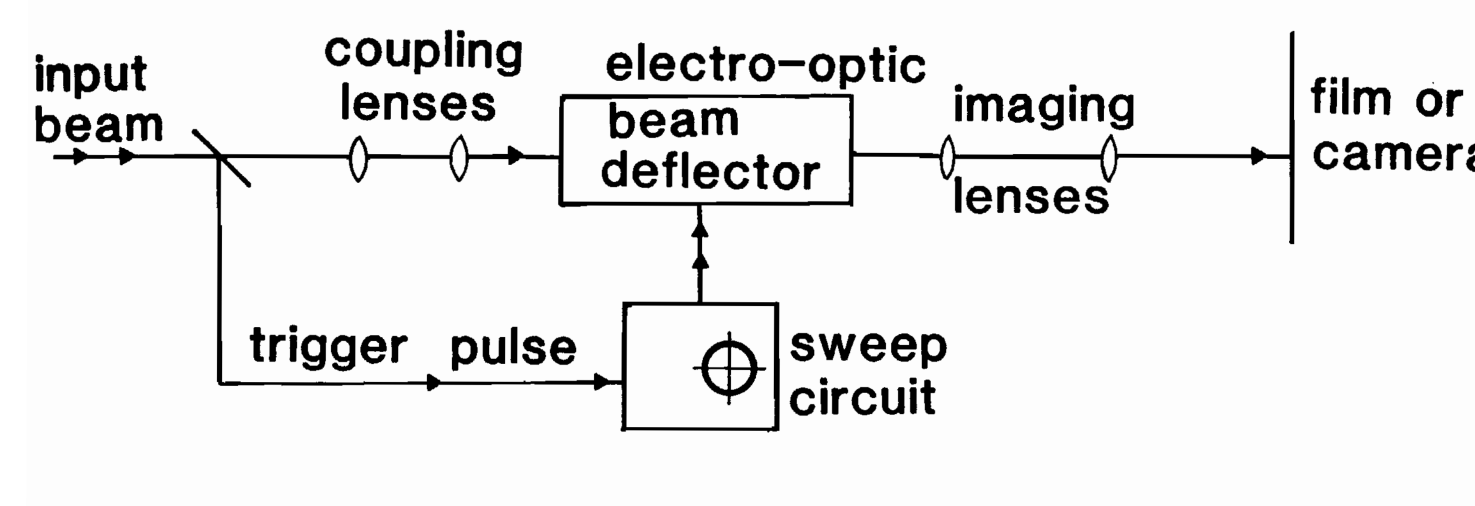

Figure 5. The electrooptic streak camera.
Direct beam deflection results in a simple streak camera design. Operation in all spectral ranges is possible, and it can be used at low light levels.

in theory, they are all essentially equivalent, each being capable of the same performance and subject to the same transit time limitations.

Chapter 3 proposes two new forms of deflectors. These devices, theoretically capable of subpicosecond resolution times, do not exhibit transit time limitations. Ease of construction and performance superiority indicate that the multiple pass traveling lens system is the preferred approach for streak camera design.

Chapters 4 through 6 cover the practical problems involved in demonstrating a useful system. At present, difficulties in generating high voltage, high current, fast risetime pulses prove to be the major limitation. Research in this area is reviewed here.

Chapter 7 describes the streak camera experiments performed in this work. Although they have not extended the state of the art in terms of resolving time or resolvable spots obtained, they represent the first demonstrations of the multiple pass traveling lens system proposed in Chapter 3, and they provide confirmation of the theory therein.

CHAPTER 2

SIMPLE ELECTROOPTIC DEFLECTION TECHNIQUES

When an electric field is applied along particular axes of some crystals, their indices of refraction change. This electrooptic effect has been researched extensively and exploited in many devices. In the linear electrooptic effect, the index change varies linearly with applied field,[22]

$$\Delta n = \tfrac{1}{2} n_o^3 r E = bE \ , \qquad (2.1)$$

n_o being the unperturbed refractive index, r the appropriate electrooptic tensor component relating the electric field and optical polarization directions, and E the applied field. Typically, maximum Δn values are of the order of 10^{-3} to 10^{-4} for the best materials such as lithium niobate and potassium dideuterium phosphate (KDDP).

A number of beam deflection techniques based on the electrooptic effect are in use, including deflection by Bragg diffraction,[23] quadrupole induced index gradients,[24] prisms,[25-27] electrode induced linear field gradients,[28] and a traveling lens design.[29-31] Some of these have been demonstrated in optical waveguides,[23, 27, 28] while the remainder have been in bulk devices; however, each could be demonstrated in a bulk device.

The quadrupole deflector, prism deflector, and lens deflector have received serious consideration for streak camera applications, with the quadrupole system displaying the best experimental

performance so far. These three systems receive close attention in this chapter where it is shown they are each capable of the same theoretical performance, with some differences occurring in practice. The literature contains several excellent reviews of prism and gradient type bulk devices,[26, 32, 33] but none of them cover transit time effects as discussed here.

2.1 Quadrupole Gradient Deflectors

Figure 6 shows a quadrupole device capable of deflection by production of an index gradient. As shown in Appendix 1, hyperbolic electrodes provide a linear electric field gradient (Figure 6b) given by

$$\partial E_z/\partial y = -2V_o/R^2 . \tag{2.2}$$

Also $n = n_o - bE$, so that $\partial n/\partial y = b\partial E/\partial y$ specifies the resulting index gradient. The deflection angle may be found by noting that the radius of curvature of a light path in a medium with a constant index gradient is[34]

$$\rho = 1/\nabla \log n \approx n_o/\nabla n = n_o/(\partial n/\partial y) = n_o R^2/2bV_o \tag{2.3}$$

and the approximate deflection angle is then

$$\theta \approx \ell/\rho = 2bV_o \ell/n_o R^2 \tag{2.4}$$

before exit from the crystal. Applying Snell's law at the crystal to air exit interface gives the external deflection angle

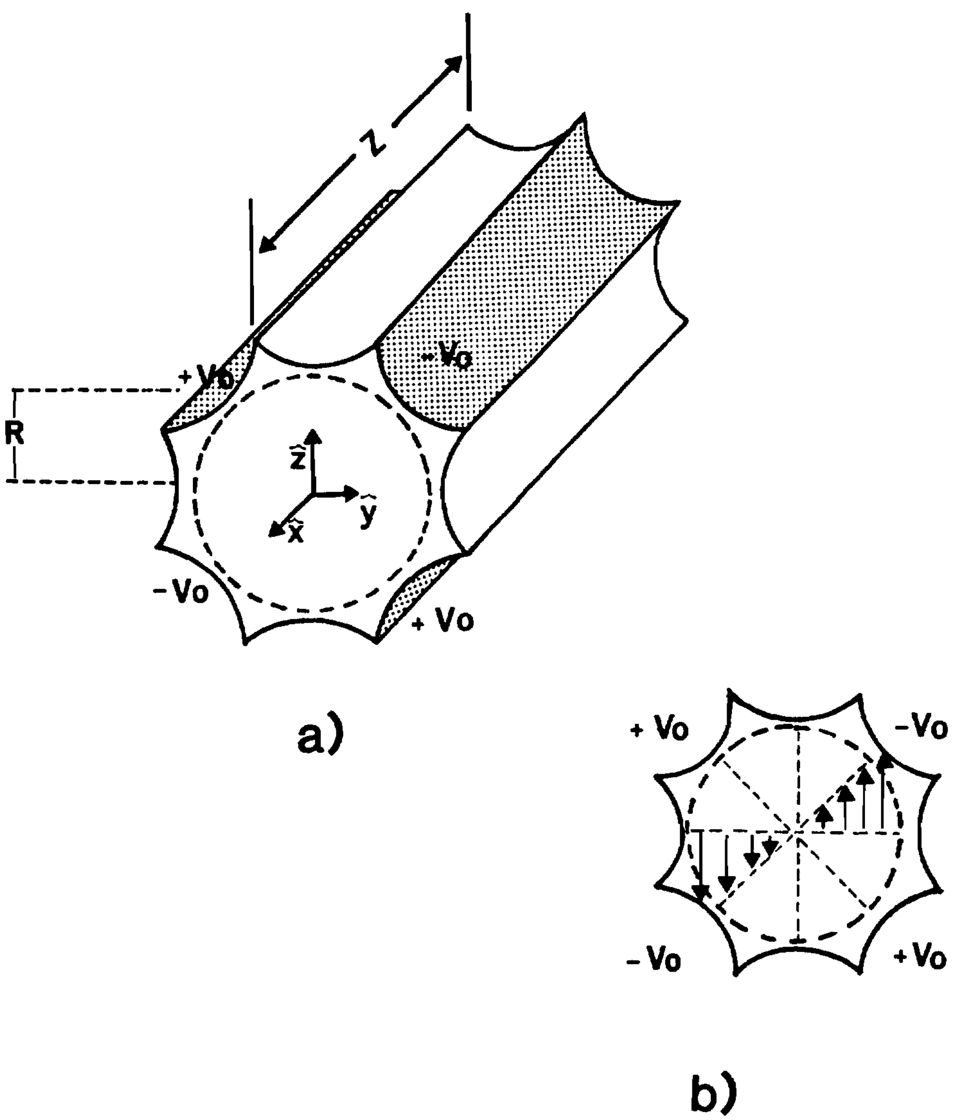

Figure 6. a) The basic quadrupole deflector arrangement. Hyperbolic electrodes induce a linear field gradient (b) which may be used to deflect a light beam.

$$\theta_1 = 2bV_o \ell / R^2 \, . \tag{2.5}$$

An alternative and more general technique for determination of the deflection angle takes note of the fact that the path length change at the edge of the beam is given by

$$\Delta p = bE\ell = 2bV_o \ell w / R^2 \tag{2.6}$$

while at the center of the beam it is given by $\Delta p = 0$, and hence the deflection angle is

$$\theta_1 = \Delta p / w = 2bV_o \ell / R^2 \tag{2.7}$$

for a beam of radius w.[35] The usefulness of this deflector is determined by the number of resolvable spots as defined by

$$N = \theta_1 / \beta = \pi b V_o \ell w / \lambda R^2 \tag{2.8}$$

where $\beta = 2\lambda/\pi w$ is the full angular divergence of the Gaussian beam determined by the $1/e^2$ intensity points of the far field pattern,[36] and where w is again the beam radius in the crystal.

Equation (2.8) gives the d.c. (low speed) deflection formula. For high deflection rates it becomes necessary to include the effects of the changing field that the light encounters as it propagates through the crystal. For a voltage increasing linearly with time, the field at any point in the crystal is a function of time and position. Integrating Δn over the length of the crystal then gives

the total path length change. With t_o being the ramp time, t the time at which light enters the crystal relative to the start of the ramp, and x the distance traveled by the light into the crystal, we have

$$V = V_o(t + n_o x/c)/t_o \quad \text{for} \quad t + n_o \ell/c \leq t_o \quad \text{and } 0 \leq x \leq \ell \qquad (2.9)$$

where the time constraint insures the voltage will be rising during the entire interaction time. The corresponding path length change, deflection angle, and number of resolvable spots as functions of time are then:

$$\begin{aligned} \Delta p &= \int_o^\ell bE\{w\}\, dx = b \int_o^\ell 2Vw/R^2 dx \\ &= 2bV_o w\, (t\ell + \ell^2 n_o/2c)/t_o R^2 \\ \theta_1 &= \Delta p/w = 2bV_o(t\ell + \ell^2 n_o/2c)/t_o R^2 \\ N &= \theta_1/\beta = \pi wbV_o(t\ell + \ell^2 n_o/2c)/\lambda t_o R^2 \, . \end{aligned} \qquad (2.10)$$

One final quantity of interest is the resolving time, which may be defined as the time required for the beam to sweep across each spot, i.e.,

$$\tau_R = 1/(dN/dt) = R^2 \lambda t_o/\pi bV_o \ell w \, . \qquad (2.11)$$

The number of spots in the usable ramp time, $t_\mu = t_o - nl/c$, is obtained by substituting t_μ for t in Equation (2.10) giving

$$N_l = \pi b V_o \ell w(t_o - n\ell/c)/\lambda t_o R^2 . \quad (2.12)$$

To minimize t_R, the ramp time t_o must be as small as possible, whereas the maximum number of spots requires t_o large. This tradeoff always occurs when considering transit time effects. For fixed t_o the maximum number of spots occurs when $\ell = ct_o/2n$ giving

$$N_m = \pi b V_o c t_o w/4\lambda R^2 n_o$$
$$\tau_m = 2\lambda R^2 n_o/\pi w b V_o c . \quad (2.13)$$

For practical deflectors the capacitance of the device is also of interest. As shown in Appendix 1 this is given by

$$C = \varepsilon_o \ell(\varepsilon_\parallel + \varepsilon_\perp) \quad (2.14)$$

when the optic axis of a uniaxial material is along either the y or z axes shown in Figure 6a. Here, ε_o is the permittivity of the vacuum, and $\varepsilon_\parallel$ and $\varepsilon_\perp$ are the relative dielectric constants for an electric field parallel and perpendicular to the crystal optic axis.

Using this arrangement Ireland[24] has demonstrated a resolution time of 20 picoseconds in a practical device without compensating for the optical transit time. This represents the best resolution obtained to date by an electrooptic streak camera.

2.2 Prism Deflectors

Prism type deflectors were suggested almost as early[37] as quadrupole deflectors, and they have received considerably more

attention. Lee and Zook[26] published an excellent review of prism techniques which covers nearly all aspects of their design and use; they did not, however, consider transit time effects. These effects in prism systems have been analyzed and discussed in conjunction with the research being described in this dissertation.[31] The most impressive low speed demonstration of the prism deflection technique was accomplished by Beasley[38] who built a prototype television projection system using electrooptic scanning of a laser beam. He obtained several hundred resolvable spot positions, a very exceptional result.

A simple prism deflector is illustrated in Figure 7. It consists of two right angle prisms sandwiched between electrodes on top and bottom. The crystal axes of the prism material are oriented so that application of a potential, V_o, to the electrodes decreases the index of refraction of the first prism and increases that of the second prism for light of a given polarization.

The angle through which the light beam is deflected by a static field is easily found by applying Snell's law at the interface of the prisms. This yields

$$\theta = \ell \Delta n / w n_o = \ell b V_o / w n_o d \qquad (2.15)$$

provided $\Delta n \ll n_o$ and $\theta \ll 1$. To determine the device characteristics when a time varying field is applied, we again apply the technique of computing the induced path length changes. Referring to

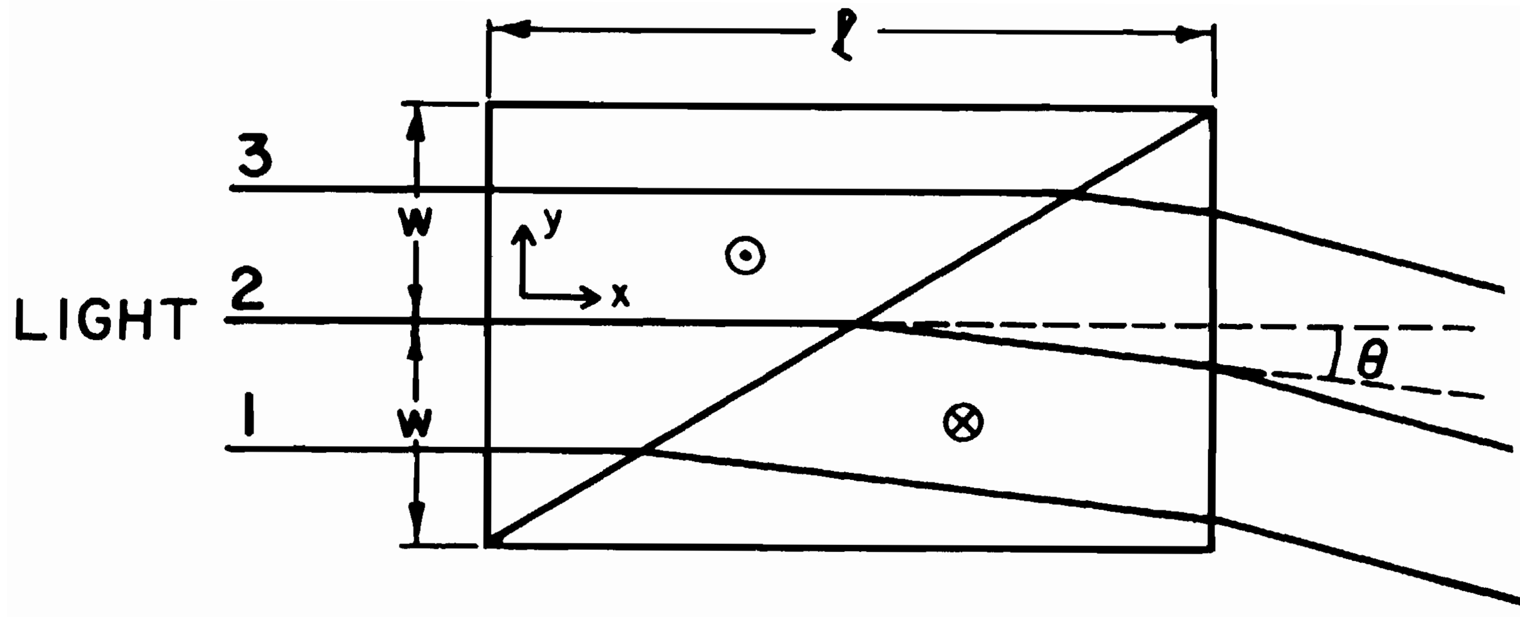

Figure 7. The basic two-prism deflector.
The symbols ⊗ and ⊙ indicate that the crystallographic c-axes of the lithium niobate crystals are oriented in the negative and positive z directions respectively. The electric field is in the +z direction. The directions of the x and y axes of the right handed coordinate systems are also indicated.

the coordinate system of Figure 7, the path length change for rays at $y = \pm w$ is just $\mp \ell \Delta n / w n_o$, and the resulting wavefront tilt or deflection angle is $\theta = \ell \Delta n / w n_o$ as before.

Next, we consider the effect of an applied voltage ramp,

$$V\{t\} = \begin{cases} 0 & ; \quad t < 0 \\ V_o t/t_o & ; \quad 0 \le t \le t_o \\ V_o & ; \quad t > t_o \end{cases} \tag{2.16}$$

on the light beam. The induced path length change for a ray which enters the first prism at y at time t and leaves the second prism at time $t + n_o \ell / c$ is

$$\Delta p\{y,t\} = \frac{b}{n_o d} \left[- \int_o^u V\{t + n_o x/c\}\, dx + \int_u^\ell V\{t + n_o x/c\}\, dx \right] \tag{2.17}$$

with $u = (1 + y/w)\ell/2$ being the abscissa of the point where the ray crosses the interface between the two prisms. Substituting for V{t} from (2.16) and integrating yields

$$\Delta p\{y,t\} = \frac{bV_o}{n_o t_o d} \left[\frac{n_o \ell^2}{4c} - \frac{n_o \ell^2 y}{2cw} - \frac{n_o \ell^2 y^2}{4cw^2} - \frac{y \ell t}{w} \right] \tag{2.18}$$

provided t is restricted to the interval $0 < t < t_o - n_o \ell / c$.

The first three terms in (2.18) are time independent. The first corresponds to a static delay of the wavefront due to the fact that the beam passes first through a lower and then a higher index material while the magnitude of the index difference is increasing. The second term is linear in the transverse coordinate, y, and represents a static wedge, while the third term is quadratic and represents a lens whose focal length, in the paraxial approximation, is $f = 2w^2 ct_o d/V_o b\ell^2$. This focusing effect, while at first sight surprising, is readily understood by a ray tracing argument illustrated in Figure 7. Consider the three rays indicated. Each follows a straight line up to the interface between the two prisms and again between the interface and the exit from the second prism, but at the interface, rays 1, 2, and 3 are deflected through progressively larger angles since the index difference is increasing with time and the rays reach the interface at progressively later times. The deflection angle varies linearly across the beam, and the effect is the same as a wedge plus lens combination. The focusing effect can be compensated for with auxiliary optics.

The last term in Equation (2.18) represents a deflection which increases linearly with time over the interval $0 < t \leq t_o - n_o\ell/c$. The deflection angle for a beam entering the first prism at time t is then

$$\theta\{t\} = \frac{\ell b V_o}{n_o w t_o d}\,(t + n_o\ell/c) = \frac{\ell b V_o t}{n_o w t_o d} + \theta\{0\} \qquad (2.19)$$

where the second term is due to the static wedge discussed above. The angular range of the deflection which occurs within the usable time interval, $0 \leq t \leq t_o - n_o\ell/c$, is

$$\theta_m = \theta\{t - n_o\ell/c\} - \theta\{0\} = \ell bV_o(t_o - n_o\ell/c)/n_o w t_o d \,. \qquad (2.20)$$

During the time intervals $-n_o\ell/c < t < 0$ and $t_o - n_o\ell/c < t < t_o$ different parts of the beam are deflected through different angles introducing severe aberrations which cannot be readily corrected.

As with the quadrupole deflector the usefulness of this device is determined by the number of resolvable spot positions traversed during the sweep. For small deflection angles this is given by $N = \theta_m/\beta$ where β is again the full angular beam divergence, $\beta = 2\lambda/\pi n_o w$. However, for larger deflections, the beam will hit the sides of the device unless proper external focusing is employed. Lee and Zook[26] have treated this geometrical constraint, and they find that the optimum f-number of the beam is $2/\theta_m$. This reduces the number of resolvable spots somewhat and the correct formula becomes

$$N = \frac{\theta_m}{\beta}\left(1 - \frac{\theta_m \ell}{8w}\right) = \frac{\pi n_o \theta_m w}{2\lambda}\left(1 - \frac{\theta_m \ell}{8w}\right) . \qquad (2.21)$$

This formula may be used for any device in which the deflection appears to originate at a point halfway between the entry and exit faces of the device. Reference to this formula will be made in a later section. Substituting θ_m as given in (2.20) yields

$$N = \frac{\pi b V_o}{2\lambda d}\left[\ell\left(1 - \frac{n_o \ell}{c t_o}\right) - \frac{b V_o \ell^3}{8 w^2 n_o d}\left(1 - \frac{n_o \ell}{c t_o}\right)^2\right]. \tag{2.22}$$

This is a maximum when w is large, in which case

$$N = \frac{\pi b V_o \ell}{2\lambda d}\left(1 - \frac{n_o \ell}{c t_o}\right). \tag{2.23}$$

The minimum resolvable time, τ, is just the usable time interval, $t_o - n_o\ell/c$, divided by N, which gives

$$\tau = 2\lambda t_o d/\pi \ell b V_o . \tag{2.24}$$

As with the quadrupole arrangement the maximum number of spots occurs for $\ell = ct_o/2n_o$ yielding

$$N_m = \frac{\pi b V_o c t_o}{8\lambda n_o d}$$

$$\tau_m = \frac{4\lambda n_o d}{\pi b V_o c} . \tag{2.25}$$

A number of other prism arrangements have been described in the literature.[25, 26, 32, 39] Analysis along the lines given here shows them all to be essentially equivalent to a single prism of length ℓ', ℓ' being the total interaction length of the light and the active material. Their main advantage is a practical one: they exhibit less capacitance than the equivalent single prism device. For a simple parallel plate capacitor the capacitance is given by

$$C = \varepsilon_{\parallel}\varepsilon_o A/d = \varepsilon_{\parallel}\varepsilon_o(2w\ell)/d \, . \tag{2.26}$$

2.3 Traveling Lens Deflector

The traveling lens deflector is a recent development in the field of electrooptic deflection, being originally proposed in 1976.[29] It has received little attention other than that given in this dissertation and related publications;[30, 31] however, it shows considerable promise in streak camera applications.

Figure 8 illustrates the traveling lens deflector. A parabolic voltage pulse propagating in the y direction forms a lens which focuses the light beam as it passes through the crystal in the x direction. The focal spot is then carried along with the lens, effectively generating deflection.

For a parabolic voltage pulse of width $2Y_1$ in the crystal,

$$V\{y,t\} = V_1[1 - (y - tc/\sqrt{\varepsilon})^2/Y_1^2] \; ; \qquad |y - tc/\sqrt{\varepsilon}\,| \leq Y_1 \tag{2.27}$$

an index change of

$$\Delta n\{y,t\} = bV_1[1 - (y - tc/\sqrt{\varepsilon})^2/Y_1^2]/d \tag{2.28}$$

occurs. The induced path length difference due to this disturbance for a ray entering the crystal at y at time t is

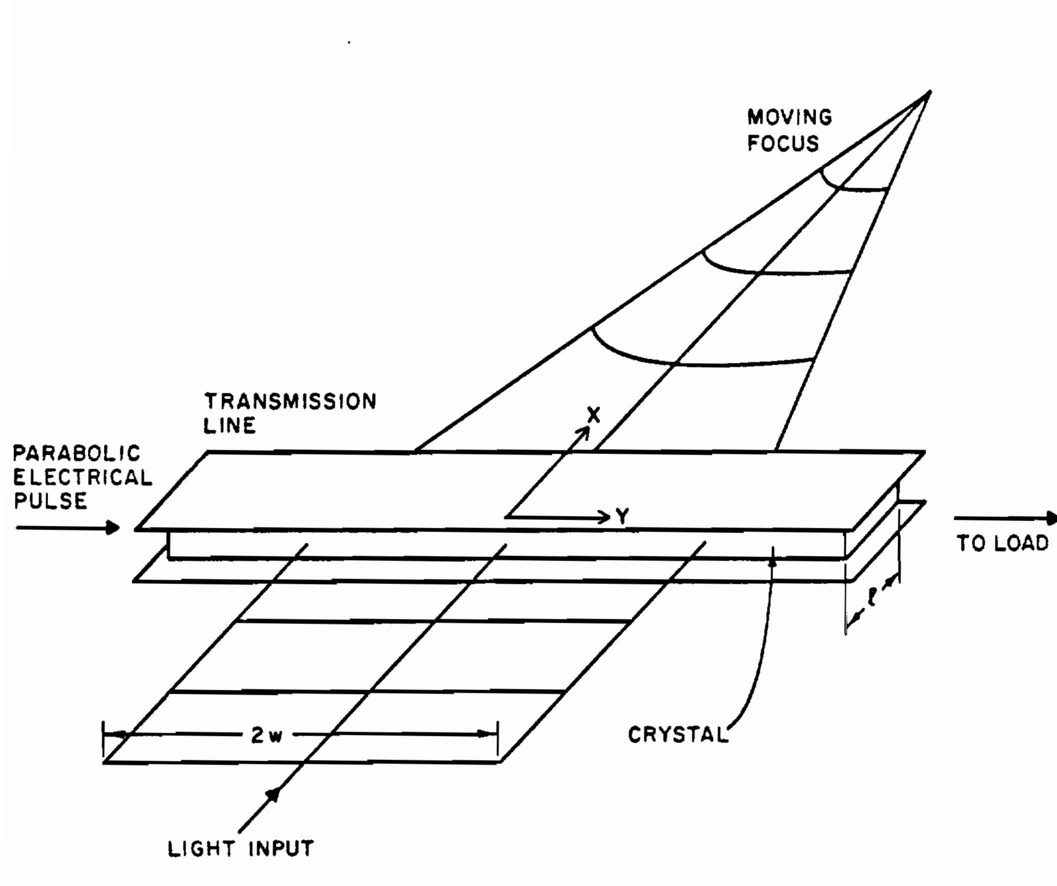

Figure 8. The traveling lens deflector.
The parabolic voltage pulse induces a lens whose focus moves as the pulse propagates down the waveguide.

$$\Delta p\{y,t\} = \int_o^{\ell} \Delta n\{y,\ t + n_o x/c\} d_x$$

$$= \frac{bV_1\ell}{d} [1 - (y - tc/\sqrt{\varepsilon})^2/Y_1^2 \qquad (2.29)$$

$$- n_o\ell(y - t_c/\sqrt{\varepsilon})/Y_1^2\sqrt{\varepsilon} - n_o^2\ell^2/3\varepsilon Y_1^2] .$$

This is quadratic in y and corresponds to a cylinder lens moving down the guide with speed $c/\sqrt{\varepsilon}$ whose center is $n_o\ell/\sqrt{\varepsilon}$ behind the peak of the voltage pulse. The focal length of this induced cylinder lens is, in the paraxial approximation,

$$f = Y_1^2 d/2bV_1\ell . \qquad (2.30)$$

It can focus an initially plane Gaussian beam of half width w to a beam of halfwidth

$$w_o = \beta f = \lambda f/\pi w = \lambda Y_1^2 d\sqrt{\varepsilon}/\pi bV_1\ell wc . \qquad (2.31)$$

The focal spot produced by this lens translates at the same speed as the electrical pulse in the wave guide, $c/\sqrt{\varepsilon}$, which means that the time for the focused beam to traverse one spot width, i.e. the resolving time, is

$$\tau = 2w_o\sqrt{\varepsilon}/c = \lambda Y_1^2 d\sqrt{\varepsilon}/\pi bV_1\ell wc . \qquad (2.32)$$

The optical signal will be properly focused and displayed only if there is complete overlap with the voltage pulse. The duration of the voltage pulse is $2Y_1\sqrt{\varepsilon}/c$, and the transit time for light in the crystal is $n_o\ell/c$. Thus there is coincidence for times $0 \leq t \leq t_1$ with t_1 given by

$$t_1 = [\,2\sqrt{\varepsilon}(Y_1 - w) - n_o\ell]/c\,. \tag{2.33}$$

The number of spot widths swept in this time, the number of resolvable spots, is

$$N = t_1/\tau = \pi b V_1 \ell w\,[\,2(Y_1 - w) - n_o\ell/\sqrt{\varepsilon}\,]/\lambda Y_1{}^2 d\,. \tag{2.34}$$

Maximizing this with respect to w gives $2w = Y_1 - n_o\ell/2\sqrt{\varepsilon}$ and then

$$N = \frac{\pi b V_1 \ell (Y_1 - n_o\ell/2\sqrt{\varepsilon})^2}{2\lambda Y_1{}^2 d}$$

$$\tau = \frac{2\lambda Y_1{}^2 d\sqrt{\varepsilon}}{\pi b V_1 \ell c (Y_1 - n_o\ell/2\sqrt{\varepsilon})}\,. \tag{2.35}$$

Finally, defining the voltage time duration in terms of t_o, the time required to reach maximum voltage, gives $Y_1 = ct_o/\sqrt{\varepsilon}$ and

$$N = \left(\frac{\pi b V_1 \ell}{2\lambda d}\right)\left(\frac{t_o - n_o\ell/2c}{t_o}\right)^2$$

$$\tau = \left(\frac{2\lambda d t_o}{\pi b V_1 \ell}\right)\left(\frac{t_o}{t_o - n_o\ell/2c}\right)\,. \tag{2.36}$$

In practical applications the stripline impedance is important and is given by [40]

$$Z = \frac{120\pi/\sqrt{\varepsilon}}{\ell/d + 0.441 + \frac{(\varepsilon+1)}{2\pi\varepsilon}\,[\ln(\ell/d + 0.94) + 1.451] + \frac{(\varepsilon-1)}{\varepsilon^2}\,(0.082)} \tag{2.37}$$

for striplines having $\ell > d$. When $\ell >> d$ this simplifies to

$$Z = \frac{120\pi d}{\ell\sqrt{\varepsilon}}\ . \tag{2.38}$$

2.4 Comparisons

To compare the various configurations, a few assumptions must be made to cast the formulae into similar forms. For the quadrupole case, assuming that $w = R$ and requiring that the internal field never exceed the material dielectric field strength $2V_o/R = E_m$, Equations (2.12) and (2.11) then show

$$N_q = \left(\frac{\pi b E_m \ell}{2\lambda}\right)\left(\frac{t_o - n_o \ell/c}{t_o}\right)$$

$$\tau_q = \frac{2\lambda t_o}{\pi b E_m \ell}\ . \tag{2.39}$$

For the prism case one can assume $V_o/d = E_m$ and use Equations (2.23) and (2.24) to derive

$$N_p = \left(\frac{\pi b E_m \ell}{2\lambda}\right)\left(\frac{t_o - n_o \ell c}{t_o}\right)$$

$$\tau_p = \frac{2\lambda t_o}{\pi b E_m \ell} \; . \qquad (2.40)$$

Finally, with $V_o/d = E_m$ Equations (2.36) lead to the corresponding lens formulae

$$N_\ell = \left(\frac{\pi b E_m \ell}{2\lambda}\right)\left(\frac{t_o - n_o \ell/2c}{t_o}\right)^2$$

$$\tau_\ell = \left(\frac{2\lambda t_o}{\pi b E_m \ell}\right)\left(\frac{t_o}{t_o - n\ell/c}\right) . \qquad (2.41)$$

For the usual case of $t_o >> n_o \ell/c$, the lens equations approach the preceding equations for the quadrupole and prism deflectors. Note that setting $2w = Y_1$ in Equations (2.32) and (2.34) for the lens rather than the optimum value of w results in

$$N_\ell = \left(\frac{\pi b E_m \ell}{2\lambda}\right)\left(\frac{t_o - n\ell/c}{t_o}\right)$$

$$\tau_\ell = \frac{2\lambda t_o}{\pi b E_m \ell} \; . \qquad (2.42)$$

All three devices have identical characteristics under these conditions. Thus, for simple deflectors the number of spots and the resolving time are a function of the interaction length, voltage ramp time, and various material parameters.

Having demonstrated the operational equality of these devices, another point of comparison is the volume of material required to produce the specified characteristics. The independent variables for volume determination are ℓ, t_o, V_o, and E_m (E_m frequently is determined by factors other than dielectric breakdown strength). For the quadrupole deflector, R is limited by E_m to $R = 2V_o/E_m$ giving an approximate volume of $V_q = \ell(2R)^2 = \ell(4V_o/E_m)^2$. For the lens system d is given by $d = V_o/E_m$, and the required crystal width is given by $2w = Y_1 = ct_o/\sqrt{\varepsilon}$. Then $V_\ell = Y_1 \ell d = ct_o \ell V_o/E_m\sqrt{\varepsilon}$ is the required volume. The prism deflector presents a more difficult calculation. As with the lens system $d = V_o/E_m$; however, the width, 2w, is governed by two constraints. The first is $w >> \theta_m \ell/8$ as required in the operational comparison, and the second is $\theta_m << 1$ as required in the original derivation. These conditions can usually be satisfied by requiring $2w \geq d$.

Table 1 summarizes these results. The prism system always requires less volume than the quadrupole system. This is due to the nonuniform field and the requirement that voltages of plus and minus V must be applied in the quadrupole case. If $Y_1 >> d$ is required for the lens (a practical constraint normally), then the lens volume is always greater than or equal to the prism volume and will usually be much larger. Thus, the prism deflector usually requires considerably less material to obtain a given set of performance characteristics than either the lens or quadrupole systems.

TABLE 1

SIMPLE DEFLECTOR VOLUME COMPARISONS

	Length	Width	Height	Volume
Quadrupole Deflector	ℓ	$2R = \frac{4V_o}{E_{max}}$	$2R = \frac{4V_o}{E_{max}}$	$\ell\left(\frac{4V_o}{E_{max}}\right)^2$
Prism Deflector	ℓ	$> \frac{V_o}{E_{max}}$	$d = \frac{V_o}{E_{max}}$	$> \ell\left(\frac{V_o}{E_{max}}\right)^2$
Lens Deflector	ℓ	$Y = \frac{ct_o}{\sqrt{\varepsilon}}$	$d = \frac{V_o}{E_{max}}$	$\frac{ct_o \ell V_o}{E_{max}\sqrt{\varepsilon}}$

Since the most important practical limitation in using these devices is the pulse generator, the capacitance and impedance of these devices are also of importance. From Equations (2.39) - (2.42) the number of spots per unit length is given approximately by

$$N/\ell = \pi b E_m / 2\lambda \tag{2.43}$$

for the common case of $t_o >> n_o \ell / c$. For the quadrupole system the capacitance per unit length, given by Equation (2.14), may be used to obtain the capacitance per spot

$$C/N = [\epsilon_o(\epsilon_\parallel + \epsilon_\perp)](2\lambda/\pi b E_m) . \tag{2.44}$$

Similarly, for the prism systems

$$C/N = [\epsilon_o \epsilon_\parallel (2w/d)](2\lambda/\pi b E_m) . \tag{2.45}$$

Practical prisms usually require $2w/d >> 1$. Consequently, for most materials the quadrupole system will entail less capacitance per spot than the prism system.

Comparison with the traveling lens system is more difficult and will not be done here. Since the traveling lens system usually requires much more material than the quadrupole or prism systems, the latter would normally be preferable.

Before leaving the topic of simple lumped deflection systems, one final limitation of these devices requires some emphasis. As discussed earlier a tradeoff always exists between the number of spots

obtainable and the resolving time. When t_o is as small as possible the best resolution time is obtained. However, t_o must exceed the transit time, $\ell n/c$. Thus, the best resolution time (corresponding to the case of zero spots) occurs for $t_o = \ell\sqrt{\varepsilon}/c$ giving the result

$$\tau_{Rm} = 4\lambda/\pi n_o^2 rcE_m \tag{2.46}$$

which is dependent only upon the material chosen and the wavelength. For $\lambda = 1\mu m$ and $E_m = 10^7 V/m$, we have

for $LiNbO_3$: $n_o = 2.2$, $r = 30.8 \times 10^{-12} m/V$, $\varepsilon_\parallel = 26.4$, and $\tau_{Rm} = 2.8$ ps

and for KDDP : $n_o = 1.5$, $r = 23.6 \times 10^{-12} m/V$, $\varepsilon_\parallel = 48$, and $\tau_{Rm} = 7.9$ ps. (2.47)

Conventional photoelectron streak cameras offer picosecond resolution with 25 to 100 spots resolution. Therefore, no simple electrooptic deflection system is likely to replace them in the spectral region of $\lambda < 1\mu m$ on the basis of performance alone, although there may be valid economic reasons for using electrooptic devices. Since the electrooptic deflector resolution deteriorates for longer wavelengths, these simple deflectors do not show great promise in the infrared region either. These results are due to the limitation imposed by transit time of the light through the crystal. The next several sections deal with a method of overcoming this limitation.

CHAPTER 3

DEFLECTION SYSTEMS WITHOUT TRANSIT TIME LIMITATIONS

The previous chapter dealt with simple deflection systems all of which were subject to transit time limitations. In this chapter we examine systems which perform without this limitation. By placing a series of simple deflectors side by side, a strip transmission line may be constructed. The arrangements for the prism and lens devices are illustrated in Figures 9 and 10. The voltage pulse propagates down the line while the light beam traverses back and forth across the line. The dimensions are chosen to maintain synchronism between the voltage pulse and light pulse to allow many interactions of the two. By choosing the correct angle of crossing for the lens system exact synchronism can be maintained and no transit time effect occurs. For the prism arrangement a small transit time effect due to one pass through the line (simple prism effect) occurs, but it is quite small.

A single pass traveling lens deflector can be constructed which is free of transit time effects. By adjusting the angle of incidence in the simple lens deflector, the light and voltage pulses can be propagated with exact synchronism, thereby eliminating transit time effects. The interaction length may then be increased far beyond the restriction imposed by transit time. Practical problems involving the stripline impedance and required voltage pulse source, however, limit the

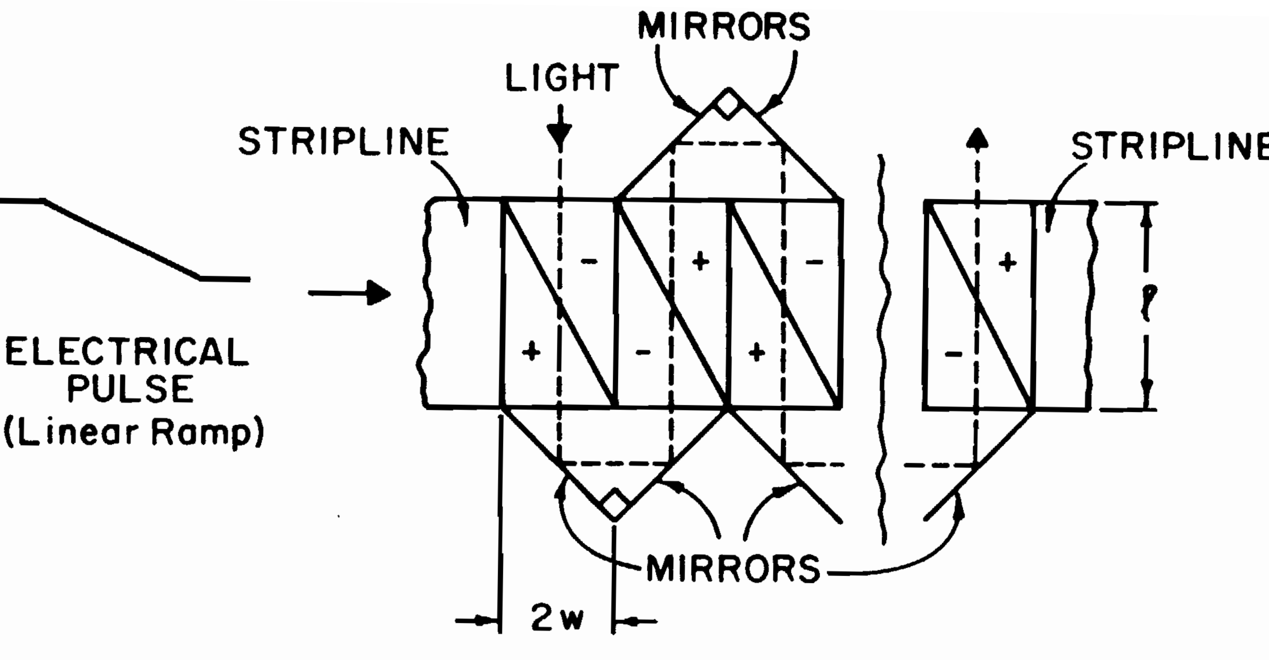

Figure 9. The multiple prism stripline deflector.
The + and - signs indicate the relative change in refractive index induced by the field.

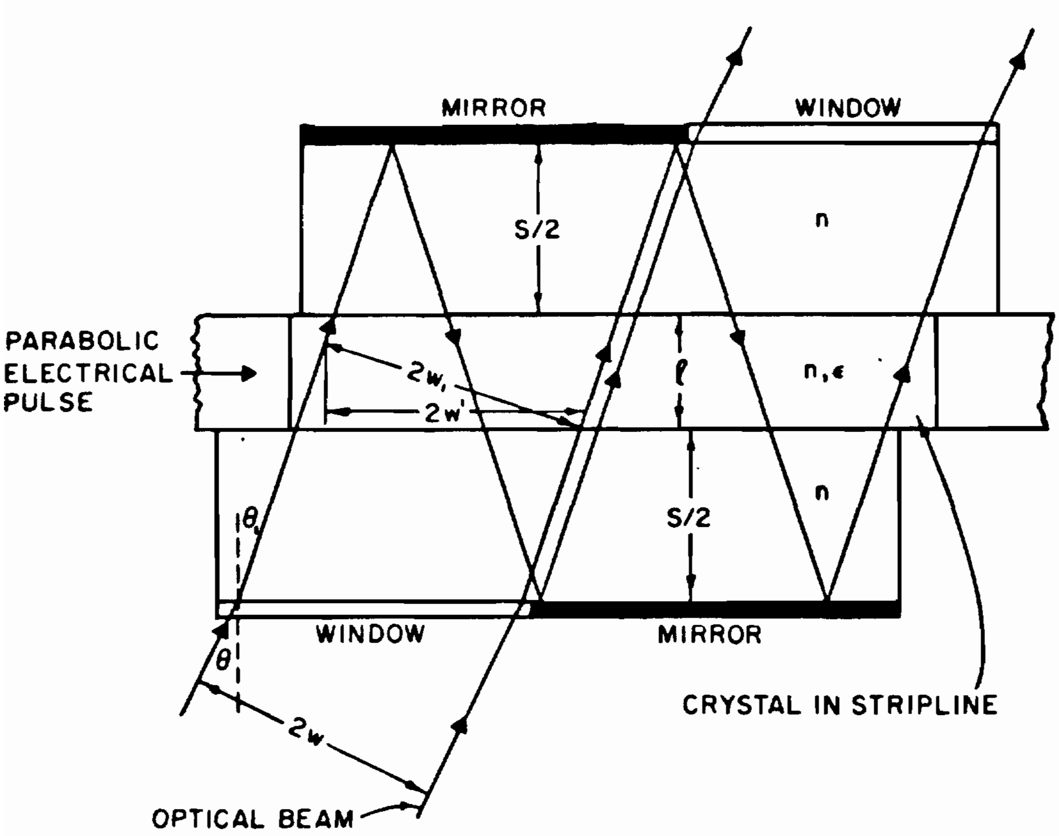

Figure 10. The iterated traveling lens deflector. The angle $\theta_1 = \arcsin(n/\sqrt{\varepsilon})$ is such that a point on the optical wavefront maintains exact coincidence with the same point on the electrical waveform The space between the edges of the stripline and the mirrors is filled with an index matching substance.

usefulness of this arrangement. For completeness it is analyzed at the end of this chapter.

3.1 Multiple Prism System

Before considering multiple prism systems in detail we must modify the analysis of the simple prism deflector given in Chapter 2 to include the effects of a voltage ramp moving across the prism due to its inclusion in the stripline structure. The analysis follows the previous one closely. Referring to Figure 11, the voltage is uniform in the direction of light propagation at any given instant but is a linear ramp in the direction of the waveguide axis, the y direction. The performance of the stripline prism deflector may be readily determined by the path length techniques of the previous chapter. The time origin is chosen so that the voltage ramp is present in the prisms at t = 0

$$V\{y,o\} = V_o w(1 - y/w)/Y_o \tag{3.1}$$

with $Y_o = ct_o/\sqrt{\varepsilon}$, t_o being the duration of the voltage ramp. Then, the induced path length change for a ray entering at (0,y) at time t becomes

$$\Delta p\{y,t\} = \frac{bV_o}{Y_o nd}\left[-\int_o^u (w - y + tc/\sqrt{\varepsilon} + n_o x/\sqrt{\varepsilon}\,)dx + \int_u^\ell (w - y + tc/\sqrt{\varepsilon} + n_o x/\sqrt{\varepsilon}\,)dx \right] \tag{3.2}$$

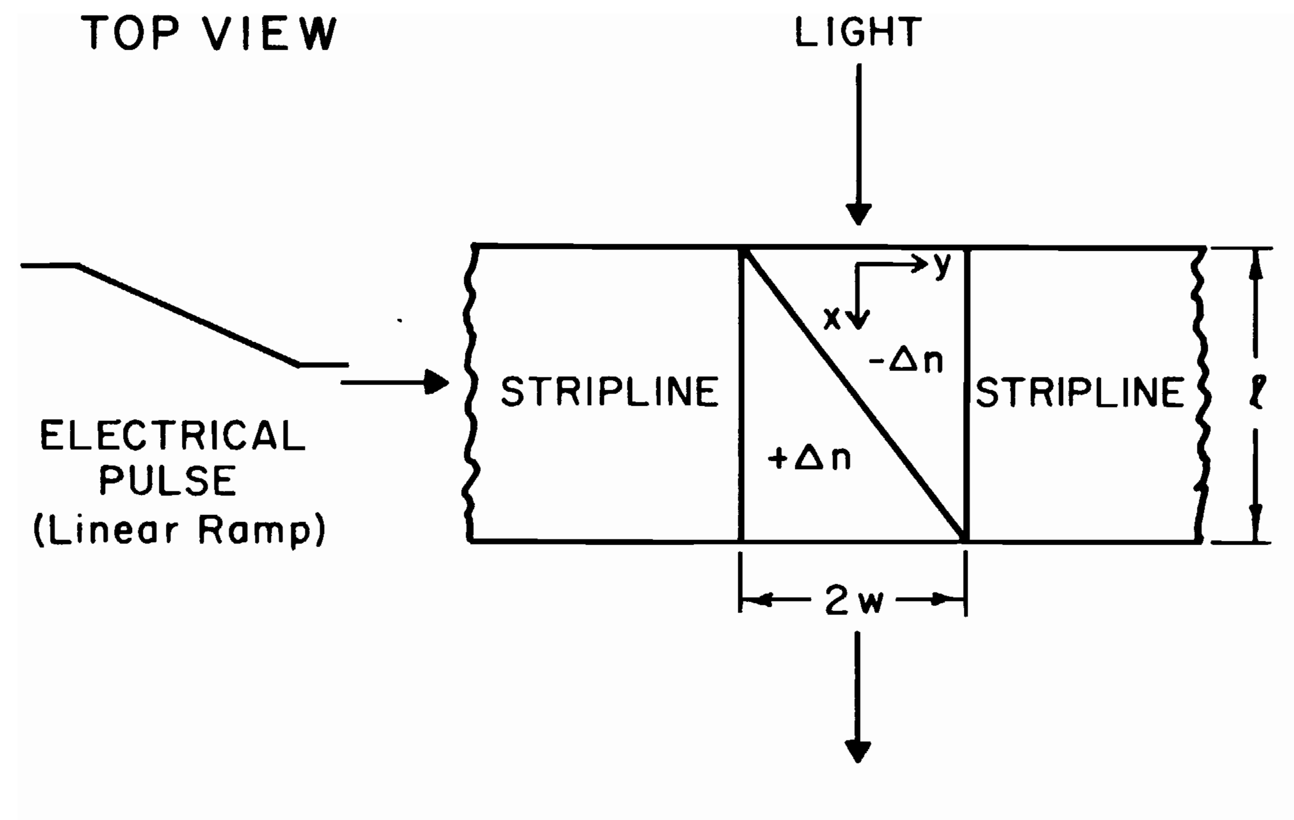

Figure 11. The two-prism deflector in a stripline configuration.

where, as with the simple prism deflector, $u = \ell(1 + u/w)/2$. On integration this yields

$$\Delta p\{y,t\} = \frac{bV_o}{Y_o nd}\left[\frac{n_o\ell^2}{4\sqrt{\varepsilon}} - \left(\ell w + \frac{n_o\ell^2}{2\sqrt{\varepsilon}}\right)\frac{y}{w} + \left(\ell w - \frac{n_o\ell^2}{4\sqrt{\varepsilon}}\right)\frac{y^2}{w^2} - \frac{\ell ytc}{w\sqrt{\varepsilon}}\right] . \qquad (3.3)$$

The first three terms represent a static delay, wedge, and cylinder lens respectively, similar to those occurring in the simple prism. The last term is a wedge varying linearly in time representing an angular deflection of

$$\theta\{t\} = bV_o\ell c/n_o wY_o d\sqrt{\varepsilon} . \qquad (3.4)$$

The maximum value of t for which the optical and electrical fields overlap is

$$t_m = t_o - (2w\sqrt{\varepsilon} + n_o\ell)/c = [(Y_o - 2w)\sqrt{\varepsilon} - n_o\ell]/c \qquad (3.5)$$

and the corresponding deflection angle is

$$\theta_m = bV_o\ell(Y_o - 2w - n_o\ell/\sqrt{\varepsilon})/n_o wY_o d . \qquad (3.6)$$

Turning now to the multiple prism arrangement shown in Figure 9, we see that the time required for the electrical pulse to move from one prism to the next is $2w\sqrt{\varepsilon}/c$ while the time required for the light is $\ell n/c$ in the stripline plus $4wn/c$ in the external prisms. Synchronization occurs when these are equal, leading to the condition

$$\ell = 2w(\sqrt{\varepsilon}/n_o - 2)\,. \tag{3.7}$$

Since the incremental deflection due to each unit is small, the total angular deflection, ϕ_m, is just $k\theta_m$ for k units, with θ_m given by Equation (3.6) and with ℓ given by Equation (3.7), thus

$$\phi_m = 2kbE_m(\sqrt{\varepsilon}/n_o - 2)(Y_o - 4w + 4wn_o/\sqrt{\varepsilon})/n_oY_o\,. \tag{3.8}$$

The total length of the optical path is $k(c/n_o)(2w\sqrt{\varepsilon}/c) = 2kw\sqrt{\varepsilon}/n_o$. Substituting this value for ℓ in Equation (2.21) along with ϕ_m of Equation (3.8) for θ_m, we obtain for the number of resolvable spots

$$N = \frac{\pi bV_o(\sqrt{\varepsilon}/n_o - 2)kw}{\lambda Y_o d}(Y_o - 4w + 4wn_o/\sqrt{\varepsilon}) \cdot \left[1 - \frac{bV_o\sqrt{\varepsilon}(\sqrt{\varepsilon}/n_o - 2)k^2}{2n_o^2Y_od}(Y_o - 4w + 4wn_o/\sqrt{\varepsilon})\right] \tag{3.9}$$

and a time resolution of

$$\tau = t_m/N = \sqrt{\varepsilon}(Y_o - 4w + 4wn_o/\sqrt{\varepsilon})/cN\,. \tag{3.10}$$

Equations (3.9) and (3.10) describe the important characteristics of the multiple prism system. In streak camera applications it is desirable to obtain the maximum number of spots possible given a particular voltage risetime, and two limiting cases are of special interest: those where the number of prisms, k, is small (as may be required for economic reasons); and those where the number of prisms

has its optimum value. For small k the term in brackets is approximately one and Equations (3.9) and (3.10) simplify to

$$N = \pi b V_o (\sqrt{\varepsilon}/n_o - 2) k w (Y_o - 4w + 4wn/\sqrt{\varepsilon})/\lambda Y_o d$$

$$\tau = \lambda Y_o d\sqrt{\varepsilon}/\pi b V_o (\sqrt{\varepsilon}/n_o - 2) kwc. \qquad (3.11)$$

Maximizing the number of resolvable spots, N, with respect to the prism halfwidth, w, leads to

$$w = Y_o/8(1 - n_o/\sqrt{\varepsilon})$$

$$\ell = Y_o(\sqrt{\varepsilon}/n_o - 2)/4(1 - n_o/\sqrt{\varepsilon})$$

$$N = \pi b V_o k Y_o (\sqrt{\varepsilon}/n_o - 2)/16\lambda d(1 - n_o/\sqrt{\varepsilon})$$

$$\tau = 8\lambda d(\sqrt{\varepsilon} - n_o)/\pi b V_o kc(\sqrt{\varepsilon}/n_o - 2). \qquad (3.12)$$

For lithium niobate at one micrometer and a field of 10^7 V/m ($\varepsilon = 26.4$, $n_o = 2.2$, $b = 1.6 \times 10^{-10}$ m/V), these give:

$$\tau = (50/k) \text{ picoseconds; } N = 10\, kt_o \text{ spots; } w = 1.28\, t_o \text{ cm;}$$
$$\text{and } \ell = 0.856\, t_o \text{ cm.} \qquad (3.13)$$

with t_o in nanoseconds.

These equations show that the number of resolvable spots is proportional to the number of prism sections as we would expect. In addition, the prism dimensions scale with the voltage ramp time (through Y_o) as does the number of resolvable spots, while the

resolvable time is independent of the physical dimensions of the prisms. Thus a physically larger system (more interaction length) provides more spots but no better resolution for a fixed number of prisms.

For large k, N is a maximum when

$$k = k_o = \{[3bV_o\sqrt{\varepsilon}(\sqrt{\varepsilon} - 2n_o)(Y_o - 4w + 4wn_o/\sqrt{\varepsilon})]/2n_o^3Y_od\}^{-\frac{1}{2}} \qquad (3.14)$$

which yields

$$N\{k_o\} = \frac{2\pi w}{3\lambda}\left[\frac{2n_obV_o(\sqrt{\varepsilon} - 2n_o)(Y_o - 4w + 4wn_o/\sqrt{\varepsilon})}{3Y_od\sqrt{\varepsilon}}\right]^{\frac{1}{2}}$$

$$\tau\{k_o\} = \frac{3\lambda\sqrt{\varepsilon}}{2\pi wc}\left[\frac{3Y_od\sqrt{\varepsilon}(Y_o - 4w + 4wn_o/\sqrt{\varepsilon})}{2n_obV_o(\sqrt{\varepsilon} - 2n_o)}\right]^{\frac{1}{2}}. \qquad (3.15)$$

Finally, maximizing this N with respect to w yields

$$w = Y_o/6(1 - n_o/\sqrt{\varepsilon})$$

$$\ell = Y_o(\sqrt{\varepsilon}/n_o - 2)/3(1 - n_o/\sqrt{\varepsilon})$$

$$k_o = [2n_o^3d/bV_o(\varepsilon - 2n_o\sqrt{\varepsilon})]^{\frac{1}{2}}$$

$$N = \frac{\pi Y_o[2n_obV_o(1 - 2n_o/\sqrt{\varepsilon})]^{\frac{1}{2}}}{27\lambda(1 - n_o/\sqrt{\varepsilon})\sqrt{d}}$$

$$\tau = 9\lambda(\sqrt{\varepsilon} - n_o)/\pi c[2n_obV_o(1 - 2n_o/\sqrt{\varepsilon})/d]^{\frac{1}{2}}. \qquad (3.16)$$

For lithium niobate under the same conditions as before

$$\tau = 0.88 \text{ picoseconds; } n = 378\ t_o \text{ spots; } k = 59;$$

$$w = 1.70\ t_o \text{ cm and } \ell = 1.14\ t_o \text{ cm} \qquad (3.17)$$

where t_o is in nanoseconds.

These results show that an optimum number of prism sections exists for a given material and peak voltage, and use of this many prisms results in a corresponding characteristic resolving time. As before, the number of spots and system dimensions scale linearly with the voltage ramp time.

3.2 Lens Systems--Geometric Considerations

Analysis of the multiple lens system is most easily accomplished by the use of ray matrix techniques. The analysis presented here begins with a determination of the geometric constraints and their consequences. The results will be applied to the multiple lens system and finally to the special case of a single lens system having synchronous light and electrical pulse interaction.

The geometric limitations may be understood with the aid of Figure 11. With perfect synchronism of the light and voltage pulses, the deflection system is entirely equivalent to that of Figure 11. This diagram shows the situation when the beam width, 2w, is less than the effective voltage pulse width, $2Y_1$, in the crystal. This condition is required for complete overlap of the optical pulse width

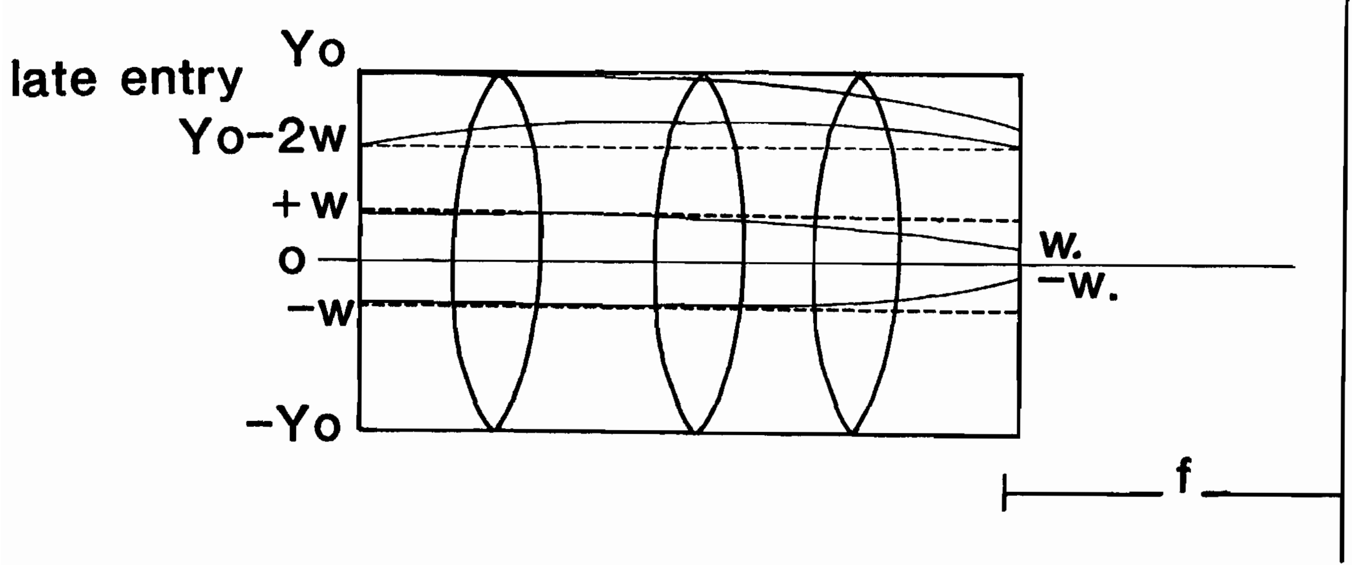

Figure 12. Traveling lens geometric limitations.
For a beam width much less than the electrical pulse width, $2Y_o$, in the deflector, a beam of width 2w' must stay in a region of that width as shown at the top (latest possible entry time, full deflection) while traveling through the deflection system.

by the electrically induced refractive index change in the crystal in order to avoid severe beam quality degradation. The entry time of the light pulse into the deflector relative to the position of the voltage pulse corresponds to the height of the ray as shown in the figure. Two beam entry times are depicted. The first shows the beam of width 2w entering the system with the beam edges at heights Y_1 and $Y_1 - 2w$ corresponding to the edge of the electrical pulse and therefore maximum deflection. The second shows the beam edges at $\pm w$ corresponding to the center of the electrical pulse and no deflection. Note the dashed lines beginning at the beam edges upon entry. These form an aperture within which the beam must stay during its passage through the system. This aperture constraint is imposed by the requirements that the beam must pass through the deflector without slipping beyond the edge of the electrical pulse, and it must pass through the deflector without hitting the mirrors upon entry or exit from the deflector. This constraint determines an optimum f-number for the entering beam and limits the number of resolvable spots.

The optical system may be represented by a ray matrix of the form[41]

$$T = \begin{pmatrix} A & B \\ C & D \end{pmatrix} \qquad (3.18)$$

which has a determinant of 1, i.e., AD - BC = 1. For all cases of interest here the additional constraint of A = D occurs. Thus

$$A^2 = BC + 1 \,. \qquad (3.19)$$

The ray matrix may be used to determine the height, h', and slope, s', of any ray exiting the system as a function of its entry height, h, and slope, s, according to

$$\begin{pmatrix} A & B \\ C & D \end{pmatrix}\begin{pmatrix} h \\ s \end{pmatrix} = \begin{pmatrix} h' \\ s' \end{pmatrix} = T\begin{pmatrix} h \\ s \end{pmatrix} . \tag{3.20}$$

From Figure 12 the lower ray of the beam at maximum deflection must satisfy

$$T\begin{pmatrix} Y_1 - 2w \\ s \end{pmatrix} = \begin{pmatrix} Y_1 - 2w \\ s' \end{pmatrix} . \tag{3.21}$$

A beam of f-number f_1 inside the crystal requires $s = 1/2f_1$. Inserting this gives

$$\begin{pmatrix} A & B \\ C & D \end{pmatrix}\begin{pmatrix} Y_1 - 2w \\ 1/2f_1 \end{pmatrix} = \begin{pmatrix} AY_1 - 2Aw + B/2f_1 \\ CY_1 - 2Cw + D/2f_1 \end{pmatrix} = \begin{pmatrix} Y_1 - 2w \\ s' \end{pmatrix} . \tag{3.22}$$

Equating the heights then leads to

$$f_1 = \frac{B}{2(1 - A)(Y_1 - 2w)} = \frac{-(1 + A)}{2C(Y_1 - 2w)} . \tag{3.23}$$

For a given system this determines the external focusing required in order to obtain the maximum number of spots.

For the lower ray of the undeflected beam, the effects of the system are given by

$$\begin{pmatrix} A & B \\ C & D \end{pmatrix}\begin{pmatrix} -w \\ 1/2f_1 \end{pmatrix} = \begin{pmatrix} -w_1 \\ s_1 \end{pmatrix} = \begin{pmatrix} -Aw + B/2f_1 \\ -Cw + D/2f_1 \end{pmatrix} . \tag{3.24}$$

At the exit plane the spot radius is then

$$w_1 = Aw - B/2f_1 = Aw - (1 - A)(Y_1 - 2w) \tag{3.25}$$

and the distance to the focal plane is

$$f = \frac{w_1}{s_1} = \frac{Aw - (1 - A)(Y_1 - 2w)}{D(1 - A)(Y_1 - 2w)/B - Cw} \tag{3.26}$$

while the spot size in the focal plane is

$$2w_o = \beta f = \frac{2\lambda f}{\pi w_1} = \frac{2\lambda}{f}\left[D(1 - A)(Y - 2w)/B - Cw\right]^{-1}. \tag{3.27}$$

To determine the deflection in the focal plane, one may first compute the displacement of the center of the beam at the exit face relative to the entry face and then add to this the additional deflection resulting from the non-zero slope of the central ray between the exit face and the focal plane. The position of the central ray at the exit face follows from the position at the entry face by application of the system ray matrix

$$\begin{pmatrix} A & B \\ C & D \end{pmatrix}\begin{pmatrix} Y_1 - w \\ 0 \end{pmatrix} = \begin{pmatrix} AY_1 - Aw \\ CY_1 - Cw \end{pmatrix} \tag{3.28}$$

where $Y_1 - w$ is the entry face height, $A(Y_1 - w)$ the exit face height, and $C(Y_1 - w)$ the slope of the exiting central ray. The spot movement of the beam on the output face is then

$$D_1 = (Y_1 - w) - A(Y_1 - w) = (1 - A)(Y_1 - w) \tag{3.29}$$

and the movement at the focal plane due to the slope change is

$$D_2 = -f[C(Y_1 - w)] = C(w - Y_1)\left[\frac{Aw - (1 - A)(Y_1 - 2w)}{D(1 - A)(Y_1 - 2w)/B - Cw}\right]. \quad (3.30)$$

From the total two sided deflection in the focal plane, $2(D_1 + D_2)$, and the spot size in the focal plane, $2w_o$, the number of resolvable spots for this system is $N = 2(D_1 + D_2)/2w_o$. Using (3.29), (3.30), (3.27), and (3.19), the number of resolvable spots and corresponding resolvable time are

$$N = -\pi C(Y_1 - w)[A(Y_1 - w) - (Y_1 - 3w)]/\lambda(1 + A)$$

$$\tau = 2(Y_1 - w)/N(C/\sqrt{\varepsilon}) = \frac{-2\lambda(1 + A)\sqrt{\varepsilon}}{\pi c C[A(Y_1 - w) - (Y_1 - 3w)]}. \quad (3.31)$$

These simplify to the simple lens formulae, (2.32) and (2.34), when the appropriate matrix elements, $A = 1$ and $C = 1/f$ with f given by (2.30), are used and the transit time, $(n\ell/c)$, is ignored. Equation (3.31) for the number of resolvable spots corresponds to Equation (2.21) for prism systems when geometric constraints on the maximum allowable deflection are taken into account.

The preceding derivations have assumed that the optical system is made up of a sequence of positive lenses; however, the system will also provide deflection when negative lenses are employed. Practically, a simple reversal of the electrical field will reverse the sign of the lens. The negative lens case is treated in Appendix 2, where

it is shown to be inferior to the positive lens case. For this reason it shall be given no further consideration here.

3.3 Multiple Lens System

The appropriate ray matrix for the multiple lens system can be developed from the simple elements shown in Table 2.[42] For light passage through an inactive medium of length a/2 and index n_o, followed by a weakly quadratic active medium of index $n = n_o - \frac{1}{2}n_2 r^2$, followed by another inactive section identical to the first, the appropriate matrix is

$$T' = SL_2S = \begin{pmatrix} 1 - \dfrac{a+h}{2f_1 n_o} & \dfrac{a+h}{n_o} - \dfrac{2ah + a^2}{4n_o^2 f_1} \\ -\dfrac{1}{f_1} & 1 - \dfrac{a+h}{2f_1 n_o} \end{pmatrix} \tag{3.32}$$

where f = 1/hn . The ray matrix for q consecutive passes is just the qth power of T'

$$T^q = (T')^q . \tag{3.33}$$

Defining ψ by the equation $\cos\psi = 1 - (a + h)/2f_1 n_o$, Sylvester's theorem[42] may be used to show that

$$T^q = \begin{pmatrix} \cos q\psi & \left(\dfrac{a+h}{n_o} - \dfrac{2ah + a^2}{4n_o^2 f_1}\right) \dfrac{\sin q\psi}{\sin\psi} \\ \dfrac{-\sin q\psi}{f_1 \sin\psi} & \cos q\psi \end{pmatrix} = \begin{pmatrix} A & B \\ C & D \end{pmatrix} . \tag{3.34}$$

For the configuration described here, $n_2 = 2bV_o/Y_1^2 d$ and $\psi \ll 1$ which lead to

TABLE 2

RAY MATRICES

Element	Ray matrix
n = 1 | n | n = 1; $\leftarrow a/2 \rightarrow$	$S = \begin{vmatrix} 1 & a/2n \\ 0 & 1 \end{vmatrix}$ transit through medium of index n
$\leftarrow h \rightarrow$; n = 1 | | n = 1; $n = n_o - \frac{1}{2} n_2 r^2$	$L_1 = \begin{vmatrix} \cos\left(h\sqrt{\frac{n_2}{n_o}}\right) & \frac{1}{\sqrt{n_o n_2}} \sin\left(h\sqrt{\frac{n_2}{n_o}}\right) \\ -\sqrt{n_o n_2} \sin\left(h\sqrt{\frac{n_2}{n_o}}\right) & \cos\left(h\sqrt{\frac{n_2}{n_o}}\right) \end{vmatrix}$
Same as above	$L_2 = \begin{vmatrix} 1 - \frac{h^2 n_2}{2n_o} & h/n_o \\ - n_2 h & 1 - \frac{h^2 n_2}{2n_o} \end{vmatrix}$ for $h \sqrt{\frac{n}{n_o}} << 1$

$$A = \cos q\psi$$

$$f_1 = Y_1^2 d/2bV_o h$$

$$\sin\psi \approx \Psi = \left[\frac{(a+h)2bV_o h}{n_o d Y_1^2}\right]^{\frac{1}{2}}$$

$$C = \frac{-\sin q\psi}{f_1 \sin\psi} = \frac{-\sin q\psi}{Y_1}\left[\frac{2bV_o h n_o}{(a+h)d}\right]^{\frac{1}{2}} \qquad (3.35)$$

along with

$$h = \ell/\cos\theta_1 = \ell/(1 - n_o^2/\varepsilon)^{\frac{1}{2}}$$

$$a = s/\cos\theta_1 = s/(1 - n_o^2/\varepsilon)^{\frac{1}{2}}$$

$$w' = (\ell + s)\tan\theta_1 = (\ell + s)n_o/(\varepsilon - n_o^2)^{\frac{1}{2}} \qquad (3.36)$$

in terms of the notation of Figure 10. Substitution of Equations (3.35) and (3.36) in Equation (3.31) then yields performance specifications for the multiple lens system:

$$N = \frac{\pi n_o \sin q\psi}{Y_1\lambda(1 + \cos q\psi)}\left(\frac{2bV_o\ell}{w'd\sqrt{\varepsilon - n_o^2}}\right)^{\frac{1}{2}} (Y_1-w')[(Y_1-w')\cos q\psi - (Y_1-3w')]$$

$$\tau = \frac{2Y_1\lambda\sqrt{\varepsilon}(1 + \cos q\psi)}{\pi n_o c \sin q\psi}\left(\frac{w'd\sqrt{\varepsilon - n_o^2}}{2bV_o\ell}\right)^{\frac{1}{2}} [(Y_1-w')\cos q\psi - (Y_1-3w')]^{-1}$$

$$\psi = \frac{1}{n_o Y_1}\left(\frac{2bV_o\ell w'\varepsilon}{d\sqrt{\varepsilon - n_o^2}}\right)^{\frac{1}{2}} . \qquad (3.37)$$

As with the multiple prism system several limiting cases are of special interest: one for the less than optimum system (but perhaps required for economic reasons) involving a small number of passes, i.e., small q; one involving an optimum number of passes, i.e., optimum q; and one where the beam width, 2w', is much less than the electrical pulse length, $2Y_1$, as in the experiments to be described in a later chapter. For small q and $A \approx 1$ and $C = -1/f_1$, these become

$$N = \frac{2\pi b V_o \ell w' q (Y_1 - w')}{Y_1^2 d\lambda \sqrt{1 - n_o^2/\varepsilon}}$$

$$\tau = \frac{Y_1^2 d\lambda \sqrt{\varepsilon - n_o^2}}{\pi b V_o \ell w' c q} \quad . \tag{3.38}$$

Inserting $\ell + s = w'/\tan\theta_1$ and Equations (3.36), and then optimizing the number of resolvable spots, N, with respect to the beam radius, w', we obtain $Y_1 = [w'^2 + 2w'(w' - s\tan\theta_1)]/(2w' - s\tan\theta_1)$. For the range of $0 < s < w'/\tan\theta_1$ this yields $3w'/2 \geq Y_1 \geq w'$, but Equation (3.23) for the external focusing indicates that when $Y_1 > 2w'$, a diverging beam should be used (since $A > 1$ and $C < 1$ and therefore $f_1 < 0$. However, the beam will then extend outside the allowed aperture; therefore the optimum condition is unusable. The largest possible value of w' consistent with the above arguments is $Y_1 = 2w'$ which when used in Equations (3.38) yields

$$N = \pi b V_o \ell q / 2 d\lambda \sqrt{1 - n_o^2/\epsilon}$$

$$\tau = 2 Y_1 d\lambda \sqrt{\epsilon - n_o^2} / \pi b V_o \ell c q$$

$$w' = Y_1/2$$

$$(\ell + s) = Y_1 \sqrt{\epsilon - n_o^2} / 2 n_o \qquad (3.39)$$

for the performance and dimensional specifications (Figure 10). For comparison with Equations (3.12) for the multiple prism deflector and the example given there, note that the best results are obtained when the optical path is contained entirely in the active medium. Then, for $s = 0$, Equations (3.39) for the multiple lens system become

$$N = \pi b V_o Y_1 q \sqrt{\epsilon} / 4 d\lambda n_o$$

$$\tau = 4 n_o d\lambda / \pi b V_o c q$$

$$w' = Y_1/2$$

$$\ell = Y_1 \sqrt{\epsilon - n_o^2} / 2 n_o \; . \qquad (3.40)$$

With one micrometer wavelength light and a field of 10^7 V/m as before, lithium niobate in this configuration will provide a resolving time, τ, and number of resolvable spots, N, for a beam of halfwidth w' and crystal width ℓ, of:

$\tau = 5.84/q$ picoseconds; $N = 171\ q t_o$ spots; $w' = 2.92\ t_o$ cm; and $\ell = 6.16\ t_o$ cm
where t_o is in nanoseconds. (3.41)

These equations, as compared to Equations (3.13), show that for a given pulse risetime the lens system may be optimized to provide performance far superior to that of the prism system by allowing the use of considerably more active material per pass.

For large q the number of resolvable spots as given by Equation (3.37) is a maximum when

$$\cos q\psi = \left[\frac{9Y_1 - 17w'}{4(Y_1 - w')}\right]^{\frac{1}{2}} - \tfrac{1}{2}\ . \tag{3.42}$$

Optimization of N with respect to w' when Equation (3.42) is inserted in Equation (3.37) proves difficult. The equation dN/dw' = 0 cannot be solved analytically. However, the aperture requirements preclude the use of entering beams with negative f-numbers, and from Equation (3.23) this means Y_1 must be greater than or equal to the beam width 2w'. If dN/dw' is evaluated for $w' = Y_1/2$, the resulting slope is greater than zero, suggesting that this condition may specify the optimum value for w'. Using this condition gives

$$w' = Y_1/2$$

$$\cos q\psi = 0$$

$$\sin q\psi = 1$$

$$N = \frac{\pi n_o}{\lambda}\left(\frac{2bV_o\ell Y_1}{d\sqrt{\varepsilon - n_o^2}}\right)^{\frac{1}{2}}$$

$$\tau = \frac{\lambda\sqrt{\varepsilon}}{\pi n_o c}\left(\frac{Y_1 d\sqrt{\varepsilon - n_o^2}}{2bV_o\ell}\right)^{\frac{1}{2}}$$

$$q = \frac{\pi}{2\psi} = \frac{\pi n_o}{2}\left(\frac{dY_1\sqrt{\varepsilon - n_o^2}}{bV_o\ell\varepsilon}\right)^{\frac{1}{2}}\ . \tag{3.43}$$

Clearly, when ℓ is as large as possible N will be a maximum. From the synchronism equation, $w' = (\ell + s)n_o/\sqrt{\varepsilon - n_o^2} = Y_1/2$, this occurs when $s = 0$. Then

$$w' = Y /2$$

$$\ell = Y_1\sqrt{\varepsilon - n_o^2}/2n_o$$

$$N = \frac{\pi Y_1}{\lambda}\left(\frac{bV_o n}{d}\right)^{\frac{1}{2}}$$

$$\tau = \frac{\lambda}{\pi c}\left(\frac{d\varepsilon}{bV_o n_o}\right)^{\frac{1}{2}}$$

$$q = \frac{\pi n_o}{2}\left(\frac{2n_o d}{bV_o \varepsilon}\right)^{\frac{1}{2}} . \tag{3.44}$$

For lithium niobate these specify:

$\tau = 0.092$ picoseconds; $N = 10882\ t_o$ spots; $q = 35$;

$\ell = 6.16\ t_o$ cm ; and $w' = 2.92\ t_o$ cm

where t_o is in nanoseconds. (3.45)

The superiority of the multiple lens system is again apparent when these results are compared to those for the multiple prism system as given in Equations (3.17).

The last case to be analyzed here occurs for $w' \ll Y_1$. Then from Equation (3.42)

$$\cos q\psi = \left[\frac{9Y_1 - 17w'}{4(Y_1 - w')}\right]^{\frac{1}{2}} - \tfrac{1}{2} \approx 1 - \frac{2w'}{3Y_1}$$

$$\sin q\psi \approx \left(\frac{4w'}{3Y_1}\right)^{\frac{1}{2}} \qquad (3.46)$$

and from Equations (3.37) and (3.42)

$$N = \frac{(2.18w'/Y_1)\pi n_o}{2\lambda}\left(\frac{bV_o \ell Y_1}{d\sqrt{\varepsilon - n_o^2}}\right)^{\frac{1}{2}}$$

$$\tau = \frac{2\lambda\sqrt{\varepsilon}}{(2.18w'/Y_1)\pi n_o c}\left(\frac{Y_1 d\sqrt{\varepsilon - n_o^2}}{bV_o \ell}\right)^{\frac{1}{2}}$$

$$q = \frac{1}{\psi}\left(\frac{4w'}{Y_1}\right)^{\frac{1}{2}} = 2n_o\left(\frac{dw'\sqrt{\varepsilon - n_o^2}}{bV_o \ell \varepsilon}\right)^{\frac{1}{2}} \qquad (3.47)$$

and finally for s = 0, i.e., no inactive medium in the optical path, these become

$$N = \left(\frac{2.18}{2\sqrt{2}}\right)\left(\frac{w'}{Y_1}\right)\left(\frac{\pi Y_1}{\lambda}\right)\left(\frac{bV_o n_o}{d}\right)^{\frac{1}{2}}$$

$$\tau = \left(\frac{2\sqrt{2}}{2.18}\right)\left(\frac{Y_1}{w'}\right)\left(\frac{\lambda}{\pi c}\right)\left(\frac{d\varepsilon}{bV_o n_o}\right)^{\frac{1}{2}}$$

$$q = \frac{\pi n_o}{2}\left[\left(\frac{2n_o d}{bV_o \varepsilon}\right)\left(\frac{16w'}{\pi^2 Y_1}\right)\right]^{\frac{1}{2}} \qquad (3.48)$$

Thus the number of resolvable spots and resolving time are degenerated from the $2w' = Y_1$ optimum, given by Equations (3.43), by the factor $(0.77w'/Y_1)$, and q is smaller by the factor $(16w'/\pi^2 Y_1)^{\frac{1}{2}}$.

3.4 Single Lens

For a single lens system with the angle between the propagation directions of the light and electrical pulse adjusted to maintain perfect synchronization, the system may be described by matrix L1 of Table 2 with $n_2 = 2bV_o/dY_1$ and $h = \ell\sqrt{1 - n_o^2/\varepsilon}$. Thus

$$A = \cos\left[\frac{\ell}{Y_1}\left(\frac{2bV_o}{n_o d\sqrt{1 - n_o^2/\varepsilon}}\right)^{\frac{1}{2}}\right]$$

$$C = -\left(\frac{2bV_o n_o}{Y_1^2 d}\right)^{\frac{1}{2}} \sin\left[\frac{\ell}{Y_1}\left(\frac{2bV_o}{n_o d\sqrt{1 - n_o^2/\varepsilon}}\right)^{\frac{1}{2}}\right]. \tag{3.49}$$

These may be substituted in Equations (3.31) to obtain N and τ. Since A and C are independent of the beam halfwidth, w, Equation (3.31) may be maximized with respect to w giving

$$w = \left(\frac{2 - A}{3 - A}\right) Y_1 . \tag{3.50}$$

As with the multiple lens system the aperture constraints require the f-number of the entering beam to be positive and hence $Y_1 \geq 2w'$. For $Y_1 = 2w$

$$N = -\pi C Y_1^2/4\lambda$$

$$\tau = -4\lambda\sqrt{\varepsilon}/\pi c C Y_1 \tag{3.51}$$

using C as given by Equation (3.49). Finally, the number of resolvable spots is a maximum when C is a maximum. This requires the sine function to be equal to 1, or

$$\frac{\ell}{Y}\left(\frac{2bV_o}{n_o d\sqrt{1 - n_o^2/\varepsilon}}\right)^{\frac{1}{2}} = \pi/2 \tag{3.52}$$

which determines ℓ, the interaction length, as a function of the pulse risetime. Then

$$C = -\left(\frac{2bV_o n_o}{Y_1{}^2 d}\right)^{\frac{1}{2}}$$

$$N = \frac{\pi Y_1}{\lambda}\left(\frac{bV_o n_o}{d}\right)^{\frac{1}{2}}$$

$$\tau = \frac{\lambda}{\pi c}\left(\frac{d\,\varepsilon}{bV_o n_o}\right)^{\frac{1}{2}} \tag{3.53}$$

give the value for C, the number of resolvable spots, and the resolvable time. These values for C, N, and τ are identical to those found for the multipass case as given by Equations (3.44). This is no surprise since both configurations have the same w and both represent continuous interaction of the light and voltage pulses. One simply has mirrors which rearrange the geometry of the system and provide the practical advantage of a higher stripline impedance.

3.5 Comparisons of the Multiple Unit Systems

Based upon the examples given for the multiple unit systems it would appear that the lens system is superior, and indeed in some ways it is. The possibility of having continuous interaction between the optical and electrical pulses connot be realized in the prism system, whereas it can be in the lens system. This leads to the superiority of the lens system in the idealized cases analyzed to this point. To obtain a better understanding of the relative advantages of each, we will now consider their effectiveness per unit length of optical and electrical pulse interaction.

To begin, let the number of passes in each device be a small number. For the prisms Equations (3.12) give

$$N_p/\ell k = \pi b V_o / 4\lambda d$$

$$\tau_p = \frac{8\lambda n_o d}{\pi b V_o kc} \left(\frac{1 - n_o/\sqrt{\varepsilon}}{1 - 2n_o/\sqrt{\varepsilon}} \right) \tag{3.54}$$

while for the lens system, Equations (3.40) give

$$N_\ell/\ell q = \pi b V_o / 2\lambda d\sqrt{1 - n_o^2/\varepsilon}$$

$$\tau_q = \frac{4\lambda n_o d}{\pi b V_o cq} \; . \tag{3.55}$$

Then
$$\frac{N_\ell/\ell q}{N_p/\ell k} = \frac{2}{\sqrt{1 - n_o^2/\varepsilon}}$$

$$\frac{\tau_\ell}{\tau_p} = \frac{(1 - 2n_o/\sqrt{\varepsilon})}{2(1 - n_o/\sqrt{\varepsilon})}\left(\frac{k}{q}\right). \tag{3.56}$$

The lens system is about twice as effective. Comparison of the multiple prism formulae, Equations (3.54), to the single prism formulae, Equations (2.23) and (2.24), shows that the synchronism condition imposed upon the multiple prism system requires a value of w such that N is cut in half, whereas this is not the case for the lens systems. The $\sqrt{1 - n_o^2/\varepsilon}$ factor is due to the increased interaction length presented by the lens material due to the non-normal light incidence. These differences result in the resolving times differing by approximately a factor of 2 also.

In order to compare the volume of active material required to produce the same performance, note first that the interaction length needed for the prism systems is twice that needed for the lens systems. From Equations (3.12) the required stripline length per pass is $Y_o/4(1 - n_o/\sqrt{\varepsilon})$ and the number of passes required is $\ell/[Y_o(\sqrt{\varepsilon}/n_o - 2)/4(1 - n_o/\sqrt{\varepsilon})]$ giving a required width of $\ell/(\sqrt{\varepsilon}/n_o-2)$ for the prism system, while for the lens system Equations (3.40) require a width of $w' = Y_1/2$ and $\ell/(Y_1\sqrt{\varepsilon - n_o^2}/2n)$ passes to make a total width of $n\ell/\sqrt{\varepsilon - n_o^2}$. Inclusion of the $2/\sqrt{1 - n_o^2/\varepsilon}$ factor shows that

$$V_p = \left(\frac{2}{\sqrt{1 - n_o^2/\varepsilon}}\right)(\ell)\ (d)\left[\frac{n_o \ell}{\sqrt{\varepsilon}(1 - 2n_o/\sqrt{\varepsilon})}\right]$$

$$V_\ell = (\ell)\ (d)\left[\frac{n_o \ell}{\sqrt{\varepsilon}\sqrt{1 - n_o^2/\varepsilon}}\right] \qquad (3.57)$$

for the volume of the prism and lens systems respectively. Thus

$$\frac{V_p}{V_\ell} = \frac{2}{(1 - 2n_o/\sqrt{\varepsilon})} \,. \qquad (3.58)$$

The lens system exhibits a volume advantage for a small number of passes.

In larger systems the advantages of the lens system continue to grow. For the optimum systems with the number of passes and widths optimized, Equations (3.16) for the prism system and Equations (3.44) for the lens system show that

$$N_\ell/N_p = 27(1 - n_o/\sqrt{\varepsilon})/[2(1 - 2n_o/\sqrt{\varepsilon})]^{\frac{1}{2}}$$

$$\tau_p/\tau_\ell = 9(1 - n_o/\sqrt{\varepsilon})/[2(1 - 2n_o/\sqrt{\varepsilon})]^{\frac{1}{2}}$$

$$\frac{V_\ell}{V_p} = \frac{(\ell)(w)(d)(q)}{(\ell)(2w)(d)(k)} = \frac{9\pi(1 - n_o/\sqrt{\varepsilon})^2}{8}\left[\frac{(1 - n_o^2/\varepsilon)}{(1 - 2n_o/\sqrt{\varepsilon})}\right] \qquad (3.59)$$

where ℓ_ℓ and ℓ_p are the total interaction lengths. (The ℓ's in the numerators and denominators are not the same but refer to their respective systems.) For lithium niobate these become:

$$N_\ell/N_p = 28.8; \; \tau_p/\tau_\ell = 9.6; \; V_\ell/V_p = 2.76; \text{ and } \ell_\ell/\ell_p = 3.21. \tag{3.60}$$

Thus the lens system enables use of more material to generate a longer total interaction length to produce more spots and a better resolving time.

3.6 Voltage Pulse Generator Limitations

The foregoing sections have all assumed that a voltage pulse of the desired peak voltage and risetime can be produced; usually, however, this is not the case. The major difficulty in developing electrooptic deflection devices stems from the lack of adequate pulse generators. This places another constraint on these systems leading to different optimizations. This section will assume a voltage pulse generator model and then determine its effects upon system optimization and performance.

Most pulse generation techniques exhibit effects describable by a characteristic inductance. This suggests a very reasonable model: the voltage pulse source is equivalent to an effective internal inductance, L, characteristic of the switching mechanism and particular device, connected in series with a resistance, z_o, representing the transmission line impedance. For an ideal step function voltage generator the model predicts a pulse into the transmission line with a risetime proportional to L/z_o. This model is particularly suited

to the stripline deflectors where z_o varies for different configurations. If the pulse generator functions within a line whose impedance is matched to the stripline, the risetime depends upon z_o. If the pulse generator operates in a line of impedance z_o which is coupled by some technique to the deflector line, the voltage depends upon the transmission coefficient of the matching section.

For striplines, the approximate impedance is given by Equations (2.37) and (2.38), the latter equation being sufficiently accurate for most cases of interest here ($d < \ell$). Thus

$$t_o = L/z_o \approx \sqrt{\varepsilon}\ \ell L/120\pi d$$

$$Y = ct_o/\sqrt{\varepsilon} = c\ell L/120\pi d \tag{3.61}$$

for pulse generators operating in a matched transmission line. For the multiple prism system, employing the synchronism condition, $\ell = 2w(\sqrt{\varepsilon}\ /n_o - 2)$, gives

$$Y_o = cLw(\sqrt{\varepsilon}/n_o - 2)/60\pi d \tag{3.62}$$

which may be inserted directly into Equations (3.11) for small k to yield

$$N_p = 60\pi^2 bV_o kw\,[cL(\sqrt{\varepsilon}/n_o - 2)/60\pi d - 4(1 - n_o/\sqrt{\varepsilon})]/\lambda cL$$

$$\tau_p = \lambda\sqrt{\varepsilon}L/60\pi^2 bV_o k$$

$$d = V/E$$

$$\ell = 2w(\sqrt{\varepsilon}/n_o - 2) \tag{3.63}$$

for the number of resolvable spots, resolving time, stripline thickness, and stripline width. For lithium niobate with $V = 10^7$ V/m and L = 15 nh (see Chapter 4) the following numerical values ensue:

$N_p = 12$ kw spots; $\tau_p = 81/k$ picoseconds; d = 1 mm;

and $t_o = 1.37$ w nanoseconds; where w is in cm. (3.64)

For the lens system the halfwidth of the pulse in the transmission line is

$$Y_1 = c\ell L/120\pi d \,. \qquad (3.65)$$

Then

$$N_\ell = \pi b V_o \ell q / 2d\lambda\sqrt{1 - n_o^2/\varepsilon}$$

$$\tau_\ell = L\lambda\sqrt{\varepsilon - n_o^2}\,/60\pi^2 b V_o q$$

$$w' = Y_1/2 \qquad (3.66)$$

on insertion of relation (3.65) into Equations (3.39). Again, for lithium niobate:

$N_\ell = 27.8\ q\ell$; $\tau_\ell = 73.5/q$ picoseconds; $w' = 5.97\ \ell$ cm;

and $t_o = 2.04\ \ell$ nanoseconds; where ℓ is in cm. (3.67)

The comparison per unit length of interaction yields

$$\frac{N_\ell/\ell q}{N_p/\ell k} = \frac{cL\sqrt{\varepsilon/n_o - 2}}{\sqrt{1 - n_o^2/\varepsilon}\ 60\pi\,[cL(\sqrt{\varepsilon}/n_o - 2)/60\pi - 4d(1 - n_o/\sqrt{\varepsilon})]} \,. \qquad (3.68)$$

For small d (the usual case) the comparison becomes

$$\frac{N_\ell/\ell q}{N_p/\ell k} = \frac{1}{\sqrt{1 - n_o{}^2/\varepsilon}}. \tag{3.69}$$

These are essentially equivalent (within a factor of cos θ_1). For large d the lens system begins to gain due to the transit time effects in the prism system.

Since the performance is essentially the same per unit length of active material, the volume comparison becomes a width comparison. For the prisms the stripline length per pass (of width ℓ) is $2w = \ell/(\sqrt{\varepsilon}/n_o - 2)$, and for the lens system it is $w' = c\ell L/240\pi d$. Generally, the length per pass for the lens system will be somewhat larger. For the lithium niobate examples, 2w = 2.981 and w' = 5.971. The volumes differ by a factor of 2.

One final practical consideration deals with the production of voltage pulses versus voltage steps. As a rule, voltage pulses are more difficult to produce than voltage steps, given a peak voltage and risetime. For example, charged line pulse generators (see Chapter 4) require twice as much voltage on the switch as is required to produce a simple voltage step. On the other hand, a Blumlein pulse generator requires switch operation in a line having half the impedance of the load, and hence produces a slower risetime pulse. These considerations will generally favor the use of prism systems until satisfactory pulse generators are developed, ones which will permit the tailoring of the pulse to the deflection system.

3.7 Some Typical Designs

Practical deflection systems suffer from two major limitations: the available pulse generators are less than ideal as discussed in the previous section; and it is not usually possible to utilize the optimum number of iterations due to the sheer volume of crystal required and the associated expense of construction. Practical deflectors will therefore have an additional constraint on the amount of crystal utilized. As an illustration consider the use of a 20 cm length of lithium niobate 4 mm thick, and having electrodes 4 mm wide. As a stripline its impedance is then 41 ohms. Using a 10 kV voltage pulse produced by a spark gap having 15 nh of inductance, Equation (3.61) yields t_o = 366 ps. A number of deflector designs are possible. For the lens system of Figure 10, the number of passes, q, and the stripline to mirror spacing, s/2, are related to the stripline length, r, and internal beam angle, θ_1, by

$$(q + 1)(\ell + s) \tan \theta_1 + \ell \tan \theta_1 = r \, . \qquad (3.70)$$

Using q as the dependent variable in Equations (3.36), (3.37), (3.61) and (3.70) yields the design specifications given in Table 3. The minimum q value follows from $w' < Y$ while the maximum q value given corresponds to s = 0, i.e., no separation between the mirrors and the electrode edges.

The best time resolution occurs for q = 24 while the maximum number of spots occurs for q = 52. These separate optimums are

TABLE 3

PRACTICAL DESIGNS FOR LITHIUM NIOBATE

TRAVELING LENS DEFLECTOR (λ = 1μm)

N	τ (ps)	q	w'(mm)	S(mm)	r(cm)
6.5	8.4	9	19.8	37.8	20
34.5	8.1	14	13.2	23.9	20
49.1	8.02	19	9.9	16.9	20
57.8	7.99	24	7.9	12.7	20
63.3	8.01	29	6.6	9.9	20
66.9	8.06	34	5.7	7.9	20
69.2	8.15	39	5.0	6.5	20
70.5	8.3	44	4.4	5.3	20
71.1	8.4	49	4.0	4.4	20
71.2	8.5	52	3.7	3.9	20
70.7	8.8	59	3.3	3.0	20
69.8	9.0	64	3.0	2.4	20
68.5	9.3	69	2.8	2.0	20
66.9	9.6	74	2.6	1.6	20
64.9	10.0	79	2.5	1.2	20
62.7	10.4	84	2.3	0.9	20
60.1	10.9	89	2.2	0.6	20
57.3	11.6	94	2.1	0.4	20
54.2	12.2	99	2.0	0.2	20
51.5	13.0	103	1.9	0.02	20
PRISM DEFLECTOR (λ = 1μm)					
14.5	9.2	17	6.0	---	20

typical of practical designs. The maximum number of spots increases as a function of ℓ/d due to the increased product of total interaction length and electric field, whereas the minimum resolvable time decreases with smaller ℓ/d ratios since this yields higher stripline impedances and faster voltage pulses.

For the prism system of Figure 9, using the same dimensions, we see the resolvable time is comparable to the lens systems; however, the number of resolvable spots is significantly smaller. This occurs partly because the lens system uses a two sided pulse to provide twice the number of spots, and partly because the prism deflector cannot be optimized to the pulse generator.

CHAPTER 4

SUPPORTING SYSTEMS AND TEST APPARATUS

A number of practical difficulties are encountered when implementing and testing a stripline deflection system. The deflector itself requires an appropriate voltage pulse generator, effective matching of the generator to the stripline, an appropriate design using available materials, and high optical quality of the materials and surfaces. Then, a picosecond laser source capable of triggering the deflector pulse generator and providing a pulse to be deflected is needed to complete the test apparatus. This chapter deals with the techniques related to these needs.

4.1 Fast High Voltage Pulse Production

Unavailability of a suitable voltage pulse generator to drive an electrooptic deflector presents the main difficulty in demonstrating a useful device. The requirements for this generator are:

1. High voltage--for a field of 10^7 V/m over 2 mm a voltage of 20,000 volts is needed;
2. Fast risetime--for 20 resolvable spots of 25 picoseconds resolution a pulse width of about 1 nanosecond is required; and
3. Synchronization to the optical pulse being deflected--with jitter of less than the pulse width.

The capability of being able to trigger the deflector with a low level light pulse would also be useful, but many applications do not require this.

Three techniques suggest themselves. Laser triggered spark gap technology has been in use for many years in this service; however, it is somewhat clumsy to use, requires frequent maintenance, and unless very high energy light pulses are available it shows considerable firing delay and unacceptable jitter. Auston demonstrated the photoconductive silicon switch in 1974,[43] and subsequent work has shown it to be a potential candidate offering very fast risetime and perfect synchronization, but at present it cannot meet the voltage requirement of 20 kV. More recently, high voltage switching has been accomplished using photoconductivity in silicon junction devices, but these devices appear to require even more light energy than pure silicon devices and have even more severe voltage limitations.

4.1.1 Photoconducting Switches

The basic photoconductive silicon switch is shown in Figure 13.[44] The microstrip construction enables electrical wave propagation between the IN and OUT connections upon activation of the photoconductive silicon switch in the gap. Initially, a signal cannot propagate across the gap due to the high resistance of the pure single crystal silicon; however, when the gap is illuminated with green light of sufficient intensity, a highly conductive surface layer forms

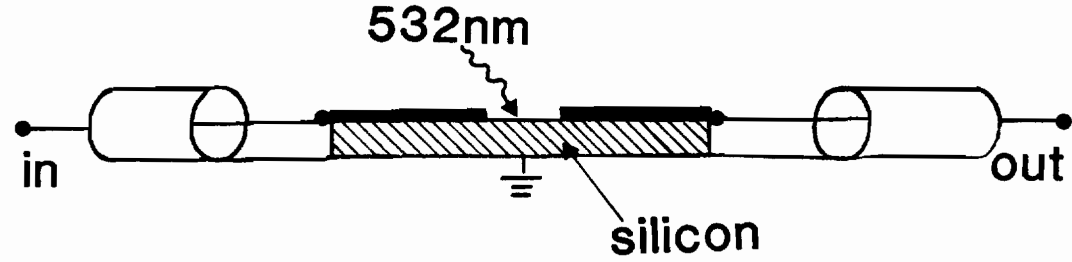

Figure 13a. An optically activated silicon switch. The light induces a conducting surface layer which completes the stripline across the gap enabling conduction.

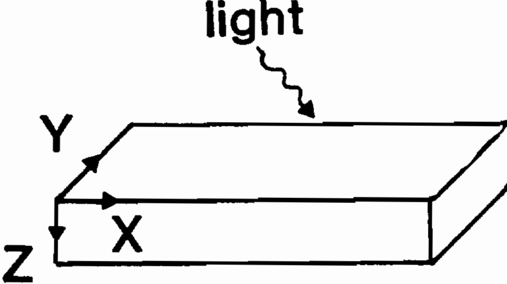

Figure 13b. Coordinate system for analyzing the light activated switch.

allowing electrical signals to propagate across the gap. The time duration of the conductive state depends upon the carrier lifetime, which for pure silicon may be on the order of milliseconds.

To be useful the light pulses must contain sufficient energy to create enough carriers to drop the series surface resistance well below the transmission line impedance. When the illumination is independent of the x coordinate, as defined in Figure 13b, the conductance of a long, thin, rectangular section of material is

$$dG = (\sigma/\ell)dydz \tag{4.1}$$

where σ is the conductivity as a function of y and z. With the conductivity given by $\sigma = e(\mu_n + \mu_p)n$, integration of Equation (4.1) gives

$$G = [e(\mu_n + \mu_p)/\ell] \int_o^t \int_o^w ndydz \tag{4.2}$$

where the carrier pair density, n, is also independent of x. This may be rearranged to the form

$$G = [e(\mu_n + \mu_p)/\ell^2] \int_o^t \int_o^w \int_o^\ell ndxdydz \ . \tag{4.3}$$

But this integral just represents the total number of generated hole electron pairs. For green light of wavelength 532 nm, the absorption coefficient of $\alpha_1 = 2.4/\mu m$ means all of the light will be absorbed in the first few micrometers. Assuming generation of one electron hole

pair per photon and accounting for surface reflection one obtains

$$G = \frac{4n}{(n+1)^2} \left(\frac{\varepsilon}{\hbar w}\right) \left[\frac{e(\mu n + \mu p)}{\ell^2}\right] \quad (4.4)$$

where ε is the energy in the incident light pulse and $\hbar w$ is the photon energy. The gap resistance must be much lower than the stripline impedance, z_o, and this implies

$$Gz_o \gg 1$$

$$\varepsilon \gg \frac{(n+1)^2}{4nz_o} \left[\frac{\ell^2 \hbar w}{e(\mu_n + \mu_p)}\right]$$

$$\ell \ll \left[\frac{4n}{(n+1)^2} \left(\frac{\varepsilon G}{\hbar w}\right) e(\mu_n + \mu_p)\right]^{1/2} . \quad (4.5)$$

At the high fields necessary for acceptable operation, the low field mobility, $\mu_o = \mu_n + \mu_p$, no longer is applicable since the drift velocity in silicon limits at $v_d \approx 10^7$ cm/s.[45] With $E = v_d/\mu$ the end of the linear region occurs when $E_o = 10^7/\mu_o$ giving

$$\mu = \mu_o E_o / E$$

$$\varepsilon \gg \frac{(n+1)^2}{4nz_o} \left[\frac{\ell^2 \hbar w E}{e\mu_o E_o}\right]$$

$$\ell \ll \left[\frac{4n}{(n+1)^2} \left(\frac{\varepsilon G}{\hbar w}\right) \frac{e\mu_o E_o}{E}\right]^{1/2} \quad (4.6)$$

for $E > E_o$.

Note that operation with wavelengths other than green is possible as long as the photon energy is somewhat greater than the 1 eV energy gap of silicon to ensure complete absorption near the surface. For applications where a high energy pulse synchronized to the event of interest is not available, this technique will be of no use. Design curves are shown in Figure 14.

Another consideration stems from the high power dissipation occuring in the silicon during the off state as given by

$$P = V^2 G_o = V^2 wt/\rho \ell \, . \qquad (4.7)$$

For example, with V = 10 kV, w = 2 mm, ℓ = 2 mm, t = 10 um, and ρ = 4000 ohm-cm then P = 25 watts. Several methods exist to minimize this problem. One successful technique employs the use of a pulsed high voltage supply providing low duty cycle pulses[46, 47] synchronized to some point in time before the event of interest. Another suggested technique depends upon the altered properties of silicon at low temperatures.[47] At 77° K the mobility rises by a factor of 30, and the intrinsic resistivity should rise by several orders of magnitude. The resistance increase would of course lower the power dissipation.

One final problem deals with the question of just how large a field can be sustained in a large piece of single crystal silicon. Studies of the intrinsic properties within junction regions indicate avalanche multiplication sets in at fields of 2×10^7 V/m; however,

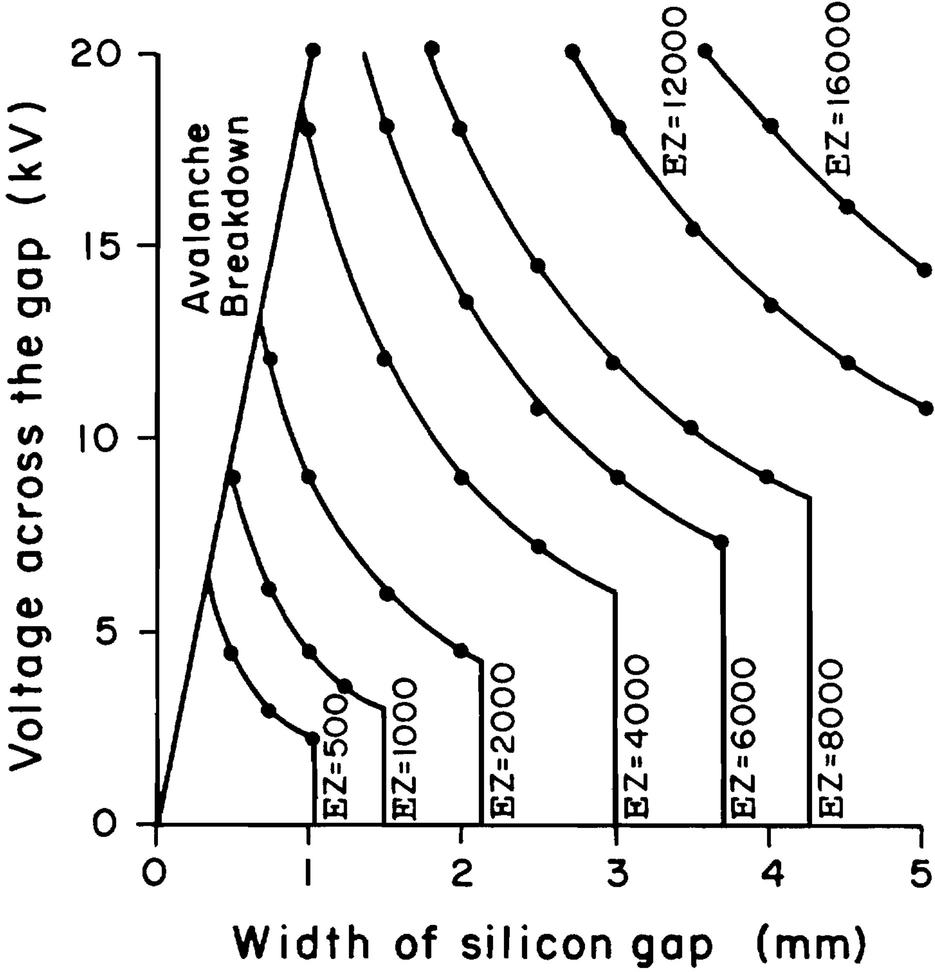

Figure 14. Design chart for light activated silicon switches.

1) Choose the switch operating voltage.
2) Decide on the width of the silicon region.
3) Determine the appropriate EZ value from the above chart.
4) Divide by the impedance of the stripline to obtain the required pulse energy in microjoules of 532 nm light.

experimental studies of these photoconductive switches indicate breakdown effects occurring at much lower fields.[47] One successful technique to avoid a breakdown problem used a spark gap as a pulsed high voltage source for the silicon. When the silicon was triggered within 2 ns of the voltage pulse onset, successful operation occurred, with longer delays resulting in breakdown (either on the surface or in the air).[47]

In designing a silicon switch, this author chose to try and solve the power dissipation problem by operating at a low temperature. Some 8000 ohm-cm resistivity silicon was obtained, and after cutting a wafer from the boule, electrodes were fastened to the wafer by sputtering a thin gold-palladium layer onto the sample corners followed by indium soldering of gold wires. Hall and conductivity measurements were then made for temperatures in the range of 77° K to 300° K using the Van der Pauw technique,[48-51] and from this data the resistivity, Hall mobility, electron density, and Fermi level were calculated according to

$$\rho = 1/\sigma,\ \mu_H = R_H\sigma,\ n = 1/eR_H,\ \text{and}\ (\varepsilon_F - \varepsilon_c) = -kT/n(N_c/n) \quad (4.8)$$

where ρ is the resistivity, μ_H the hall mobility, R_H the hall coefficient (measured), σ the conductivity (measured), $e = 1.6 \times 10^{-19}$ coulomb, k being Boltzman's constant, and $N_c = 5.45 \times 10^{15}\ T^{3/2}\ /cm^3$ the conduction band effective density of states. The results are plotted in Figures 15 and 16. The mobility changes by a factor of 30

Figure 15. Silicon properties vs. temperature.

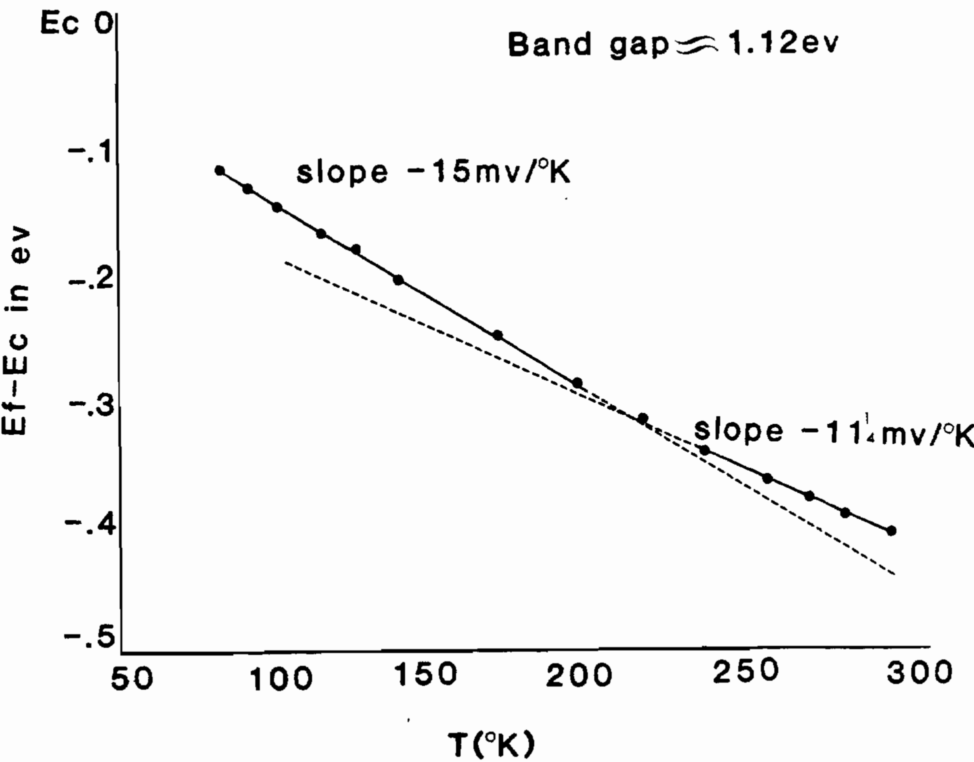

Figure 16. Fermi level plot for the silicon sample indicating possible deep level traps at about .3 eV below the conduction band.

as expected, but the resistivity actually drops by a factor of 4 on lowering the temperature. This occurs because the density of carriers stabilizes due to impurities rather than dropping rapidly as hoped for. The decreased mobility then results in a decreased resistivity. Operation at low temperatures in order to decrease power dissipation will accordingly be ineffective.

The flat portion of the electron density curve shows that the number of shallow donors, less the number of acceptors, must be about 5.4×10^{11} per cm^3, while the Fermi level plot suggests a deep level trap near 0.32 eV below the conduction band. At the highest temperature shown the electron density reaches $3.9 \times 10^{12}/cm^3$, most of which has come from the deep level traps. Accordingly, the trap density must be approximately 3.4×10^{12} per cm^3.

This analysis shows the importance of careful control over impurities if high resistivity at low temperatures is to be achieved. To increase the resistivity by three orders of magnitude, while increasing the mobility by a factor of 30 as the temperature drops, necessitates a drop in electron density by over four orders of magnitude. This means a careful balancing of shallow impurity levels and acceptor levels to within a density of $\Delta n \approx 10^8$ per cm^3. This would be difficult indeed. Alternatively, some other technique might be used such as the introduction of iron centers to control the electron density at low temperatures. The main conclusion to be reached here is that the selection of material for this application proves to be difficult and cannot be made on the room temperature properties of the silicon.

In addition to determining the low temperature usefulness of the silicon, some high field measurements were made. The electrode arrangement on the silicon for the first experiment is shown in Figure 17a. With 100 V - 4000 V pulses having risetimes of 3 ns and falltimes of 200 ns applied to the electrodes, the voltage curve in Figure 17b is measured across the silicon. For voltages of less than 500 volts, the pulse rises in 3 ns and decays in 200 ns as expected, but when over 500 volts is applied, the silicon breaks down within several ns, decays to 500 volts in 10-40 ns depending upon the peak voltage, and then decays the remaining 500 volts in 200 ns or more.

Another sample prepared with a slightly different electrode arrangement (Figure 17c) and potted in clear silicon rubber, GE type 615, produced similar results. Application of 6 kV induced arcing along the surface from the top electrode to a point just over the second electrode. With this sample the breakdown occurs at 2 kV rather than 500 volts, and with the higher voltages the decay from breakdown to 2 kV takes nearly 400 ns.

From these measurements it is clear that breakdown occurs through the silicon at fields near 10^4 V/cm and is not due to surface or air breakdown. This field is far below the avalanche field of 2×10^7 V/cm typical of p-n junctions in silicon, effectively ruling out carrier multiplication by excitation across the gap. Since the deep level traps are active at room temperature as evidenced by the rapidly changing electron density in Figure 15, the process may be due

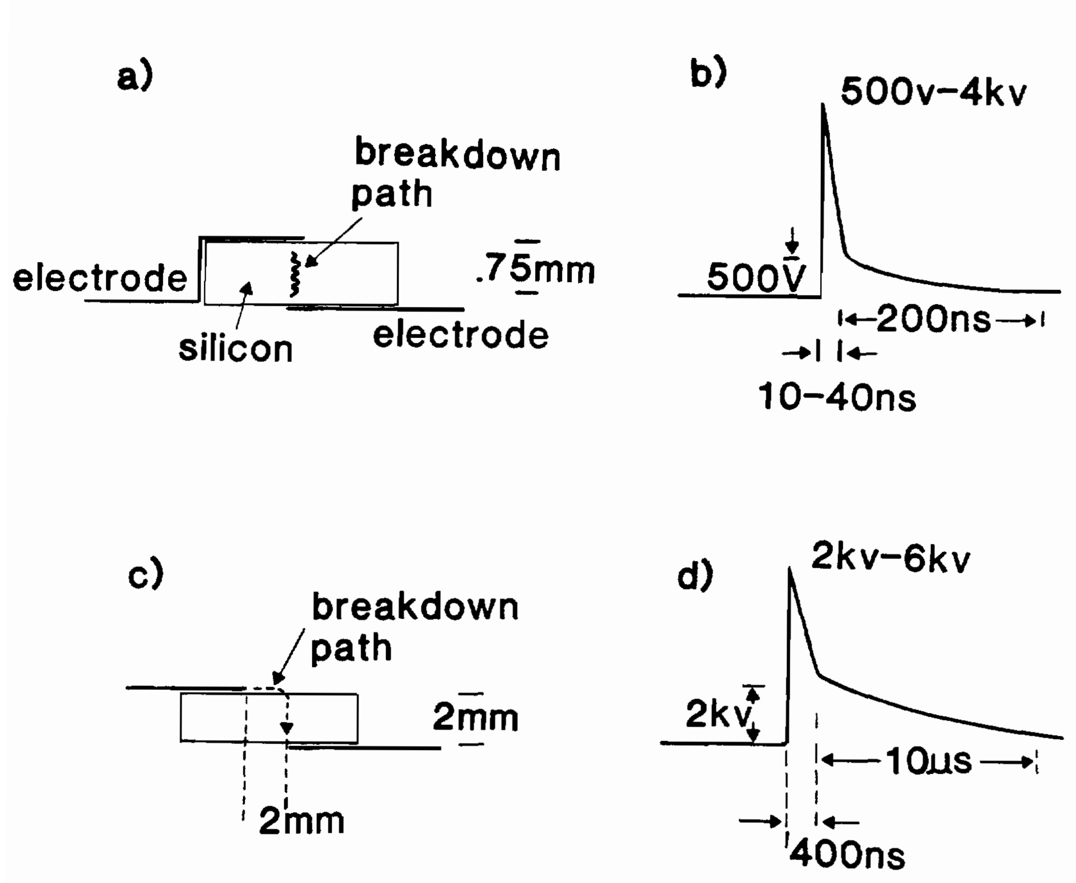

Figure 17. Silicon switch electrode geometries and breakdown voltage waveforms.
Thin sample at a) tested with voltage pulse having 3 ns risetime and 200 ns falltime.
A thicker sample at c) was tested with a voltage pulse having 3 ns risetime and 10 ns falltime. b) and d) show the voltages measured across the silicon.

to ionization of deep level trapping centers. In any case, the low fields attainable severely limit the usefulness in this application since wide gap regions enabling high voltage standoff make very high energy light pulses necessary for switching. It appears that the technique of pulsing the high voltage with a fast risetime pulse followed by switching within several nanoseconds is the only useful technique for silicon photoconduction at present, but as the design chart shows this technique requires high energy light pulses to switch high voltages in the low impedance striplines such as those used in KDDP based deflectors. For example, with 10 kV across a 2 mm gap (which might be a high enough voltage) in a 10 ohm charged line pulser, a pulse of 500 μJ of energy at a wavelength of 532 nm is needed to activate the switch.

The high resistivity of GaAs has prompted an attempt to use it as a high voltage switch. The results have not been promising.[52] With 5 kV applied across the GaAs, the maximum output pulse obtained was 600 V. The cause of this low voltage stems from intervalley scattering of carriers to the low mobility bands. The consequent low mobility of carriers will not allow the conversion of the gap resistance to a sufficiently low value. The effect is precisely the same as that involved in the negative differential conductivity property utilized in the Gunn effect.

4.1.2 Photoconductivity in Silicon Junctions

Some recent work using thyristors, PNPN four layer devices, has shown some promise; however, the demonstrated capability at present is far below that required for this application. The advantage of the junction devices lies in their ability to hold off relatively high voltages at very low power dissipations. The theory of the previous section applies here, where operation is now in the region of maximum drift velocity, $v_d \approx 10^7$ cm/s, and electric field near breakdown, $E_{max} \approx 2 \times 10^5$ V/cm, since fields near the avalanche point are obtainable in the depletion regions of the PN junctions. The appropriate depletion width must be used for ℓ of the previous section.

Preliminary results[53] have demonstrated blocking voltages of 1500 volts, maximum currents of 10,000 amps, and risetimes of two nanoseconds corresponding to a dI/dt of 1000 amps per nanosecond, with indications that even shorter risetimes may be attainable. This dI/dt satisfies the pulse generator requirements nicely, but the blocking voltage is quite low, and the required pulse energy of 3 mJ is quite high. At present, therefore, these devices appear to be of little value in this application.

4.1.3 Spark Gaps

A number of researchers have reported on the operation of laser triggered spark gaps, including a variety of configurations capable

of operation over a wide voltage range.[54-59] Typically, voltages of 10-20 kV have been switched with risetimes of a nanosecond or less. Usually, operation has been in a 50 ohm coaxial environment, although results using a 10 ohm system have been reported.[56]

Spark gap operation is controlled by many factors. The gap spacing, gas type and pressure, and applied voltage all exert some control over firing delay time. Normally they are adjusted so the gap is near breakdown field strength. Optimum operation for production of a 10 kV pulse requires a gap of one half millimeter and a nitrogen pressure of 165 lbs.[57] Another important parameter is the laser pulse energy. For tungsten targets a minimum of 22 microjoules is required in a time period of 200 ns - 300 ns, while more energy is required for other common materials since their lower melting points inhibit the thermionic emission mechanism.[59]

This research has utilized three spark gap systems, the earliest version being a stripline system in a low impedance, 8 ohm, environment. Considerable experimentation with this system proved it to be unacceptable due mainly to a switching time of 8 to 10 nanoseconds. Figure 18 details the firing delay for various nitrogen pressures and gap widths, these being characteristic of spark gap systems in general. A very acceptable value of jitter occurred, usually only a nanosecond or two. The slow switching time appeared to be a function of the geometry and low impedance; however, a contributing factor may have been the very poor quality mylar stripline used in its construction.

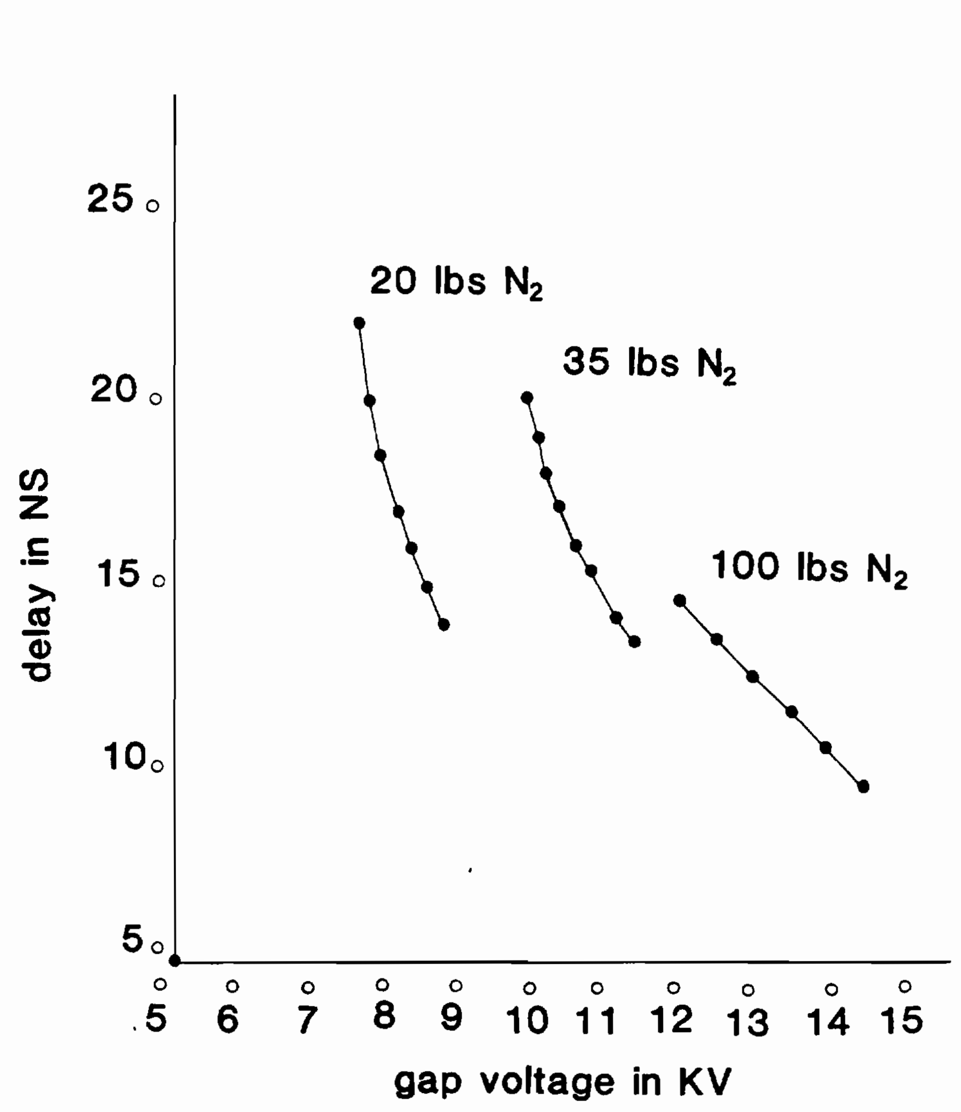

Figure 18. Characteristics of mylar dielectric, stripline, spark gaps.
For all cases the voltage pulse produced was 15-20 ns long for a design impedance of 8 ohms.

A 12.5 ohm coaxial system proved to be far superior to the strip-line system. Standard copper pipe sizes were used throughout to simplify construction. In order to inhibit electrical breakdown between the inner and outer conductors and across the gap itself, the entire system was pressurized to 200 lb. of nitrogen. This pulse generator performed reasonably well and provided the voltage pulse used in one set of deflection experiments. Its output pulse was 8 kV with a full width at the baseline of 3 ns, corresponding to a risetime of under 1 ns, this being close to the 1 ns risetime in 10 ohms reported by Michon.[56] Unfortunately, the coaxial to stripline coupling system we employed at its output deteriorated the pulse width to 5 ns resulting in poor overall performance of the pulse generation system.

The third spark gap was modeled after Alcock et al.[57] This coaxial system was designed for 50 ohm operation using standard RG8U coaxial cable. The gap generated a pulse of 10-12 kV with a full width at the baseline of 2.5 ns. The corresponding risetime of 1 ns is still somewhat more than obtained by Alcock. The reasons for this are unclear, but may be related to difficulties we had in obtaining laser pulses of sufficient energy to ensure optimum operation of the spark gap.

As a pulse generator the spark gap should be characterizable by an equivalent inductance, L, defined according to $\tau_R = L/R$ or $L = \tau_R z_o$ where z_o is the line impedance and τ_R the corresponding risetime.

Data from several sources show

$$L \approx (0.3\ \text{ns})(50\ \text{ohm}) = 15\ \text{nh}.$$ [57]

$$L \approx (1.0\ \text{ns})(10\ \text{ohm}) = 10\ \text{nh}.$$ [56]

$$L \approx (1.0\ \text{ns})(50\ \text{ohm}) = 50\ \text{nh}.$$ [58]

$$L \approx (1.5\ \text{ns})(12.5\ \text{ohm}) = 19\ \text{nh}$$

$$L \approx (1.25\ \text{ns})(50\ \text{ohm}) = 62\ \text{nh}$$

the last two being the author's results. The variations are due, presumably, to differences in laser characteristics used for triggering, different geometries, and different target materials. The first two suggest an optimum of 10-15 nh, which was used for numerical examples in Chapter 3.

4.1.4 Pulse Forming Networks

Multiple prism deflection systems require a voltage pulse in the form of a linear ramp. If the deflector can tolerate being charged to the peak operating voltage for extended periods of time this requirement follows easily; the transmission line is charged and an appropriate high voltage switch shorts one end of the transmission line. This produces a voltage ramp which then propagates down the line. Departures from linearity of the ramp will cause some nonlinearity in the time resolution as a function of deflection angle, but simple

calibration procedures should minimize this inconvenience. In addition, some degradation of the spot size would occur, but this should not be serious.

The main difficulty with this technique arises from the high fields present in the charged deflector. Ordinarily these fields will be much greater than the dielectric strength of the surrounding air, thereby mandating the use of optically contacted, high dielectric strength materials. Index matching fluid is commonly used, but problems occur due to heating and subsequent turbulence effects in the fluid.

A more satisfactory solution follows from the use of a pulse forming network to provide a two sided pulse. The deflector may then idle with no applied field, while only the leading edge of the applied voltage pulse is used for deflection. Due to the short time duration of this pulse, the peak field generated may exceed the static dielectric strength of the deflection system without causing breakdown. This is possible since dielectric breakdown usually takes several nanoseconds in most materials, and the high fields due to the pulse are not in one place for sufficient time to allow breakdown. This leads to a considerable simplification of system design. A pulse forming network must be used for the traveling lens deflector system since its operation depends on a two sided pulse.

The most widely used pulse forming technique is illustrated in Figure 19.[60] The short section of line at the left is charged to

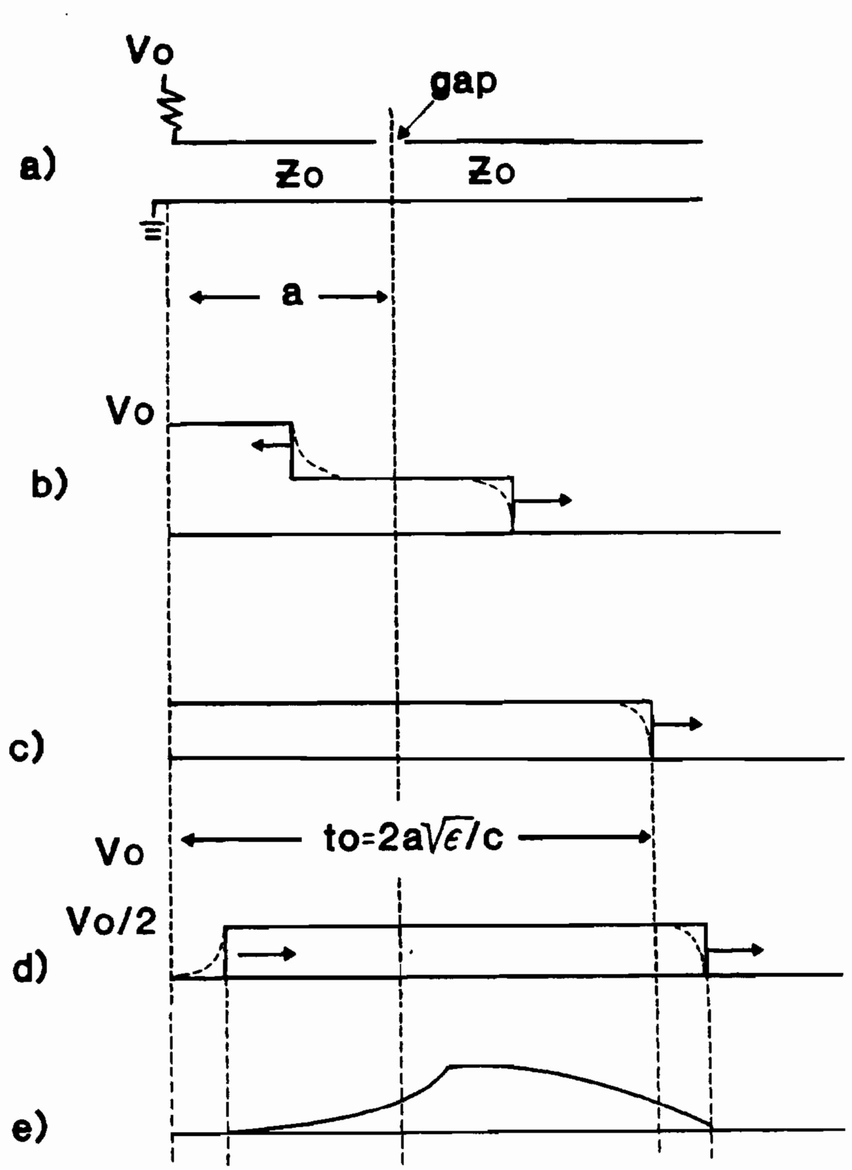

Figure 19. Simple charged line pulse forming network.
a) Mechanical construction.
b) Voltage distribution shortly after gap is shorted.
c) Voltage distribution when traveling wave reaches the left end.
d) Voltage distribution of final pulse.
e) Real pulse.

the supply voltage, V_o, establishing a field, E_o, in the transmission line dielectric (Figure 19a). The right side, being isolated from the supply voltage, remains at $V = 0$ while the switch is open. When the switch is closed, continuity of voltage and current through the switch requires the formation and propagation of two electromagnetic waves in the transmission lines. One wave having an electric field of $E_o/2$ moves to the right and leaves behind its leading edge a voltage of $V_o/2$, while to the left, a field of $-E_o/2$ travels leaving behind its leading edge a field of $E_o - E_o/2 = E_o/2$ and a voltage of $V_o/2$ (Figure 19b). The voltage at the switch has dropped to $V_o/2$, and a current of $V_o/2z_o$ flows everywhere between the two propagating wave fronts.

When the left hand wave reaches the open ended line it is reflected (Figure 19c). As it moves to the right, it cancels out the remaining $E_o/2$ field and $V_o/2z_o$ current leaving behind a voltage and current of zero. As depicted in Figure 19d a square pulse of time duration $2a\sqrt{\varepsilon}/c$ and amplitude $V_o/2$ now propagates to the right.

In practical switches the edges of these pulses are not square; instead, they have finite rise and fall times as shown by the dotted lines. By shrinking "a" until the risetime equals $2a\sqrt{\varepsilon}/c$, a smoothly varying pulse of width $4a\sqrt{\varepsilon}/c$ is obtained as depicted in the last frame of Figure 19. This pulse is now suitable for the deflection applications considered here. Note that the switch must withstand twice the voltage of the required pulse as must the left hand side of the transmission line.

Many other techniques for pulse formation have been described in the literature and in books dealing with pulse technology.[61] Some, such as the Blumlein arrangement, provide a pulse of height equal to the supply voltage, but the switch operates in a $z_o/2$ environment resulting in a slower risetime. Techniques for special applications, such as the one described later in relation to single pulse selection, are numerous, with each having its own advantages and disadvantages, but few have the simplicity of the charged line pulse generator described above.

4.2 High Voltage Pulse Transmission and Coupling Techniques

The high voltage driving pulse provided by the pulse generator must be coupled from the generator to the deflector and subsequently out of the deflector. In deciding on the best technique to be used at each transition, the designer must consider the following: the high voltages involved, typically 10-20 kV, tend to cause dielectric breakdown in the transmission line dielectrics and in the surrounding air; spark gap pulse generators are coaxial devices while the deflectors are stripline devices; spark gaps usually operate at the impedance of common coaxial cables, 50 or 75 ohms, whereas the deflector may provide a much lower impedance load; and finally, the dielectric constants of stripline dielectrics will not usually match that of the crystal used in the deflector. Each of these factors leads to difficulties in transmitting the maximum pulse voltage with minimum distortion and/or reflection at a transition point. Each will be considered in what follows.

4.2.1 Transmission Lines

Four types of transmission lines have been used in this research. The first was a mylar based stripline fabricated with 10 mil mylar sheet for a dielectric and brass shimstock for electrodes. Difficulties first appeared with this line in the charged line section of a stripline pulse forming network and subsequently in the transmission side also. Continuous voltages of 20 kV caused deterioration of the mylar dielectric, culminating in dielectric breakdown after several days of operation. Increasing the thickness to 20 mils by using two sheets proved to be of little value. In addition, pulse broadening occurred in short sections of this transmission line, apparently due to impedance nonuniformities along the line as a result of nonuniform electrode width and separation. Our experience indicates that in high field, fast pulse applications mylar performs poorly as a dielectric material.

We constructed a second form of transmission line using copper tubing for conductors and pressurized nitrogen for a dielectric. Nylon spacers worked well for separating the inner and outer conductors on the transmission line side of the pulse generator, but occasional arcing in the charged line eventually deposited sufficient carbon on the spacers to force disassembly and cleaning of the unit. Eventually, a technique evolved for supporting the inner conductor of the charge line at its ends, thereby removing the need for spacers. This technique worked very well for construction of a 12.5 ohm, 10 kV

pulse generator; however, coupling of the pulse to another form of transmission line proved difficult. Broadside connection to a mylar stripline was used (see Figure 20), but it was quite unsatisfactory, not only because of the problems with the mylar, but also because of the drastic discontinuities occurring at the coupling which broadened the pulse width from 3 ns to 5 ns.

Standard RG8U coax cable performs the best in the pulse forming network. It withstands 25 kV indefinitely, and 30 kV for short times, with no apparent ill effects. It is flexible, easy to couple to, requires no construction, and is commonly available. The 50 ohm impedance necessitates an impedance change before coupling to the crystal; however, the high impedance leads to a fast pulse risetime which partially offsets the voltage loss incurred during the impedance transformation.

A suitable form of stripline is still required for connections into and out of the deflector. Satisfactory results have been obtained through the use of copper clad, teflon glass microwave material available from 3M in a number of thicknesses, dielectric variations, and tolerances. Using 15 mil dielectric thickness, a number of sections with various impedances were constructed. Excellent results were obtained when photographic etching was used to define the electrodes; however, this process is relatively expensive and has a long turnaround time. Scribing the copper and peeling the unwanted metal away from the dielect produced satisfactory stripline sections for

operation below 5 kV; the scribing procedure, however, damaged the dielectric slightly and resulted in dielectric breakdown when 10 kV pulses were propagated down the line.

4.2.2 Transitions

In this application transitions in the transmission line system fall into three types: coaxial to stripline geometry alterations, dielectric changes requiring corresponding dimensional changes, and impedance transitions between the pulse generator and deflection system. Geometrical and dielectric transitions must be made in such a manner so as to pass the electrical pulse with minimal distortion and/or reflection; thus, minimization of the inherent discontinuities of these transitions arising from the differences in electric fields in the two lines is required. Impedance discontinuities, on the other hand, cannot pass the pulse unchanged. Either the peak height, or pulse width, or both must change.

The coaxial to stripline transition can be accomplished in several ways. Since the voltage pulse is a guided TEM 00 wave, the transition should disturb the electromagnetic fields as little as possible. The broadside coupling technique illustrated in Figure 20a minimizes the physical size of the discontinuity region, but it presents a drastic change to the electromagnetic fields since they must change from one plane to another plane perpendicular to the first. This coupling performs well at low frequencies, but it reflects more and more of the pulse energy as the frequency increases.[62] Figure 20b

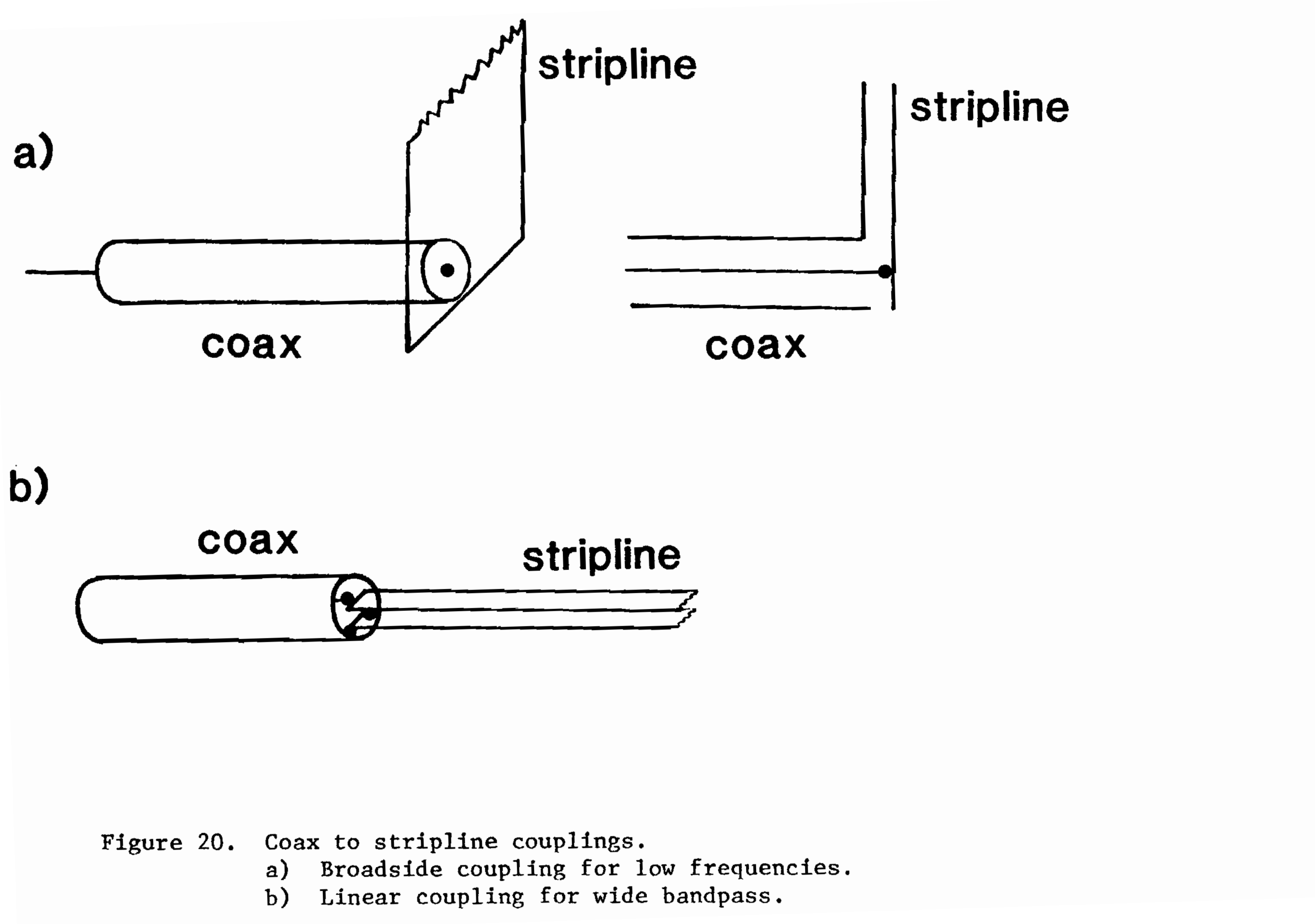

Figure 20. Coax to stripline couplings.
a) Broadside coupling for low frequencies.
b) Linear coupling for wide bandpass.

illustrates a more satisfactory technique. The size of the discontinuity region is again small, but now the fields exist in the same planes in both guides. A slight capacitive discontinuity occurs at the junction, but it is possible to tune this out and create a perfect match if desired.[63] This technique, however, is susceptible to high field breakdown at the points where the upper stripline electrode is near the outer coaxial electrode, and the use of silicon rubber, RTV, or corona dope is mandatory in order to avoid air breakdown. For very high voltages, implying thick and wide striplines, this approach may be unusable, forcing a return to the previous method.

The problem of dielectric changes proves to be more difficult to solve. The transition from transmission line to deflector stripline must have as small a discontinuity as possible, not only to avoid degradation of the voltage pulse, but to enable double pass operation of the deflector as described later. This mandates impedance continuity. To allow for changes in the dielectric constant and maintain a fixed impedance, either the dielectric thickness or electrode width or both must change. Any of these changes presents a slight capacitive discontinuity. Because these transitions involve dielectric changes, the analyses are difficult and none exist in the literature; however, the discontinuity values should be similar to those discussed in the next paragraph.

Impedance transitions present the most challenging transition problem. Abrupt changes are the simplest, and they operate uniformly

over a very broad band from d.c. to microwave frequencies with uniform voltage reflection and transmission coefficients given by the simple relations

$$T = 2z_1/(z_1 + z_2) \quad \text{and} \quad R = (z_1 - z_0)/(z_1 + z_0) . \qquad (4.9)$$

Theoretical analyses exist for both width and thickness steps in uniform dielectrics.[64-66]

Tapered transmission line sections, on the other hand, offer potential gains over the simple abrupt transitions. Whereas the abrupt transition acts as a low pass filter tending to broaden the pulse, a tapered section behaves as a high pass filter,[67-70] and with proper design can cause pulse width narrowing. At low frequencies where the wavelength is long compared to the taper length, Equations (4.9) describe their behavior, while at high frequencies nearly complete power transfer occurs giving voltage transmission and reflection coefficients of

$$T = \sqrt{z_1/z_0} \quad \text{and} \quad R = 0. \qquad (4.10)$$

Accentuation of the high frequency energy over the low frequency components of a pulse can lead to a narrower pulse width of greater amplitude than predicted by Equation (4.9). Experiments verify this at low voltages (using an exponentially tapered line); however, dielectric breakdown at high fields prevented our use of the line in actual deflection experiments. The high impedance end of the taper

must be capable of withstanding the full pulse height of the generator, whereas an abrupt change located close to the coaxial to stripline transition need only withstand the voltage determined by T in (4.9).

4.3 Light Pulse Generation

In order to test the deflector, suitable light pulses capable of triggering the voltage pulse generator, being deflected, and subsequently being detected must be available. For spark gap systems the energy must be greater than 30 microjoules and be delivered in a period of two to three hundred nanoseconds as stated earlier. The wavelength is relatively unimportant so long as it is absorbed by the metal target. For the pulse to be deflected, however, a pulse shorter than the expected resolution time of the system proves most useful. In addition, it must be in the transparency range of the deflector crystal, and for preliminary testing, preferably be in the visible region for ease of alignment and simplicity of observing deflector operation. Whereas the spark gap will successfully function when triggered by a train of pulses, detection of the deflected pulse is most easily accomplished with a single pulse. In order to synchronize the two events a train of fast pulses generated by a mode locked laser is used to trigger the spark gap, while a single pulse selected from the train is converted to the visible region and sent to the deflection system.

4.3.1 The Oscillator, Amplifier, and Doubler

The basic oscillator consists of a flash pumped Nd:YAG laser rod, 1/4 inch in diameter by 3 inches long. The resonator was plane parallel, consisting of 100% reflecting mirror and a 50% reflecting output mirror, both coated for operation at the laser wavelength of 1064 nanometers. Apertures restrict operation to the fundamental spatial mode while also protecting the o-ring rod seals from the high intensity radiation. Horizontal polarization of the beam is insured by a Brewster angle thin film polarizer within the cavity. Short pulses are obtained by circulating a mode locking dye through a dye cell contacted to the 100% mirror.

For reasons explained in the next section, several configurations using the above layout were investigated. Table 4 summarizes the unique features of each. The dye concentrations are only approximate, being experimentally adjusted to provide stable mode locking in a dye cell of 1.5 mm thickness. Burst to burst instability proved to be large, with variations of at least 2:1 in total output energy; this not being a crucial factor in our experiments, no attempt was made to improve on it.

Some experiments, requiring more energy per pulse than the oscillator could produce, used a second flash pumped Nd:YAG rod as an amplifier. The second rod, pumped simultaneously with the first, provided a single pass gain of 4 to 5 depending on pumping energy.

TABLE 4

OSCILLATOR AND MODE LOCKING CONFIGURATIONS

	Radius of 100% Reflecting Mirror	Cavity Length	Mode Locking Dye	Dye Solvent	Dye Concentration	Output Pulse Spacing	Number of Output Pulses
I	2 m	1 m	Eastman 9740	1,2 Dichloroethane	2 mg dye per 300 ml solvent	4 ns	24
II	2 m	1 m	Eastman 14015 (BDN)	DMSO	Saturated	4 ns	7
III	flat	2 m	Eastman 9740	1,2 Dichloroethane	2 mg dye per 300 ml solvent	9 ns	24
IV	flat	2 m	Eastman 14015 (BDN)	DMSO	Saturated	9 ns	7

To generate the visible light for the deflection experiment, an angle tuned, KDP frequency doubler 30 mm long produced 532 nanometer green light. A dichroic mirror placed beyond the doubler separated the green from the infrared for later use. Typically, the doubler converted 10-20 percent of the infrared to green.

4.3.2 Single Pulse Selection

Selection of a single pulse from a train of pulses enables several experiments to be done. First, it greatly facilitates deflection experiments. When the lens deflector is used, light pulses arriving too early or too late to be deflected arrive at the output plane in the center of the sweep region where they can contribute to system noise. If they are of sufficient energy, they may completely mask the desired measurements. This is not a problem in the prism system since the deflection region does not overlap the undeflected beam position. In the voltage measurement technique to be described later, additional incoming light may completely mask the desired data; hence, single pulse selection is mandatory if a pulse train serves as the light source. Beyond these immediate concerns a single, fast pulse is desirable for other types of experiments. For example, in fluorescence studies excitation before interaction with the desired pulse may render the acquired data useless. For these reasons considerable effort has been expended to develop a simple, reliable, single pulse selection system.

The basic switchout system uses the linear electrooptic effect to cause polarization rotation of the light when an electric field is applied to the crystal. With a KDP crystal located between crossed polarizers, the polarizers are adjusted for maximum light at the crystal and minimum light transmission through the pair. Application of the appropriate half wave voltage to a properly oriented crystal then causes transmission of light through the second polarizer. A second arrangement using a Brewster angle polarizer and a 100% mirror enables operation at half the voltage; the light travels through the polarizer and crystal, is reflected by the mirror and travels back through the polarizer and crystal. When a field is applied to the crystal the light incident on the polarizer for the second time will be reflected rather than transmitted since its polarization will have been altered by two passes through the crystal. The two passes of light through the crystal allow application of only half the field (1/4 wave voltage) in order to produce the same cumulative effect. Operation of this device requires that the voltage pulse applied to the crystal should have a duration approximately equal to the pulse to pulse spacing of the incident pulse train. The half wave voltage varies inversely with wavelength and for KDP (using the r_{63} tensor component) is approximately 7 kV for a wavelength of 1 um. The double pass arrangement should then operate with 3.5 kV. Experimentally, a voltage of 5 kV resulted in switch out of 80-90 percent of the energy of a single pulse.

Our initial work utilized avalanche transistors to secure the desired electrical pulse. They proved superior to spark gaps in terms of reliability but inferior in regard to rise and fall time of the pulse. Figure 21 shows the schematic of this system. Initially both chains of transistors hold off 5600 volts to maintain a zero voltage differential across the crystal. The pulse train incident on the photodiode switches T1 into conduction, resulting in a 5 ns wide, 30 volt pulse across R4, which propagates through the two cables causing the first chain to switch, followed 3 ns later by switching of the second chain. The difference in switching times places a pulse across the crystal. The fastest fall times for each chain were near 4 ns, being primarily controlled by the inductance of the circuit wiring.

Using a 60 cm laser cavity to obtain 4 ns pulse separation, this switchout performed in an unsatisfactory manner. The slow falltime across the chains resulted in a reduced voltage of 7 ns duration, enabling switchout of only 50% of a pulse and frequently part of a second pulse. In addition, jitter in the triggering circuit would cause the time of switchout to vary over the entire pulse train, thereby creating large variations in the energy of the switched out pulse, which in turn resulted in very poor operation of the spark gap when triggered by this pulse. The device is, however, reliable for many months of operation when used several hours a day at a switching rate of 5 times per second. The long time constant of R2

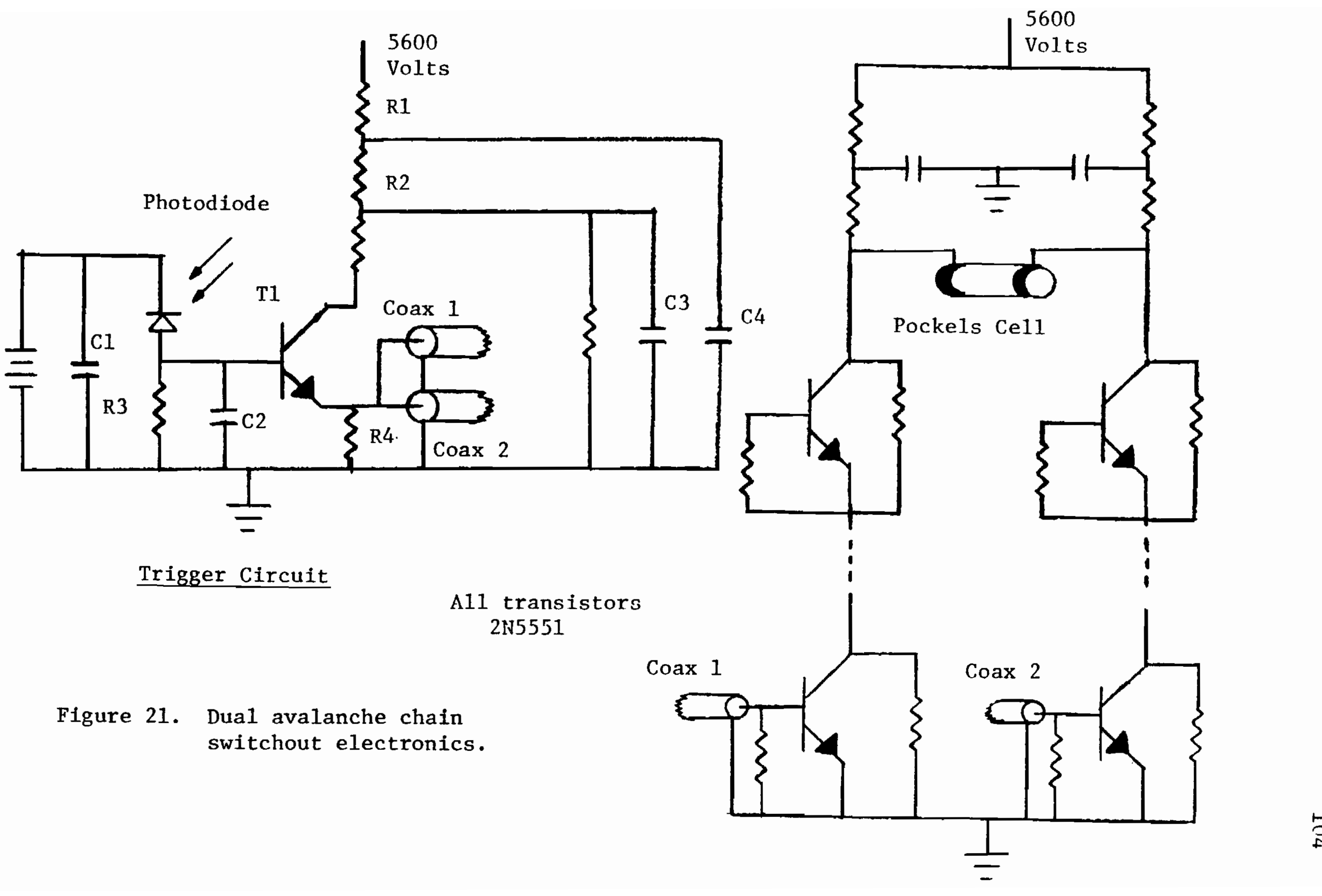

Figure 21. Dual avalanche chain switchout electronics.

and C3 insures that the transistors cannot be refired by a second pulse in the same burst, or even by another extraneous burst resulting from poor mode locking, thus ensuring low duty cycle operation leading to very low transistor failure rates.

In order to devise a more acceptable pulse selector several changes were made. First, the oscillator cavity was lengthened to provide pulse separations of 10 ns in order to relax the pulse width constraints on the switchout pulse generator. Secondly, a krytron replaced the avalanche transistors as the primary switching element, along with the addition of a pulse forming network enabling operation with only one switch. Lastly, operation of the oscillator using Eastman 14015 dye provided a shorter pulse train with more energy per pulse.

The schematic of the improved circuit appears in Figure 22. As before, the photodiode triggers an avalanche transistor which subsequently triggers Q1. The large pulse generated across R6 then triggers the krytron, with transformer coupling providing isolation in order to keep the large pulse across R6 from being fed back into the base emitter circuit of Q1. Two milliamps of keep alive current are supplied to the krytron for 150 μs in order to drop the firing delay from the rated 40 ns delay down to 10 ns delay, in addition to possibly shortening the fall time of the pulse.

The insulating jacket is removed from the pulse forming coaxial cable which is then coiled as shown in Figure 22, and

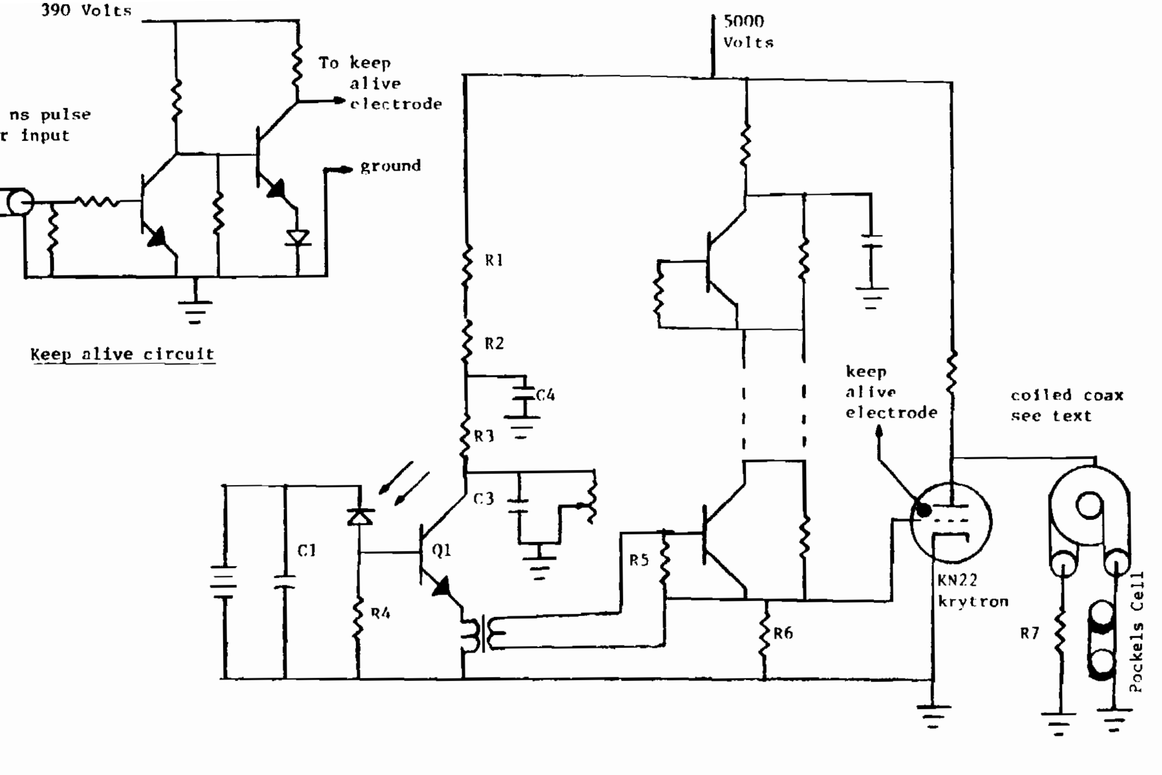

Figure 22. Krytron switchout electronics.

the braid soldered to tie the turns together electrically. Initially, the coax acts like a capacitor charged to the operating voltage, V_o, while the potential across the Pockels cell is held to zero by R7. When the krytron conducts, the outer conductor potential drops to ground potential uniformly over its entire length due to the interconnection of the turns in the coil, but the field in the coax does not disappear immediately. Consequently, a voltage of $-V_o$ appears across the Pockels cell and R7 simultaneously. Voltage and current continuity at the coax-R7 connection require the formation of a traveling wave of magnitude $V_o/2$, which then propagates down the 5½ foot cable to the Pockels cell in 8 ns. The wave reflects at the Pockels cell (which behaves essentially as an open circuit), dropping the voltage there to zero, and travels back to R7 where it dissipates in R7, having now completely discharged the cable. The outcome is a pulse of height $-V_o$ on the Pockels cell for a time duration of slightly over 8 ns.

This technique works much better than using two avalanche chains. Oscilloscope measurements of the pulse across the Pockels cell show a drop to -4.5 kV in 1.5 ns, followed by a flat region of 7 ns at -4.5 kV, followed by a rise back to zero in 1.5 ns. The pulse shape is excellent and of proper duration for use with the 10 ns pulse spacing of the longer oscillator cavity.

A statistical analysis of the switchout performance is summarized in Figure 23 for operation with each of the two mode

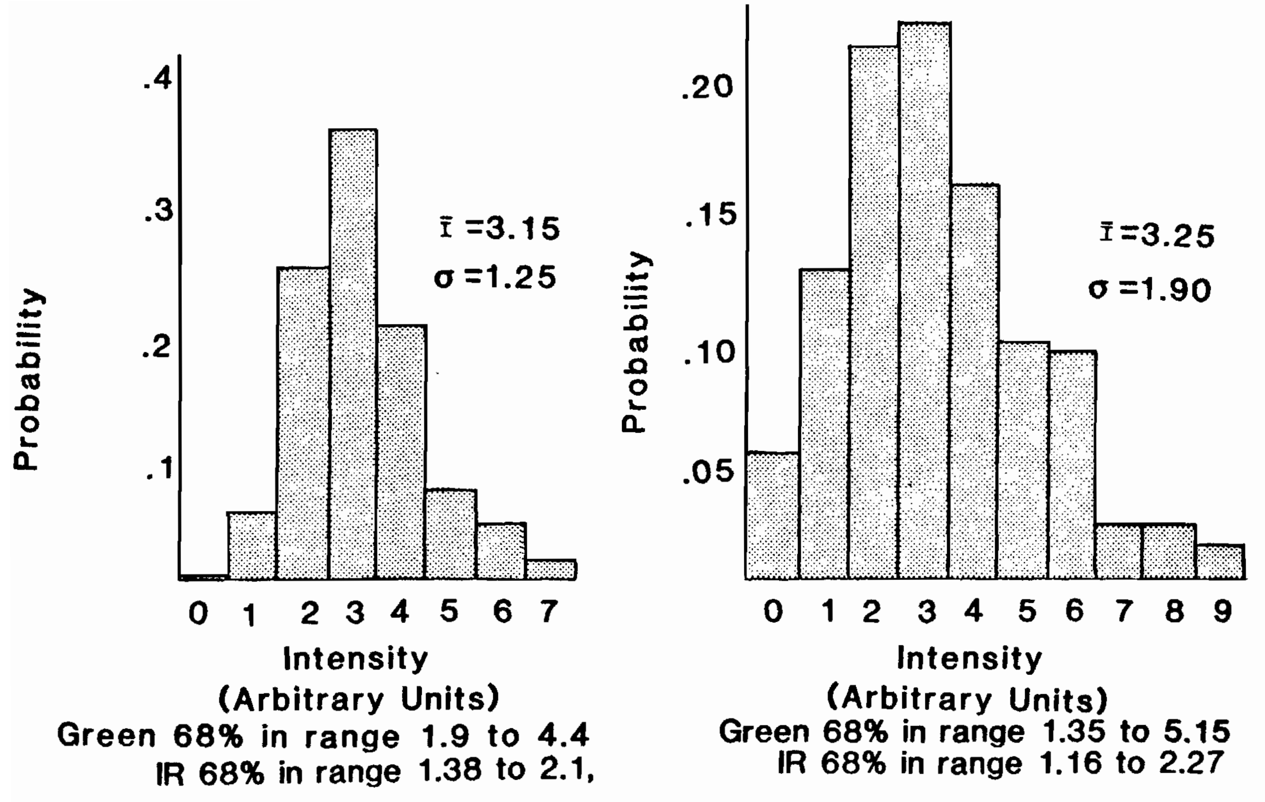

Figure 23. Operating characteristics of the single pulse selector. These graphs show the intensity distribution of the pulses provided by the switchout system. The left side was obtained when Eastman 9740 dye was used in the oscillator while the right side is for Eastman 14015 dye.

locking dyes. The intensity data were taken using a Hamamatsu streak camera with 532 nm light obtained by doubling some of the 1064 nm light in the switched out pulse. The double pass switchout configuration was used for the switchout system. Note that the data were taken in the green where the intensity range varies as the square of the intensity in the infrared, and therefore, to obtain the switchout intensity variation of the infrared, a square root must be taken. The results show similar operation with either dye, even though switchout timing varies throughout the short pulse train while staying in the first quarter to half of the long train. This suggests that the switchout triggering is operating as it should except for the time jitter. This jitter most likely exists due to the burst to burst fluctuations in energy in the pulse trains themselves, rather than the fluctuations in the switchout threshold.

CHAPTER 5

DIAGNOSTICS

Several techniques proved invaluable for verifying proper operation of the deflection system. The arrangement of Figure 24 enables measurement of the voltage pulse height and width within the deflection crystal, in addition to a determination of the electrooptic coefficient. An accurate prediction can then be made from these measurements concerning the eventual performance of the system in its deflection mode of operation.

Referring to the diagram, a single pulse is selected from the infrared pulse train which, after amplification, triggers the spark gap. The doubler and dichroic mirror provide the green light for the deflector. In this work the deflector consisted of a single crystal of deuterated KDP, KDDP, oriented to utilize the largest component of its electrooptic tensor, the r_{63} coefficient. With the field applied along the crystal z axis and the crystal x and y axes making a 45° angle with the crystal faces, the induced birefringence occurs along axes parallel and perpindicular to the crystal faces resulting in deflection for horizontally polarized light. This may be used to advantage to measure the induced birefringence. By illuminating the device with circularly polarized light, the polarization state of the transmitted light will vary as a function of the applied field, and a polarization analyzer at the output will then

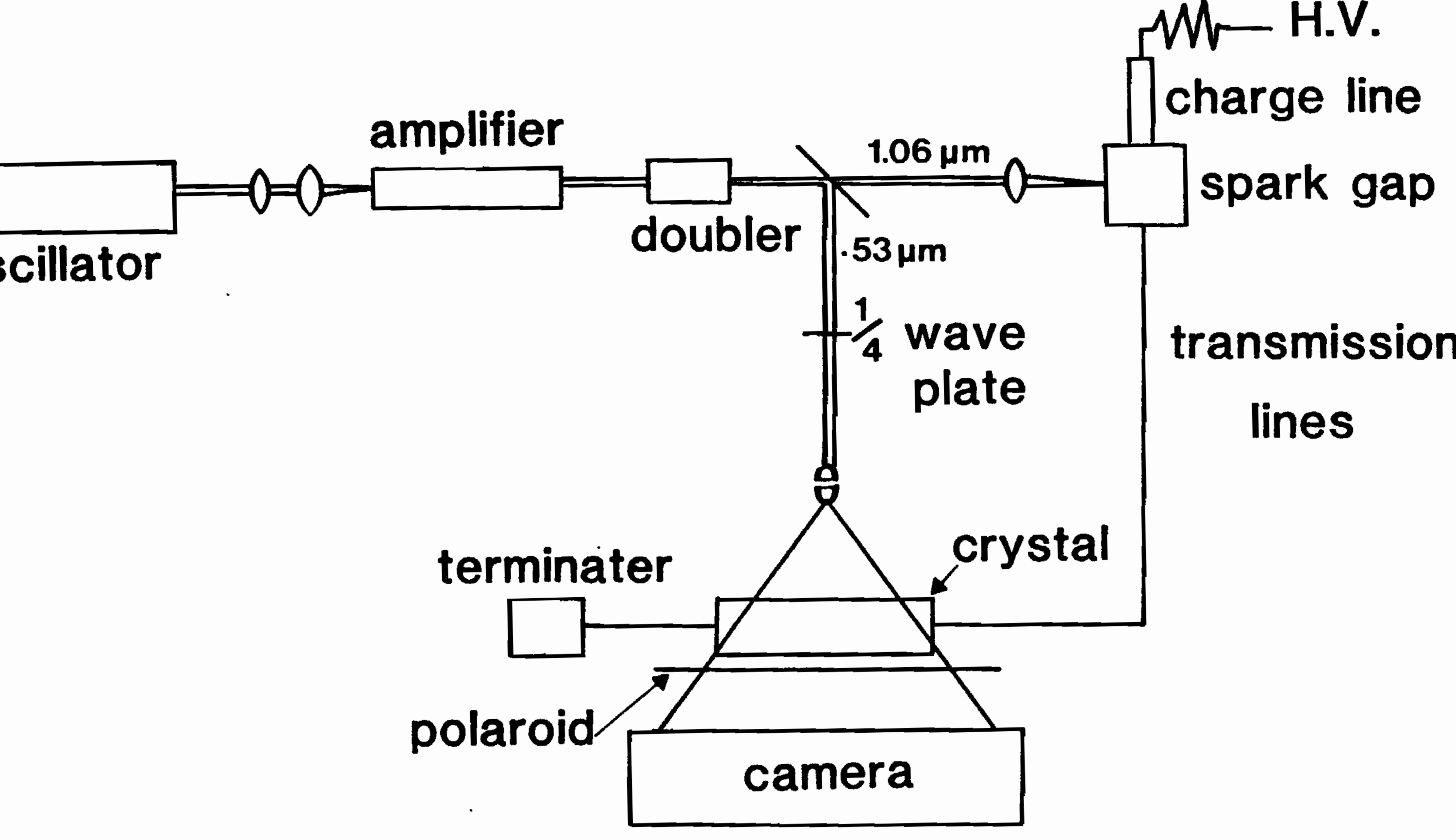

Figure 24. Test apparatus arrangement.
The system setup is illustrated for measuring voltage pulses in the crystal, and for obtaining data on the crystal itself.

convert the polarization variations to intensity changes. The resulting fringe pattern at the output then moves or deforms as a function of the applied field.

The arrangement shown consists of a quarter wave plate to create circular polarization, a diverging lens to illuminate the entire crystal, a polarization analyzer to form the fringe pattern, and film to record the pattern. A slight tilt of the crystal, causing non-normal incidence, provides closer fringe spacing for more accurate measurements. For this arrangement the fringe spacing varies quadratically, the spacing becoming smaller as one moves away from ray which passes through the crystal at normal incidence, this constituting the center of a symmetric pattern. Application of a static voltage to the stripline will cause fringe movement. Movement away from the pattern center when using KDDP implies that a voltage pulse of the same sign will induce a positive lens. Application of a voltage, V_o, sufficient to translate the pattern one fringe spacing allows easy determination of the electrooptic coefficient according to

$$r = 2\lambda d/n_o{}^3 V_o \ell \qquad (5.1)$$

for fringes involving light at near normal incidence (near the pattern center). Similar relationships hold for other orientations and other crystals, but may not be identical to these. Measurements on our crystal show $r_{63} = 2.2 \times 10^{-11}$ m/V, this being similar to value quoted, for example, by Yariv of 2.36×10^{-11} m/V.[72] By using this

same arrangement and varying the temperature of the crystal we obtained an accurate determination of $d(n_e - n_o)/dT$. Using a least squares fit to the equation

$$(n_e - n_o) = a + Td(n_e - n_o)/dT \tag{5.2}$$

gave $d(n_e - n_o)/dT = -7.7 \times 10^{-6}/°C$ with a standard deviation of $2 \times 10^{-7}/°C$. This is again in excellent agreement with the value of $(-7.3 \pm .15) \times 10^{-6}/°C$ found by Phillips.[73] Attempts to determine the Curie temperature showed $T_c = 160° K$ with a standard deviation of 16° K. Because of possible systematic problems with the apparatus when this measurement was made, the result may not be reliable, or perhaps the deuteration level of our crystal is lower than expected. Quoted values for heavy deuteration (90%) indicate $T_c = 220° K$,[74] with the Curie temperature varying smoothly down to 120° K as a function of decreasing deuteration.

This apparatus arrangement may also be used to measure the electrical pulse duration and height. Adjustment of the optical delay to obtain synchronism in the crystal with the voltage pulse allows a picosecond optical pulse to strobe the voltage waveform. Comparisons of the fringe pattern with and without the voltage pulse in the crystal enable computation of a field profile along the crystal width. The position information in conjunction with the speed of electrical propagation, then yields a time profile of the voltage pulse. For fast, high voltage pulses this may be the only

means of accurately measuring the pulse, since high voltage oscillo-
scope measurements are limited to risetimes longer than a nanosecond.

CHAPTER 6

EXPERIMENTAL RESULTS

The experimental aspects of this research have emphasized the development of the multiple lens system. Each of two experiments has demonstrated satisfactory agreement with theory and has pointed out the need for better high voltage, fast pulse sources. Although neither demonstration has achieved impressive results in terms of a large number of resolvable spots or fast time resolution, sufficient success has been obtained to warrant further development towards the goal of a useful infrared streak camera.

Figure 25 depicts the apparatus employed in the first experiment. Using a 60 cm cavity with Eastman 9740 dye in the mode locking cell, the Nd:YAG oscillator delivers a pulse train of 24 infrared pulses separated by 4 ns each. Subsequent lowering of the intensity by beam expansion then protects the amplifier rod, whose output drives the tandem KDP doubler crystals to convert some of the infrared to green. The dichroic mirror reflects the green while passing the infrared onto the spark gap for triggering of the conventional charged line pulse generator. This coaxial spark gap assembly, constructed from copper tubing, has an impedance of 12.5 ohms. It operates with a nitrogen pressure of 200 lbs. and a supply voltage of 20 kV to generate an 8 kV, 5 ns voltage pulse, which passes through a short section of mylar stripline into a bundle of 4, RG58U, 50 ohm coaxial cables (making 12.5 ohms) and finally into the

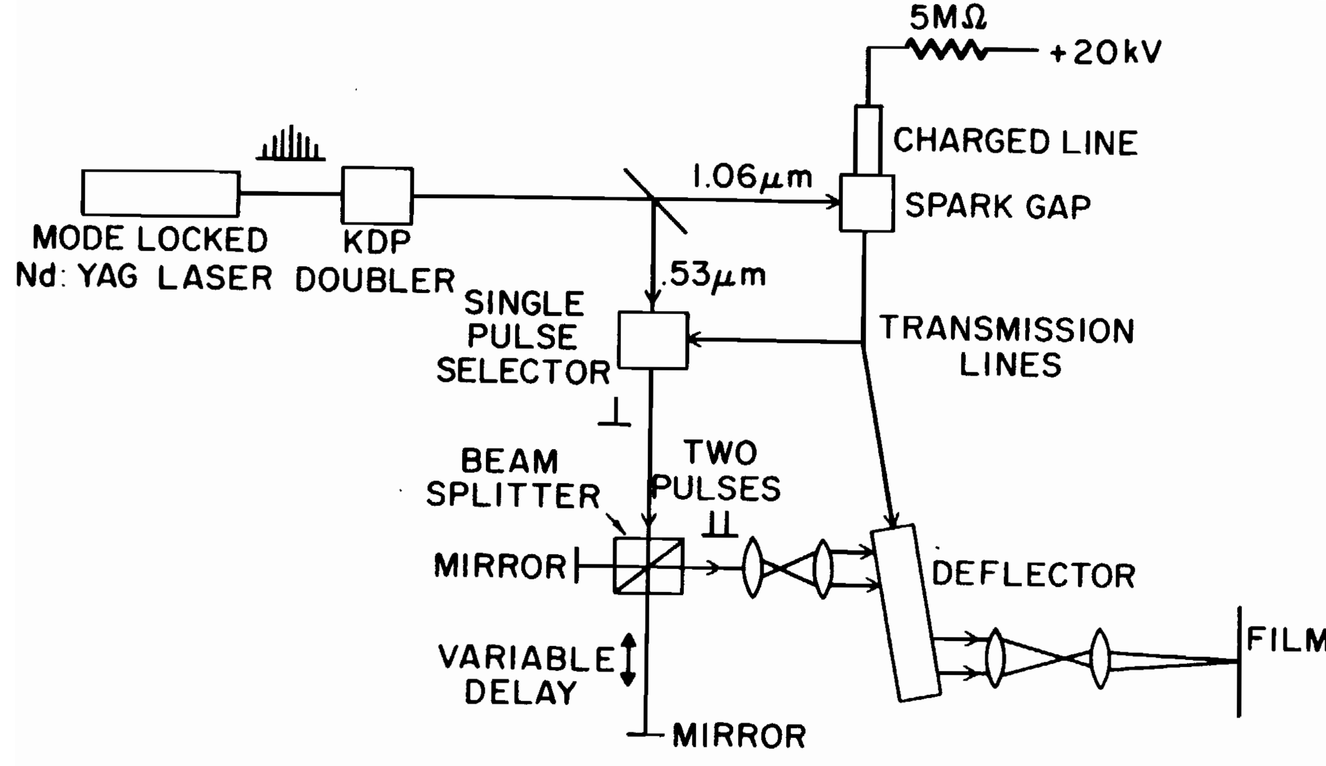

Figure 25. Experimental arrangement for deflection experiments.

deflector itself, from which another section of mylar stripline then guides the pulse to a 15 ohm resistive termination.

The green pulse train, after reflection from the dichroic mirror, passes through the Pockels cell single pulse selector. A one inch long, 1/2 inch diameter KDP crystal with ring electrodes at each end serves as the active switchout medium. The voltage pulse to activate the switchout is derived from the main spark gap generator by means of a wire connection to the mylar stripline at the output of the pulse generator. A switchout driven in this manner insures easy optical and electrical pulse synchronization with low jitter. Next, the horizontally polarized light from the switchout is delayed before entering a pulse stacker consisting of a beam splitter and two mirrors. Cylinder lenses expand the horizontal dimension of the base to fill the deflector aperture, and finally, after deflection, the beam is imaged onto film for recording of the induced beam movement.

An exploded view of the deflector appears in Figure 26. The beam width, 2w, is small compared to the value of Y, the electrical pulse halfwidth; however, for small deflections this is unimportant, as the primary determinant of operation in this range is the total interaction length of the light and field within the crystal. Moreover, a small beam width greatly relaxes the requirement concerning the optical quality of the crystal surfaces, which have large-scale errors in shape because KDDP is difficult to polish.

Figure 27 shows a densitometer tracing of one deflection event. The pulse stacker provides two pulses such that with no voltage

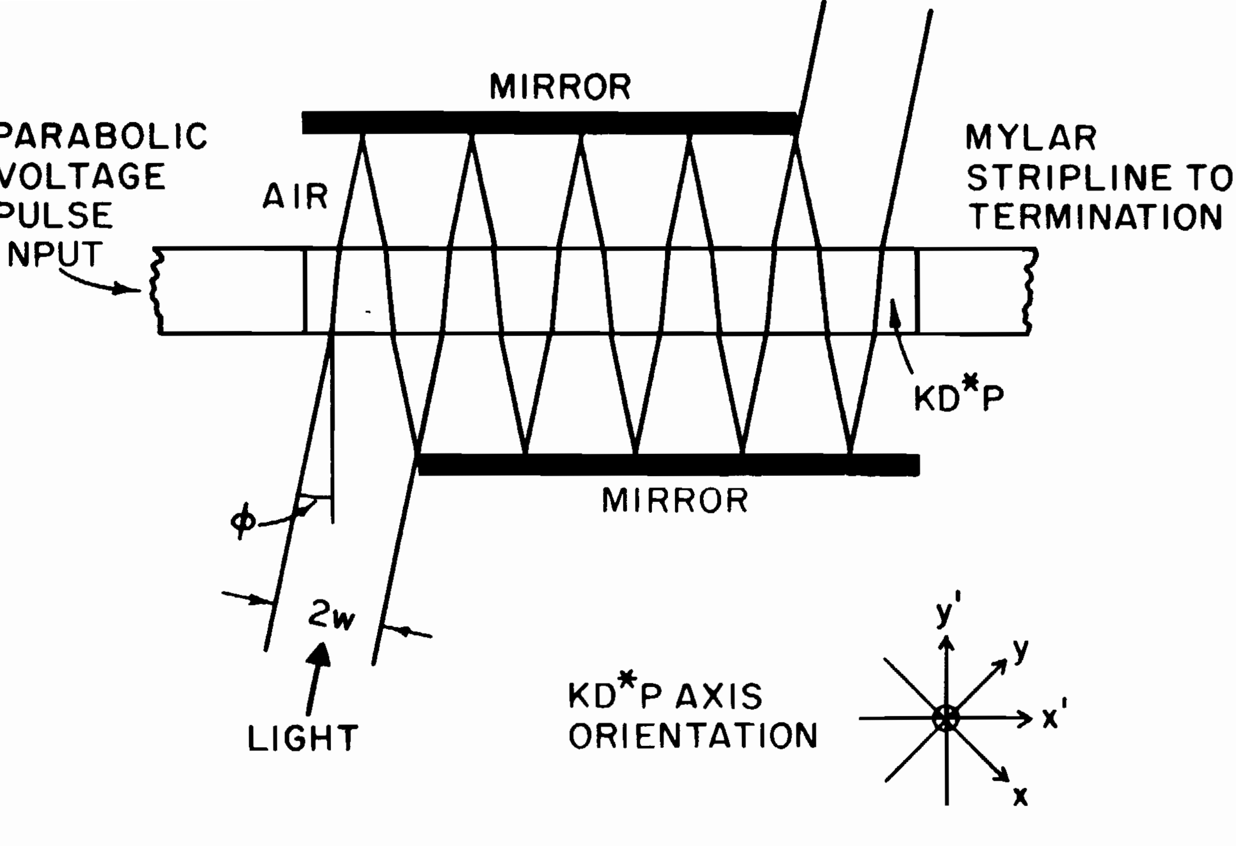

Figure 26. Deflector--exploded view.

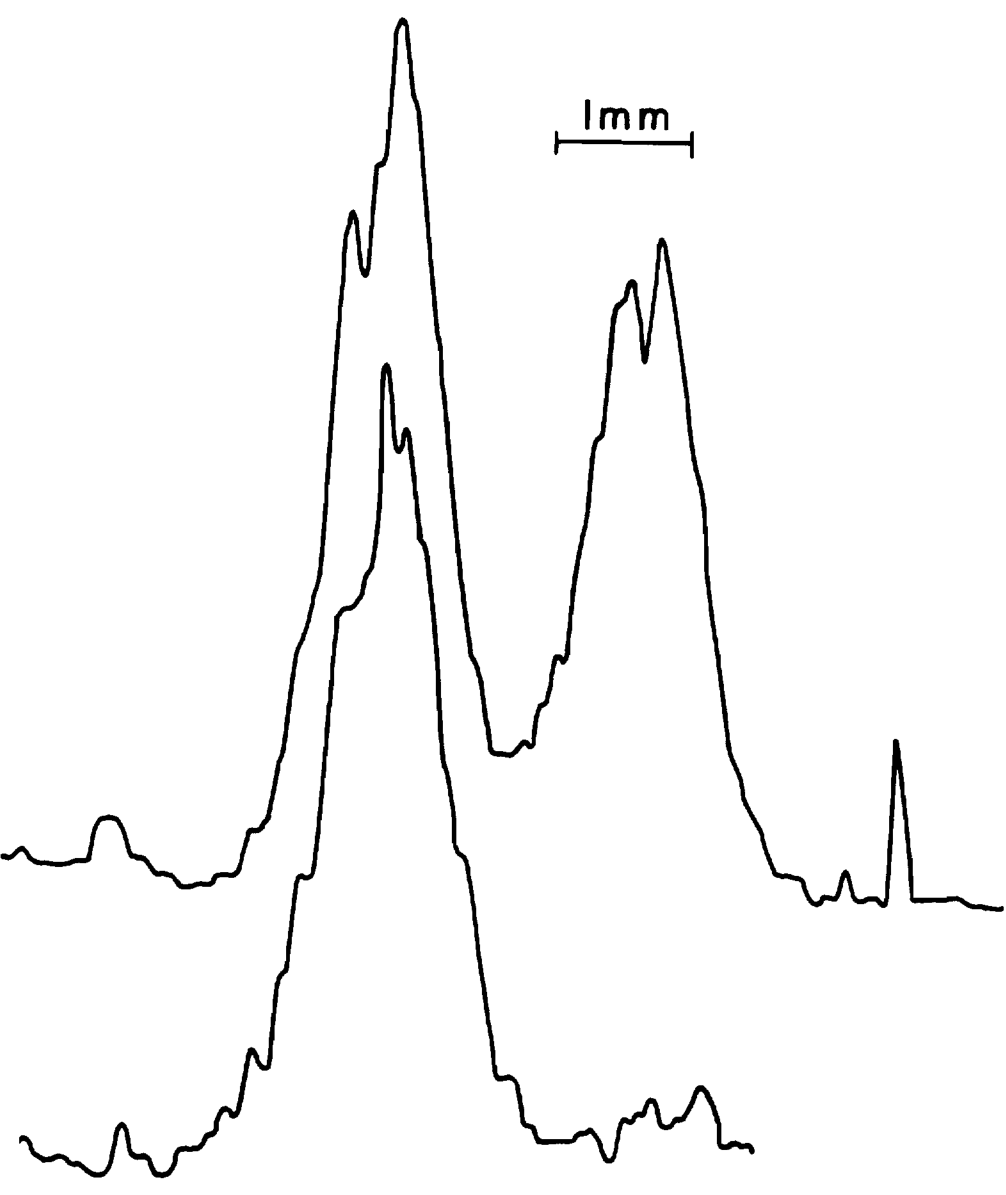

Figure 27. Sample experimental results for first deflection experiment.
The top trace shows two pulses, one deflected (right) and one undeflected (left) while the lower trace shows the pulses on top of each other.

applied they fall on top of each other (giving the lower trace), while application of a voltage pulse deflects only one of the pulses (giving the upper trace). The peak height and the full width at half maximum points fit a gaussian pulse of beam width 2w = 0.9 mm and indicate a one sided deflection of 1.15 mm, or 1.25 spots.

Analysis of many such pictures shows maximum deflection of 3.5 mm in one direction and 1.75 mm in the other direction for a total range of 5.25 mm. However, the spot size in these pictures is degraded somewhat from the diffraction limited value of 0.9 mm to a value of 1.5 mm. Thus, the deflection range corresponds to 5.8 spots, while the actual deflection in real spots is closer to 3.5 spots. The resolving time is then 5 ns/3.5 = 1.43 ns.

Equations (3.8) predict N = 6.8 spots when w = 6 mm, t_o = 5 ns, ε = 48, $Y_o = ct_o/2\sqrt{\varepsilon}$, q = 9, V = 8 kV, λ = 532 nm, n_o = 1.51, ℓ = 8 mm, d = 2 mm, θ_1 = 15 degrees, and $b = n_o^3 r \cos 2\theta_1/2$, where $r = 2.2 \times 10^{-11}$m/V (see Chapter 5) and the $\cos 2\theta_1$ arises from not having the light polarization along one of the induced birefringent axes. This difference, 5.8 versus 6.8 spots, is accounted for primarily by an experimental anomaly. The voltage pulse in the crystal, as measured using the technique described in Chapter 5, was only 6.3 kV rather than the 8 kV provided by the pulse generator. Further experiments with the apparatus showed that this was a problem arising from poor contact of the indium foil electrodes to the crystal. This was corrected at a later date by painting electrodes on with silver paint.

Use of the measured 6.3 kV value yields a prediction of 5.4 spots in excellent agreement with the experimental result of 5.8 spots.

A second experimental arrangement was chosen to improve the resolution time. Changing to a 50 ohm spark gap should decrease the pulse width by a factor of 50/12.5 = 4 according to the simple pulse generator model of Chapter 3, while dropping the voltage to 40% of 8 kV due to the required impedance change before entering the crystal. The new pulse amplitude would then be 3.5 kV with a width of 1.25 ns, and it would provide an increase in the number of spots by 1.6 times while decreasing the resolution time to less than one sixth of its previous value, i.e., 8 spots and 140 ps.

Attempts to generate the faster electrical pulse focused attention onto the various discontinuity and matching problems involved in getting the electrical pulse into the crystal. Referring to Figure 28, the spark gap is a coaxial 50 ohm system modeled after the Alcock design.[57] The pulse couples into a one inch long section of stripline (using the coupling technique of England[63]) to provide a near perfect match. The stripline impedance then changes to 10 ohms via an abrupt width change of the elctrodes on the woven, teflon-glass dielectric. The one inch section of 50 ohm stripline provides a good match from the coaxial geometry, while being short enough to insure that the voltage appearing on it will not exceed that in the 10 ohm section, thereby avoiding breakdown problems. The abrupt width change introduces a small capacitive discontinuity measured to

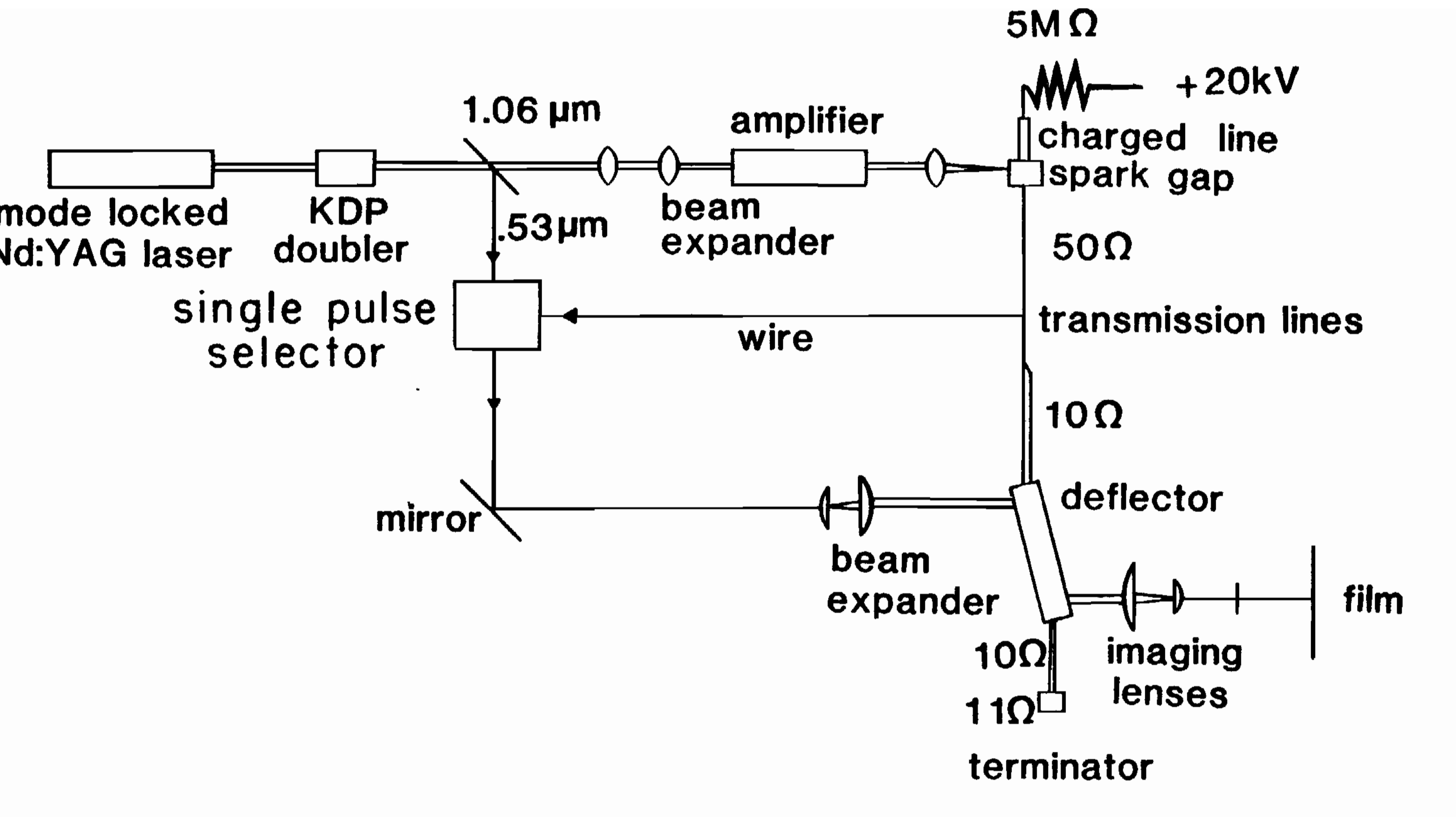

Figure 28. The setup for the second deflection experiment.

be no greater than 0.5 pf. Considered as a filter, the -3 db frequency of 0.5 pf at the junction of a 50 ohm and a 10 ohm line is 38 Ghz, which is acceptable. Another discontinuity occurs at the crystal where the dielectric thickness changes to maintain the same impedance with the same electrode width. The optical arrangement varies slightly from the previous experiment in that the green light is created and separated from the infrared before amplification in order to obtain better beam quality in the green. Changes in the deflector assembly were made in order to decrease the intensity of green light required for operation and to improve the optical quality, the latter being accomplished by index matching the crystal surfaces to optically flat glass plates.

The results with this new arrangement were somewhat discouraging. Oscilloscope measurements, subsequently confirmed by measurements made using the crystal (see Chapter 5), showed a voltage peak of 3.6 kV as expected, but the pulse width had shortened to only 2.5 ns, rather than the 1.25 ns expected. With the same material parameters as before, and with $w = 4.5$ mm, $V = 3.6$ kV, $q = 11$, $\theta = 20.7°$, $\theta_1 = 12.54°$ and $t_o = 2.5$ ns, Equations (3.38) predict $N = 6.4$ spots, $\tau = 350$ ps, and, with the imaging system now providing 1 mm of linear deflection per 0.0577 mrad of angular deflection, $w_o = 0.65$ mm and a total deflection range of 8.35 mm.

Figure 29 shows another densitometer tracing of two pulses, one deflected and one undeflected. By again fitting a gaussian to

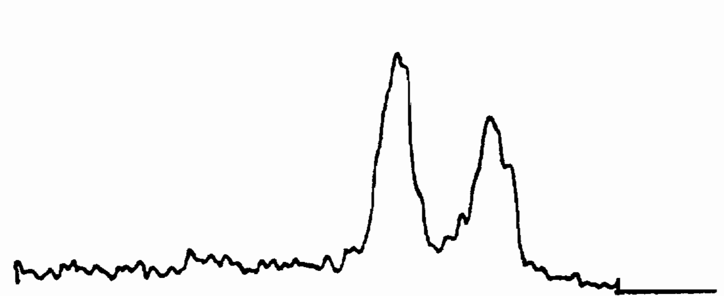

Figure 29. Sample experimental results for second deflection experiment. The densitometer tracing shows two pulses, one deflected and one undeflected.

the pulses, we measure a deflection of 1.7 spots, which when doubled gives a total range of 3.4 spots, only 53% of the predicted value, while the actual linear deflection amounted to 2.5 mm, corresponding to a full deflection range of 5 mm or 72% of the predicted value. The spot size thus appears to be somewhat larger than the diffraction limited value. From 1.7 spots in 1.25 ns a real resolution time of 740 ps is obtained (this being about twice as good as that of the first experiment). The discrepancy between the theory and experiment probably stems from our having not gathered sufficient data to accurately determine the peak deflection the device was capable of. As mentioned before, most of the attention in this experiment was focused on overcoming the difficulties involved in producing and working with faster pulses rather than obtaining accurate measurements of the deflector operation, since the wide pulse width inhibited realization of any significantly improved experimental results.

CHAPTER 7

FUTURE WORK

The next step to be taken should be the construction of a larger multiple lens deflection system utilizing lithium niobate. The smaller dielectric constant of lithium niobate provides higher stripline impedances enabling the transfer of a more nearly optimum voltage pulse into the deflector. The 8 kV, 2.5 ns, 50 ohm pulse generator described previously in conjunction with a 5 mm high, 5 mm thick, 20 cm long deflector crystal would provide 34 resolvable spot positions with a resolution of 69 ps each. This system would use total internal reflection rather than external mirrors, where an actual crystal width of 7 mm has been assumed. This represents a substantial improvement over the KDDP system and may perhaps be useful for work at 1.06 μm, but probably not for longer wavelengths.

From this example the need for a better voltage pulse generator is apparent. For example, the lithium niobate system with a 1 ns pulse width would provide 77 spots with 11 ps resolution at 532 nm, a very exciting result. This implies $N = 35$ spots and $\tau = 25$ ps at 1 μm, and $N = 10$ spots with $\tau = 75$ ps at 3 μm, which would still be useful.

Although construction of a large deflector with present day pulse generators may fulfill some current research needs, it is apparent that the primary development effort must be concentrated on electrical

pulse generators if significant gains are to be made. Solid state photoconducting systems appear the most promising, or perhaps carefully designed tapered impedance transmission lines may provide adequate improvement. Electron beam carrier excitation in semiconductors presents another option. Research in these areas is currently being done in several laboratories, but no clear solution has emerged.

APPENDIX 1

APPENDIX 1

QUADRUPOLE GEOMETRY

The quadrupole deflector is designed to provide a linear field gradient along the axes. Mathematically this implies

$$\frac{2E_z}{2y} = k \text{ and } \frac{2E_y}{2z} = k \tag{A1.1}$$

where the symmetry of the device demands satisfaction of both equations. The solution of these equations is

$$\overline{E} = kz\hat{j} + ky\hat{k} \text{ and } \phi = -kyz \tag{A1.2}$$

for the electric field vector and potential. Referring to Figure 6, the boundary conditions require $\phi = -V_o$ for $y = z = R/\sqrt{2}$. Thus $k = 2V_o/R^2$. Since the crystals of interest are usually nonisotropic, the dielectric tensor components must be used to determine the displacement vector. Assuming a component $\varepsilon_{\parallel}$ for a field in the z direction (usually the optic axis) and a component $\varepsilon_{\perp}$ for a field in the x-y plane, the quantities of interest may be written as

$$\phi = 2V_o yz/R^2$$

$$\overline{E} = 2V_o(z\hat{j} + y\hat{k})/R^2$$

$$\overline{D} = 2V_o(\varepsilon_{\perp} z\hat{j} + \varepsilon_{\parallel} y\hat{k})/R^2. \tag{A1.3}$$

To determine the capacitance of this device, the charge on the plates must be divided by the voltage. The charge may be computed

by integrating the charge density over the area of the negatively charged plates, where the surface charge density is given by $\sigma = \overline{D} \cdot \hat{n}$. Since $\overline{E}$ must be normal to the electrodes it can be used to construct a unit normal

$$\hat{n} = \overline{E}/|\overline{E}| = (z\hat{j} + y\hat{k})/\sqrt{y^2 + z^2} \,. \tag{A1.4}$$

The angle must be considered when integrating the charge density, and thus

$$C = Q/V = \frac{2}{2V_o} \int_o^{\ell} \int_a^b \frac{\sigma}{\cos\theta} \, dydx$$

$$\theta = \tan^{-1}(-dz/dy)$$

$$\sigma = \overline{D} \cdot \hat{n} \tag{A1.5}$$

where dz/dy is the slope of the line tangent to the electrode at x, the 2 before the integral accounts for there being two negatively charged electrodes having equivalent charge, and the $2V_o$ is the voltage between the positive and negative plates. The equation of the electrode in the first quadrant is given by (A1.3) and the condition $\phi = -V_o$. These yield

$$R^2 = 2xy$$

$$dy/dx = -R^2/2y^2$$

$$\cos\theta = 2y^2/\sqrt{R^4 + 4y^4} \,. \tag{A1.6}$$

The integration limits represent the intersection of the electrodes and the outermost electric field lines as depicted in Figure A1 and ignore the effects of fringing fields. The slope of the right side field line is given by

$$dz/dy = E_z/E_y = y/z. \tag{A1.7}$$

Integration of this equation along with the condition that the field line must pass through the point (0,R,0) leads to $z^2 = R^2 + y^2$ for the equation of the field line. The intersection of this curve with $R^2 = 2xy$ for the electrode yields

$$a^2 = (\sqrt{2} + 1)\, R^2/2 \quad \text{and} \quad b^2 = R^2/2(\sqrt{2} + 1). \tag{A1.8}$$

Finally, combining (A1.4) - (A1.8) the capacitance for the quadrupole arrangement is

$$C = (\varepsilon_\perp + \varepsilon_\parallel)\ell.$$

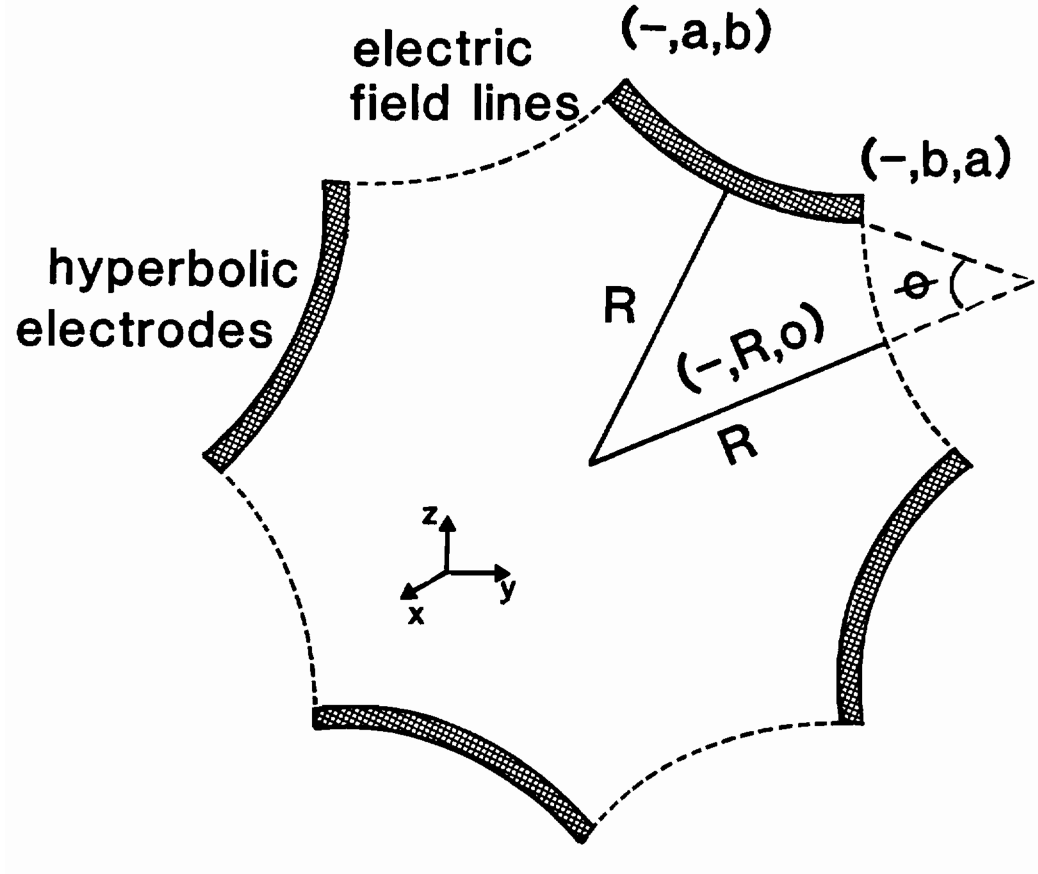

Figure A1-1. The hyperbolic electrode structure of the quadrupole deflector is shown along with the coordinates of points referenced in the analysis. The equation of the first quadrant electrode is $R^2 = 2xy$ and $b = R^2/2a$ at the electrode end points.

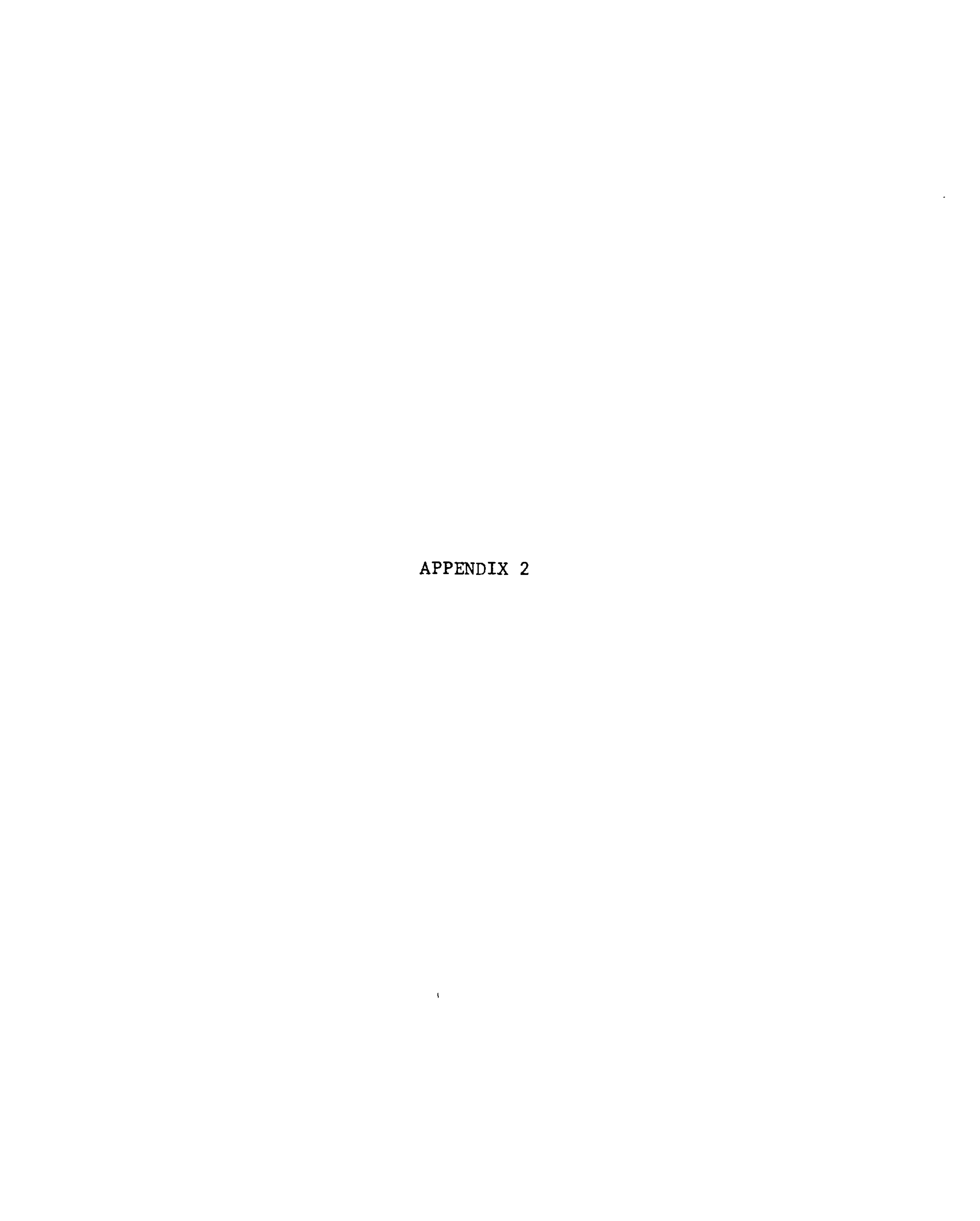

APPENDIX 2

APPENDIX 2

NEGATIVE LENS DEFLECTOR

This appendix will use simple geometric arguments coupled with the properties of gaussian beams to prove that positive lens deflectors are superior to negative lens deflectors.

Suppose a deflector is capable of deflecting the central ray of a gaussian beam through some maximum range as depicted in Figure A2-1. This deflection, or more fundamentally the path of the central ray of the beam, is independent of the beam width, but instead is determined only by the index gradients in the deflector. The slope of the exiting ray will be directly proportional to its height since the deflector may be represented by a linear ray matrix. Therefore a positive lens at the deflector output face will cause all exiting rays to pass through a single point as shown. The angle ϕ then represents the total deflection at the lens image plane, and the number of resolvable spots will be ϕ divided by the beam's full angular divergence β, given by $\beta = 2\lambda/\pi w$.

To determine the divergence the beam halfwidth w must be known. Figure A2-2 is similar to Figure A2-1, but now the rays corresponding to the beam edges (defined as the $1/e^2$ intensity points) are shown for both positive (dashed) and negative (dotted) lens deflectors. The beam widths are the same at the exit face and are as large as possible to decrease the beam divergence yet stay within the

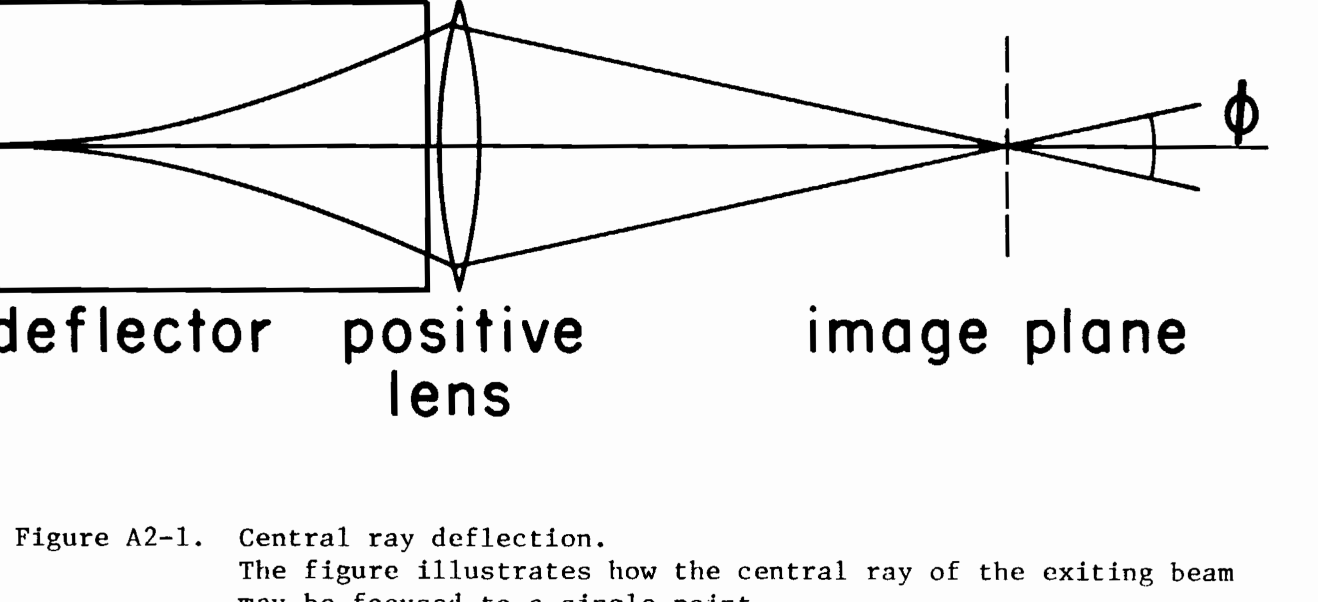

Figure A2-1. Central ray deflection.
The figure illustrates how the central ray of the exiting beam may be focused to a single point.

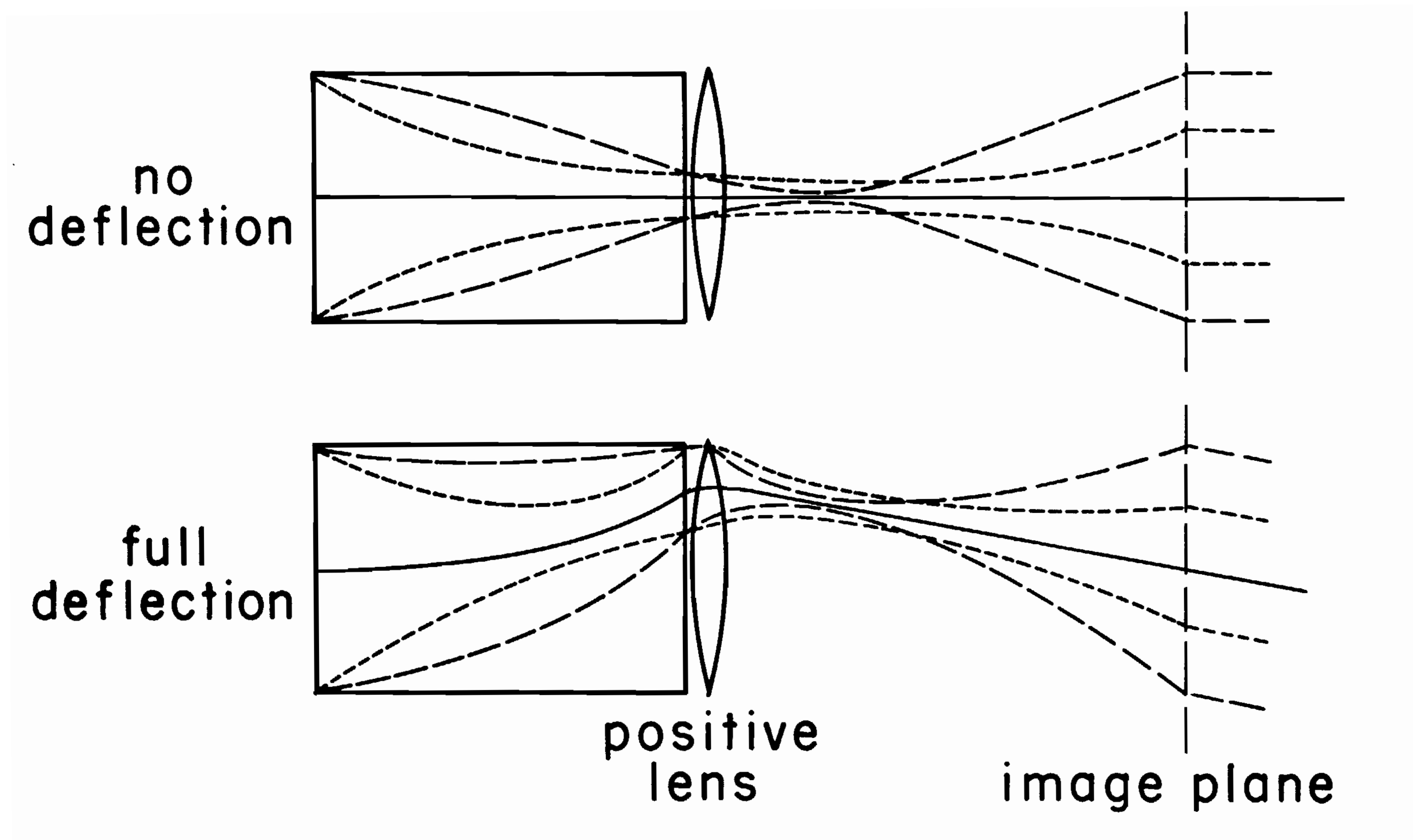

Figure A2-2. Positive and negative lens deflection characteristics.

deflector at full deflection. The lens at the exit affects the positive and negative beam edges differently since they do not have the same slopes, and consequently the beam size at the lens image plane is different for the two cases, and so are the slopes of the beam edges.

A second lens may now be placed at the first lens image plane in order to form a beam waist at that point. The lens must be different for the two deflectors under consideration, but that is of no importance. The central ray will still turn through a deflection angle of ϕ, and the full angular divergence for each case will depend only on the beam width at the second lens. Since the beam waist always occurs before the geometrical focus of a lens, the waists for the two deflector types will occur between the first lens and its image plane. Analysis of the beam edges at the exit of the deflector indicates that a more strongly focused beam will emerge from the lens (Figure A2-2) for the positive lens deflector. Thus, its waist will occur closer to the deflector as shown, its beam diameter will be larger at the image plane, its angular divergence β will be smaller at the image plane, and its total number of resolvable spots, $N = \phi/\beta$, will be larger than for the negative lens deflector.

From this argument it is clear that even though the deflection range and angle are the same at the deflector exit plane, as are the beam widths for these two cases, the number of resolvable spots are

different. In this situation the f-numbers of the emerging beams must be accounted for also. Here, this was accomplished by bringing the beams to a common geometrical image plane where the simple formula, $N = \phi/\beta$, applies for calculation of the number of resolvable spots.

REFERENCES

1. J. W. Shelton and J. A. Armstrong, IEEE J. Quantum Electron. QE-3, 696-697 (1967).
2. M. A. Duguay and J. W. Hansen, Opt. Commun. 1, 254-256 (1969).
3. R. R. Alfano and S. L. Shapiro, Opt. Commun. 6, 98-100 (1972).
4. E. G. Arthurs, D. J. Bradley and A. G. Roddie, Appl. Phys. Lett. 19, 480-482 (1971).
5. V. R. Nagibarov and V. V. Samartsev, Chem. Phys. Lett. 5, 61-63 (1970).
6. S. L. McCall and E. L. Hahn, Phys. Rev. 183, 457-485 (1969).
7. D. J. Bradley and G. H. C. New, Proc. IEEE 62, 313-345 (1974).
8. M. Maier, W. Kaiser and J. A. Giordmaine, Phys. Rev. Lett. 17, 1275-1277 (1966).
9. J. A. Armstrong, Appl. Phys. Lett. 10, 16-18 (1967).
10. H. P. Weber, J. Appl. Phys. 38, 2231-2234 (1967).
11. W. H. Glenn and M. J. Brienza, Appl. Phys. Lett. 10, 221-224 (1967).
12. H. P. Weber, J. Appl. Phys. 39, 6041-6044 (1968).
13. F. Zernicke and J. E. Midwinter, Applied Nonlinear Optics, (John Wiley & Sons, 1973), p. 61.
14. J. R. Klauder, M. A. Duguay, J. A. Giordmaine and S. L. Shapiro, Appl. Phys. Lett. 13, 174-176 (1968).
15. K. H. Drexhage, Appl. Phys. Lett. 14, 318-320 (1969).

16. H. E. Rowe and T. Li, IEEE J. Quantum Electron. QE-6, 49-67 (1970).

17. R. H. Picard and P. Schweitzer, Phys. Lett. 29A, 415-416 (1969).

18. H. P. Weber, Phys. Lett. 27A, 321-322 (1968).

19. F. A. Jenkins and H. E. White, Fundamentals of Optics (McGraw-Hill Book Co. Inc., 1957), p. 604-605.

20. M. A. Duguay and J. W. Hansen, Appl. Phys. Lett. 15, 192-194 (1969).

21. D. J. Bradey and W. Sibbett, Appl. Phys. Lett. 27, 382-384 (1975).

22. A. Yariv, Quantum Electronics (John Wiley & Sons, 1967), p. 327-335.

23. C. S. Hong, A. Yariv and B. Chen, Appl. Phys. Lett. 32, 668-670 (1978).

24. C. L. M. Ireland, Optics Commun. 30, 99-103 (1979).

25. T. C. Lee, J. D. Heaps and F. M. Schmit, Proc. IEEE 56, 1628-1629 (1968).

26. T. C. Lee and J. D. Zook, IEEE J. Quant. Elect. QE-4, 442-454 (1968).

27. C. S. Tsai and P. Saunier, Appl. Phys. Lett. 27, 248-250 (1975).

28. P. K. Tien, S. Riva-Sanseverino and A. A. Ballman, Appl. Phys. Lett. 25, 563-565 (1974).

29. G. A. Massey and R. A. Elliott, Appl. Phys. Lett. 29, 802-804 (1976).

30. R. A. Elliott and J. B. Shaw, Optics Letters 4, 49-51 (1979).

31. R. A. Elliott and J. B. Shaw, Applied Optics 18, 1025-1033 (1979).

32. J. D. Zook, Applied Optics 13, 875-887 (1974).

33. V. J. Fowler, C. F. Buhrer and L. R. Bloom, Proc. IEEE 52, 193-194 (1964).

34. M. Born and E. Wolf, Principles of Optics (Pergamon Press, 1975), p. 121-124.

35. A. Yariv, Quantum Electronics (John Wiley & Sons, 1967), p. 112.

36. A. Yariv, Quantum Electronics (John Wiley & Sons, 1967), p. 113.

37. F. S. Chen, J. E. Geusic, S. K. Kurtz, J. G. Skinner and S. H. Wemple, Proc. IEEE 52, 1258-1259 (1964).

38. J. D. Beasley, Applied Optics, 10, 1934-1936 (1971).

39. I. P. Kaminow and L. W. Stulz, IEEE J. Quant. Elect. QE-11, 633-635 (1975).

40. H. A. Wheeler, IEEE Trans. on Microwave Theory Tech. MTT-13, 174-185 (1965).

41. A. Yariv, Quantum Electronics (John Wiley & Sons, 1967), p. 99-104.

42. H. Kogelnik and T. Li, Applied Optics, 5, 1550-1567 (1966).

43. D. H. Auston, Appl. Phys. Lett. 26, 101-103 (1975).

44. A. M. Johnson and D. H. Auston, IEEE J. Quant. Elect. QE-11, 283-287 (1975).

45. S. M. Sze, Physics of Semiconductor Devices (Wiley-Interscience, 1969), p. 59.

46. P. LeFur and D. H. Auston, Appl. Phys. Lett. 28, 21-23 (1976).

47. A. Antonetti, M. M. Malley, G. Mourou and A. Orszay, Optics Commun. 23, 435-439 (1977).

48. L. J. Van Der Pauw, Phillips Res. Repts. 13, 1-9 (1958).

49. L. J. Van Der Pauw, Phillips Tech. Review 20, 220-224 (1958/9).

50. L. J. Van Der Pauw, Phillips Res. Repts. 16, 187-195 (1961).

51. R. Chwang, B. J. Smith and C. R. Crowell, Solid State Electronics 17, 1217-1227 (1974).

52. C. H. Lee, Appl. Phys. Lett. 30, 84-86 (1977).

53. O. S. F. Zucker, J. R. Long, V. L. Smith, D. J. Page and P. L. Hower, Appl. Phys. Lett. 29, 261-263 (1976).

54. W. K. Pendleton and A. H. Guenther, Rev. Sci. Instrum. 36, 1546-1550 (1965).

55. L. L. Steinmetz, Rev. Sci. Instrum. 39, 904-909 (1968).

56. M. Michon, H. Guillet, D. Le Goff and S. Raynaud, Rev. Sci. Instrum. 40, 263-265 (1969).

57. H. J. Alcock, M. C. Richardson and K. Leopold, Rev. Sci. Instrum. 41, 1028-1029 (1970).

58. R. J. Dewhurst, G. J. Pert and S. A. Ramsden, J. Phys. D: Appl. Phys. 5, 97-103 (1975).

59. F. Pinnekamp, G. Himmel and K. Bergstedt, Optics Commun. 11, 225-226 (1974).

60. S. Ramo, J. R. Whinnery and T. van Duzer, Fields and Waves in Communication Electronics (Wiley, 1944), p. 29-30.

61. F. B. A. Früngel, High Speed Pulse Technology. Vol. III., Capacitor Discharge Engineering (Academic Press, 1976).

62. H. Howe, Jr., Stripline Circuit Design (Artech House, 1974), p. 46.

63. E. H. England, IEEE Trans. on Microwave Theory Tech. MTT-24, 47-48 (1976).

64. C. Gupta and A. Gopinath, IEEE Trans. on Microwave Theory Tech. MTT-25, 819-822 (1977).

65. S. Ramo, J. R. Whinnery and T. van Duzer, Fields and Waves in Communication Electronics (Wiley, 1944), p. 477-481.

66. R. Horton, IEEE Trans. on Microwave Theory Tech. MTT-21, 562-564 (1973).

67. R. W. Klopfenstein, Proc. IRE, 44, 31-35 (1956).

68. D. Kajfez and J. O. Prewitt, IEEE Trans. on Microwave Theory Tech. MTT-21, 364 (1973).

69. R. E. Collin, Proc. IRE, 44, 539-548 (1956).

70. R. P. Hecken, IEEE Trans. on Microwave Theory Tech. MTT-20, 734-739 (1972).

71. A. M. Zarem, F. R. Marshall and S. M. Hauser, Rev. Sci. Instrum. 29, 1041-1044 (1958).

72. A. Yariv, Quantum Electronics (John Wiley & Sons, 1967), p. 333.

73. R. A. Phillips, J. Opt. Soc. Am. 56, 629-632 (1966).

74. I. P. Kaminow, Phys. Rev. 138, A1539-A1543 (1965).

BIOGRAPHICAL NOTE

John B. Shaw was born August 30, 1948, in Laramie, Wyoming. In 1951 he moved to Portland, Oregon where he attended primary schools and graduated from Woodrow Wilson High School in 1966. In 1970 he received his Bachelor of Arts degree from Portland State University in the field of Psychology.

From June 1970 until June 1977 the author was employed as a computer programmer. In 1974, while employed at Tektronix, Inc., he began part time study at the Oregon Graduate Center leading to the Master of Science degree in October 1976.

He continued at the Oregon Graduate Center on a part time basis until June 1977. He then began his doctoral research culminating in a Ph.D. in Applied Physics and Electronic Science in July 1980. During the 1979-1980 school year he finished his dissertation while holding a faculty appointment at the University of Portland, Department of Physics.

The author has been married for ten years to the former Deborah Wyss and they have two children, Rachel, age 5, and Jonathan, age 2.